

University of New Hampshire

## University of New Hampshire Scholars' Repository

---

Master's Theses and Capstones

Student Scholarship

---

Winter 2023

# AN EXPLORATION OF CONVENTIONAL BEAMFORMING APPLIED TO A PHASE MEASURING SONAR

JOAO CELSO SILVA DE DEUS

*University of New Hampshire*

Follow this and additional works at: <https://scholars.unh.edu/thesis>

---

### Recommended Citation

SILVA DE DEUS, JOAO CELSO, "AN EXPLORATION OF CONVENTIONAL BEAMFORMING APPLIED TO A PHASE MEASURING SONAR" (2023). *Master's Theses and Capstones*. 1782.

<https://scholars.unh.edu/thesis/1782>

This Thesis is brought to you for free and open access by the Student Scholarship at University of New Hampshire Scholars' Repository. It has been accepted for inclusion in Master's Theses and Capstones by an authorized administrator of University of New Hampshire Scholars' Repository. For more information, please contact [Scholarly.Communication@unh.edu](mailto:Scholarly.Communication@unh.edu).

**AN EXPLORATION OF CONVENTIONAL BEAMFORMING  
APPLIED TO A PHASE MEASURING SONAR**

BY

JOÃO CELSO SILVA DE DEUS

B. Sc. Naval Sciences, Escola Naval, Brazil, 2010

Extension Course in Hydrography (CAHO), Diretoria de Hidrografia e Navegação, Brazil, 2014

B.Sc. Production Engineering, Universidade Federal Fluminense, Brazil, 2020

THESIS

Submitted to the University of New Hampshire

in Partial Fulfillment of

the Requirements for the Degree of

Master of Science

in

Ocean Engineering

December, 2023

This thesis was examined and approved in partial fulfillment of the requirements for the degree of  
Master of Science in Ocean Engineering: Ocean Mapping by:

Thesis Director, John E. Hughes Clarke, Professor,  
University of New Hampshire.

Anthony Lyons, Research Professor,  
University of New Hampshire.

Thomas C. Weber, Affiliate Research Professor,  
University of New Hampshire.

Larry Mayer, CCOM Director/JHC Co-Director  
University of New Hampshire

On August 28th, 2023.

Approval signatures are on file with the University of New Hampshire Graduate School.

ALL RIGHTS RESERVED

© 2023

JOÃO CELSO SILVA DE DEUS



## ACKNOWLEDGEMENTS

First of all, nothing would have been possible if the Brazilian Navy had not trusted me and decided to invest in my qualification, so I cannot thank them enough. Also, there are no words to describe how grateful I am to the crews I have been part of throughout my career, made up of amazing people that inspired my fascination with the sea every day. I dedicate special thanks to CDR Anderson Peçanha for believing in my work and to LCDRs Leonardo Gomes, Vitor Pimentel, Guilherme Nascimento, Bruno Neves, and Dias Santos for helping me in my first steps as a surveyor.

To my UNH advisor, Professor John E. Hughes Clarke, I sincerely appreciate your dedication to teaching and guiding me through this research and sharing your invaluable experience, which broadened my view of Hydrography.

For the memorable moments in this trajectory, I thank the CCOM colleagues Adriano Fonseca, Airlie Pickett, Chiaki Okada, Dulap Ratnayake, Elaina O'Brien, Elias Adediran, Nicki Andreasen, and Sara Cardigos, who shared the Ocean Mapping adventure with me. I am also profoundly grateful to all UNH faculty, who were always concerned in preparing us in our best interest, especially Semme Dijkstra, who accompanied us most of the way here at CCOM.

Finally, I would not have made it without the full support of my family, Ana Carolina, Edmundo, and Riquelme. The sacrifices you made to be here with me, in another country, away from everyone but us, meant the world to me.

## TABLE OF CONTENTS

ACKNOWLEDGEMENTS .....	iv
TABLE OF CONTENTS.....	v
LIST OF TABLES .....	ix
LIST OF SYMBOLS, NOMENCLATURE OR ABBREVIATIONS .....	xvi
ABSTRACT.....	xviii
CHAPTER 1: INTRODUCTION.....	1
1.1. Statement of the problem .....	1
1.2. A brief review of Phase Measuring Bathymetry .....	2
1.3. Research questions .....	5
1.4. Research objectives .....	5
1.5. Thesis structure .....	6
CHAPTER 2: BACKGROUND.....	7
2.1. Definition .....	7
2.2. The phase ambiguity .....	9
2.3. Differential phase computation .....	10
2.4. Estimating DOAs from differential phases .....	11
2.5. Phase disambiguation.....	16
2.6. Deriving depths .....	17
2.7. Reducing the depth variance .....	18
2.7.1. Averaging equidistant pairs .....	19
2.7.2. The Vernier Method.....	23

2.7.3.	Time Average.....	25
2.8.	Known issues of phase measuring systems.....	33
2.8.1.	Lower sampling density.....	33
2.8.2.	Inherent nadir interference.....	35
2.8.3.	Baseline decorrelation.....	37
2.8.4.	Shifting Footprint.....	40
2.8.5.	Angular variance divergence.....	41
2.8.6.	Multipath.....	42
2.9.	The need for filtering.....	43
2.9.1.	Phase coherence.....	44
2.9.2.	SNR.....	45
2.9.3.	Window intensity.....	47
2.10.	Beamforming: an improvement?.....	51
2.10.1.	Beamforming (unsteered).....	52
2.10.2.	Steering a beam.....	54
2.10.3.	Adaptive beamforming.....	63
CHAPTER 3: METHODOLOGY.....		66
3.1.	The EdgeTech data format.....	66
3.2.	The data collection.....	70
3.2.1.	The systems used.....	70
3.2.2.	Installation.....	73
3.2.3.	Survey area.....	74
3.2.4.	The PMBS survey.....	76

3.2.5.	The MBES survey.....	85
3.3.	Why include beamforming in the bottom detection? And how? .....	86
3.3.1.	The steering control .....	88
3.3.2.	Converting beam steered differential phases to DOAs.....	90
3.4.	Beamforming and Time Average.....	93
3.4.1.	Defining the discrete steps .....	93
3.4.2.	The steering error .....	95
3.4.3.	Mitigating the steering error .....	96
3.5.	Beamsteering at nadir.....	101
3.6.	Beamforming algorithm implementation.....	105
3.6.1.	Stave spacing calibration .....	106
3.6.2.	Averaging phases .....	110
3.6.3.	Estimating the angular uncertainty .....	112
3.6.4.	Improving efficiency.....	115
3.6.5.	Filtering.....	116
3.6.6.	Algorithm overview .....	117
3.7.	Data visualization and analysis .....	119
3.7.1.	Integration.....	119
3.7.2.	Vertical datum correction .....	122
3.7.3.	Gridding .....	122
3.7.4.	Visualization tools .....	123
3.7.5.	The depth cross-check.....	124
CHAPTER 4: RESULTS.....		126

4.1. Beamforming performance .....	126
4.1.1. Split-arrays used.....	126
4.1.2. Beamforming vs. conventional depths.....	129
4.1.3. SNR and phase coherence.....	136
4.1.4. Comparison to the reference dataset .....	138
4.1.5. Processing time .....	140
4.2. EdgeTech solutions vs. EM2040P .....	141
4.2.1. Mean depth cross-check.....	141
4.2.2. Target detection .....	144
4.2.3. Density .....	148
4.2.4. Efficiency .....	155
CHAPTER 5: CONCLUSION .....	158
5.1. Discussion .....	158
5.2. Suggestions for future works.....	162
LIST OF REFERENCES .....	164

## LIST OF TABLES

Table 1 - Phase cycle number, depending on the stave spacing. ....	15
Table 2 - Half-Power Beamwidths for a 9-element Chebyshev-shaded array.....	58
Table 3 - JSF Message Types and Core Information.....	67
Table 4 - Sonar Trace Record Organization .....	68
Table 5 - Echo sounder specs.....	72
Table 6 - Inertial System specs.....	73
Table 7 - Sensor lever arms. ....	74
Table 8 - Sensor rotations .....	74
Table 9 - Water line height .....	74
Table 10 - Settings used during data collection.....	76
Table 11 - Normal incidence steering statistics against the EM2040P reference dataset.....	102
Table 12 - Filter thresholds used for the beamforming algorithm.....	116
Table 13 - Density - EM2040P vs. 6205.....	150
Table 14 - Efficiency comparison: EM2040P vs. 6205.....	156

## LIST OF FIGURES

Figure 1 - Geometry of Lloyd mirror system.....	2
Figure 2 – Differential phase geometry from a tilted stave pair. ....	7
Figure 3 - Phase difference geometry assuming far field. ....	8
Figure 4 - Example of theoretical phase shift and phase difference curves for an EdgeTech 6025 3-lambda spaced stave pair, with a mounting angle of 35° sitting 30 m above a flat surface. ....	10
Figure 5 - Phase shifts and Phase differences for an EdgeTech 6205 distinct stave spacings, with a mounting angle of 35° sitting 30 m above a flat surface. ....	12
Figure 6 - Phase shift and phase difference curves in the angular domain. ....	13
Figure 7 – Depths calculated from an unambiguous stave pair. ....	19
Figure 8 - A PMBS Uniform Linear Array.....	20
Figure 9 – Depths calculated from the average of all unambiguous pairs’ phase differences.....	22
Figure 10 - Circular mean angle. ....	23
Figure 11 - The Vernier logic used in the algorithm. ....	24
Figure 12 - Depths calculated using the Vernier method. ....	25
Figure 13 - Depths calculated with different sample windows.....	26
Figure 14 - Time average within an angular subset.....	27
Figure 15 - Flat seafloor assumption impact on windows. ....	29
Figure 16 - Sloped angular window limit derivation. ....	30
Figure 17 – The effect of window size compensation in bathymetry.....	31
Figure 18 - Using regression within an angular window to evaluate a sample. ....	32
Figure 19 - Average Phase vs. Regression results. ....	32

Figure 20 - Differential horizontal distance between adjacent samples. ....	33
Figure 21 - Differential horizontal spacing and DOA vs. Horizontal Range. ....	34
Figure 22 - Common Slant Range. ....	36
Figure 23 - Projected pulse lengths over different horizontal ranges. ....	38
Figure 24 - Baseline decorrelation - CW vs. FM.....	39
Figure 25 - Shifting footprint.....	40
Figure 26 - 6205 shifting footprint vs. baseline decorrelation.....	41
Figure 27 – Incidence angle vs. Angular standard deviation sensitivity for a half-lambda pair and 35° mounting angle w.r.t. vertical.....	42
Figure 28 - Outbound Multipath and Inbound Multipath. ....	43
Figure 29 – Phase coherence parameter computation.....	44
Figure 30 - Coherence vs. Horizontal Range.....	45
Figure 31 - Decomposing the complex products into their signal and noise component. ....	46
Figure 32 - SNR vs. Horizontal Range. ....	47
Figure 33 - Window intensity vs Horizontal Range .....	48
Figure 34 - Side scan image from a 6205 line, P.L. 3.7 ms.....	49
Figure 35 - Backscatter image from a 6205 line, P.L. 3.7 ms. ....	49
Figure 36 – Backscatter image from a 6205 line, P.L. 3.7 ms., window average compensated for elevation and slope change across-track. ....	50
Figure 37 - Theoretical beamforming multipath suppression.....	51
Figure 38 – Estimated beam pattern of one EdgeTech 6205 stave and ten staves. ....	54
Figure 39 – Unshaded response vs. Dolph Chebyshev response for nine elements, 0° steering, and SLL=-30dB. ....	57



Figure 40 - Hypothetical transmit beam pattern, achieved with a 3-element beamforming, shaded by the kernel [0.1007, 1, 0.1007].	59
Figure 41 - Steering down 55° an EdgeTech 6205 9-stave split-array.	60
Figure 42 – Estimated Main Lobe Half-Power Beamwidth per Steering Angle for the EdgeTech 6205.	60
Figure 43 - 9-stave split array.	62
Figure 44 - 7-stave split array.	62
Figure 45 - Discover Recording Settings.	66
Figure 46 - EdgeTech Subsystem Channels	69
Figure 47 - Theoretical TVG vs. EdgeTech TVG.	69
Figure 48 - General scheme for the swath systems used.	71
Figure 49 - EM2040P main components.	71
Figure 50 - EdgeTech 6205 main components.	71
Figure 51 - Applanix POSMV 320 V5 main components: Processing unit, dual antennas, and Inertial Measurement Unit (IMU).	72
Figure 52 - R/V Gulf Surveyor.	73
Figure 53 - Survey Location	75
Figure 54 - Survey Line Plan. NOAA chart 13283 - depths in feet.	75
Figure 55 - EdgeTech 6205 dataset - Max range 50m, PL 0.25ms.	77
Figure 56 - Discover advanced bathymetric controls.	78
Figure 57 - Discover advanced sonar controls.	79
Figure 58 - Ping rate for 100m maximum range, about 8m depth, and pulse lengths of 0.25 ms and 3.7 ms	80

Figure 59 - Ping rate for 50m maximum range, about 8m depth, and pulse lengths of 0.25 ms and 3.7 ms.....	81
Figure 60 - Discover bathymetric processing engineering parameters.....	82
Figure 61 - TVG off vs. Default TVG - 50 dB/100m.....	83
Figure 62 - Expected beam patterns for the different multipath suppression levels.....	84
Figure 63 - EM2040P dataset. ....	85
Figure 64 - Theoretical beam patterns (unsteered) that can be used in the algorithm. ....	87
Figure 65 - Intensity time series (log scale).....	88
Figure 66 - An initial concept for the beam steering. ....	89
Figure 67 - Steering angle for a 0° estimated DOA.....	90
Figure 68 - Fictitious 3-stave array. ....	90
Figure 69 - Virtual mounting angle $\Psi'$ . ....	92
Figure 70 - Samples to be beam steered at each step.....	94
Figure 71 – Bottom detection with a step size lower than the HPBW vs. a step higher than the HPBW. ....	94
Figure 72 - A profile comparing the Algorithm and EdgeTech Solutions. ....	95
Figure 73 - Beamformed Amplitude and Phase Time Series. ....	96
Figure 74 - The impact of changing elevation on the beam steering vector. ....	97
Figure 75 - Correcting the elevation in steps of 20°, 10°, and 0.5°. ....	98
Figure 76 - Choosing beamforming channels using the Amplitude Time Series. ....	99
Figure 77 - Bottom detection using amplitude-chosen beamforming channels. ....	100
Figure 78 - Result from a Root-Music algorithm devised by Wang (2018) vs. Algorithms devised in this study. ....	101

Figure 79 - Center pivot beam steering and Common pivot beam steering .....	105
Figure 80 - Calibration of the sound speed of the design using Vernier solutions.....	107
Figure 81 - Unshaded beam steered intensities (No TVG).....	108
Figure 82 - Beam steered intensities (No TVG), Chebyshev shading SLL -30dB applied.....	109
Figure 83 - Bathymetric grid of normalized complex products.....	111
Figure 84 - Bathymetric grid of amplitude-weighted complex products.....	111
Figure 85 – Angular standard deviation vs. Incidence angle.....	114
Figure 86 - Depth standard deviation vs. Incidence angle.....	115
Figure 87 - Unfiltered vs. Filtered bathymetry grid.....	117
Figure 88 - Ship position considered for integration. ....	119
Figure 89 – Draft used for Ray tracing. ....	120
Figure 90 - EdgeTech 6205 beam vector.....	120
Figure 91 - The Ray Tracing process.....	121
Figure 92 - Geo-referencing depths.....	121
Figure 93 - Tide station and survey locations.....	122
Figure 94 - Unfiltered grid from this study’s beamforming bottom detection algorithm.....	123
Figure 95 - Qimera's cross-check tool plot.....	125
Figure 96 - 3, 5, 7, and 9-stave beamforming solutions. ....	127
Figure 97 – 3 and 9-stave beamforming quality metrics.....	128
Figure 98 - 2D depth solutions from different phase bottom detection algorithms.....	129
Figure 99 – 1-meter-high boulder at the nadir.....	130
Figure 100 - Comparison between Half-wavelength, Vernier, and Beamforming DTMs.....	133
Figure 101 - Visual recognition of morphology.....	134

Figure 102 - Nadir solutions for different phase bottom detection algorithms.....	136
Figure 103 - SNR and coherence - Vernier vs. Beamforming.....	137
Figure 104 - Algorithms' grid difference statistics. ....	139
Figure 105 - 6205 raw lines cross-checked with the EM2040P reference dataset. ....	142
Figure 106 - 6205 raw line uncertainty (95% confidence) vs. beam angle. ....	143
Figure 107 – Case 1 - Target detection at close range.....	144
Figure 108 - Case 2 - Target detection at mid-range. ....	145
Figure 109 - Case 3 - Target detection at far range. ....	146
Figure 110 - Feature boundaries in the EM2040P-6205 grid difference.....	147
Figure 111 - 6205 density layer (soundings/node) at 10-meter altitude. ....	148
Figure 112 – EM2040P density layer (soundings/node) at 10-meter altitude. ....	148
Figure 113 - Sounding Density - 6205 vs. EM2040P.....	149
Figure 114 - 6205 across-track density profile. ....	151
Figure 115 – Smearing and noise at normal incidence.....	152
Figure 116 - Maximum heading change rate observed at this study's survey. ....	153
Figure 117 - Ping distribution along a heading change. ....	154

## LIST OF SYMBOLS, NOMENCLATURE OR ABBREVIATIONS

AOA	Amplitude of Arrival
ASCII	American Standard Code for Information Interchange
AUV	Autonomous Underwater Vehicle
CAATI	Computed Angle-of-Arrival Transient Imaging
CW	Continuous Wave
DHN	Diretoria de Hidrografia e Navegação
DOA	Direction of Arrival
DTM	Digital Terrain Model
FM	Frequency Modulated
GNSS	Global Navigation Satellite System
GAMS	GNSS Azimuth Measurement Subsystem
GIS	Geographic Information System
HPBW	Half-Power Beamwidth
IHO	International Hydrographic Organization
IMU	Inertial Measurement Unit
LAT	Latitude
LONG	Longitude
MBES	Multi Beam Echo Sounder
MLLW	Mean Lower Low Water
MUSIC	Multiple Signal Classification
NaN	Not a Number

NOAA	National Oceanic and Atmospheric Administration
NPL	National Physical Laboratory
PL	Pulse Length
PMBS	Phase Measuring Bathymetric Sonar
PPS	Pulse per Second
PU	Processing Unit
RMSE	Root Mean Square Estimator
ROT	Rate of Turn
RP	Reference Point
RTK	Real Time Kinematic
RVGS	Research Vessel Gulf Surveyor
Rx	Reception
SIS	Seafloor Information System
SLL	Sidelobe Level
SNR	Signal-to-Noise Ratio
TVG	Time Varying Gain
TWTT	Two Way Travel Time
Tx	Transmission
ULA	Uniform Linear Array
UNH	University of New Hampshire
UTM	Universal Transverse Mercator
w.r.t.	With Respect To

## ABSTRACT

Brazilian rivers are a particularly challenging navigation environment because of frequent changes in bathymetry due to sediment transport. To accelerate the production of hydrographic information for these regions, the Brazilian Hydrographic Office has been investigating efficient ways of riverine surveying. In this context, Phase Measuring Bathymetric Sonars (PMBS) are being considered because of their potential to provide wider swaths than traditional Multibeam Echo Sounders (MBES) in shallow waters. Although these systems historically had severe limitations in sounding quality and nadir density, new models with multiple stave pairs are being built to overcome these issues, including the EdgeTech 6205, which claims to use beamforming to resolve nadir gaps, a long-term problem of PMBS.

This research reproduced conventional phase detection algorithms and compared them to an in-house developed differential phase Direction of Arrival (DOA) estimator, which uses phase-shift beamforming to constrain the receiver elevation angle sensitivity. To assess the 6205's performance, a shallow water region, known to have varying seafloor characteristics, such as rough, smooth, target-filled, and a seafloor depth gradient, was investigated by both an EdgeTech 6205 and, as a benchmark reference, an MBES Kongsberg EM2040P, already well-assessed and used in high-quality hydrographic surveys around the world. Depths were comparable to shallow rivers to assess if it would provide reasonable quality and efficiency for riverine surveys.

The results obtained indicated that the use of beamforming significantly contributed to the suppression of multipath and noise. At the same time, the system evaluation attested to its potential to be used in hydrographic surveys, being an efficient alternative to conventional multibeam systems for IHO S-44 Order 1 riverine surveys.

## CHAPTER 1: INTRODUCTION

### 1.1. Statement of the problem

The Brazilian Hydrographic Office (Diretoria de Hidrografia e Navegação - DHN) constantly assesses ways of making the nautical chart production flow more efficient. Lately, one critical concern has been the time delay between the data collection and the information being released to the public on riverine zones. This concern stems from the fact that rivers have a significant role in the Brazilian transportation of cargo and people. According to the Brazilian National Department of Transport Infrastructure (DNIT, n.d.), the prioritized riverine transport network has an approximate length of 19.000 km, from which about 70% is critical to shipping and people transportation. Additionally, some cities in the middle of the Amazon Forest depend exclusively on riverine transport. Therefore, this reinforces the need for regular and trustable nautical infrastructure in those locations.

Additionally, Brazilian rivers are an essential and challenging environment for charting. Some of the most relevant rivers for navigation, such as the Amazon River, have a dynamic seabed environment due to significant currents and a high rate of sediment transport. Due to that, sand banks are constantly changing position along the rivers, needing frequent updates in nautical charts, and the time delay mentioned contributes to higher navigation risks.

One solution considered is periodically releasing updated information for safe corridors instead of publishing entirely new nautical charts thereby accelerating the information release to mariners. In this approach, a swath echo sounder would be used to record depths during a round trip up and down the river, establishing a recommended area for navigation. To obtain the



maximum coverage within that transit, Phase Measuring Bathymetric Sonars (PMBS) have been considered due to their expected good coverage in shallow waters.

## 1.2. A brief review of Phase Measuring Bathymetry

The possibility of using interferometry to measure a swath of depths was theorized by Tucker (1960). In the same decade, relevant field tests were performed by Chesterman et al. (1967), when records of a towed side scan sonar showed an interference pattern caused by the surface multipath in calm sea, analogous to the optics Lloyd Mirror effect, from which the author could estimate the sea floor slope.

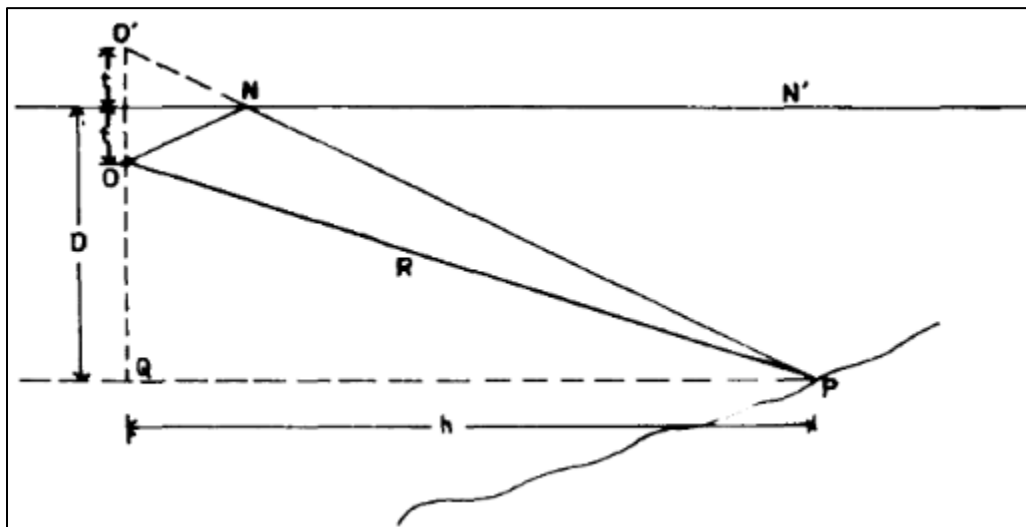


*Figure 1 - Geometry of Lloyd mirror system. Retrieved from Chesterman et al. (1967).*

Later, Stubbs et al. (1974) reproduced Chesterman's study using two experimental assemblies. The first used a reflector mounted over a side scan transducer, to obtain Lloyd mirror fringes independently of the sea state. The second used the interference of two parallel arrays, where one of them would take the position of the virtual array ( $O'$ ) in Figure 1. The author

described obtaining across-track depth profiles under realistic sea conditions, naming the approach “telesounding” that is equivalent to what is known today as swath bathymetry.

With developments in electronics, Denbigh (1977), as cited in Cloet et al. (1982), measured the phase continuously instead of adding the transducer outputs, making it possible to produce continuous depth profiles, as obtained in modern systems today. Butowski (2002) mentions that Denbigh first proposed a system with two parallel linear elements in 1977, spaced three wavelengths apart and operating at 410 kHz, which showed ambiguous measurements at angles greater than  $9.6^\circ$  from broadside. That made him build another prototype, with a spacing of 1.1 wavelengths, mitigating the ambiguity to  $27^\circ$ . In the 80's, developers produced different geometries of bathymetric sonars to optimize results, culminating with the introduction of several commercial systems, such as the Bathyscan 300 described by Cloet & Edwards (1986).

Since then, although the detailed engineering geometry is usually not public, some generalizations regarding side scan sonars design can be made: two-row systems have existed utilizing spacing of half wavelength, e.g., SeaMARC II, from International Submarine Technology Ltd. (de Moustier, 1988), but most have been designed with three or four rows, deliberately unevenly spaced (e.g., Kongsberg Geoswath and S.E.A. SwathPlus). Other companies, such as Teledyne Benthos Inc., have chosen to build 6-element uniform linear arrays (ULAs), arrays with identical elements uniformly spaced in a line, to make use of the CAATI (Computed Angle-of-Arrival Transient Imaging) method of echo arrival estimation, developed in 1998 at the Simon Fraser University (Kraeutner, 1998).

Even with a four-decade history of implementation, the quality of phase measuring sonars' sounding data has been questioned by some Hydrographic Offices, such as NOAA (2022) and DHN. NOAA (2022) states that “the discrete soundings generated by these systems may have

unacceptably high uncertainty for use in nautical charting and that some systems may be incapable of reliably resolving features to the standards required in this manual”. In turn, although the last version of DHN standards for hydrographic surveys (NORMAM-25 2°Rev) does not restrict any specific technology, Pimentel (2018), from DHN, describes an extensive list of scientific articles which performed comparisons between commercial PMBS and MBES, stating that evaluations of PMBSs imply that there are still many issues in its use for bathymetric surveys. The issues mentioned were gaps in the system nadir, noisy solutions, depth ambiguity, unmanageably large datasets, and high vertical uncertainty.

Considering these issues, EdgeTech has uniquely produced a solution in the last decade with 8 (model 4600) and now ten rows (models 2205/6205). These systems differ because they have more rows and have chosen to retain regular element spacing. As such, they have the potential to benefit from beamforming, a method that was not previously employed.

According to the manufacturer’s literature, the most remarkable result of implementing the beamforming is to have usable bathymetric solutions at the nadir, one of the most limiting factors observed in PMBS. The company called this new approach “multi-phase technology”, claiming to overcome the historical problems, and stating that the system can maintain constant data density and resolution throughout the entire swath width while complying with IHO S-44 Special Order, requiring minimal post-processing and co-registering high-resolution side-scan sonar image.

The company published online tests performed by Brisson, Wolfe, & Staley (2014), evaluating the 6205 in comparison to a multibeam reference dataset. Even so, the published results were limited to an almost flat seafloor at 10-meter depth, meaning that more tests could be performed to understand the system’s capabilities better. This thesis then focuses on investigating

how combining beamforming and phase differencing bottom detection may produce an improved solution by analyzing EdgeTech 6205 data.

### **1.3. Research questions**

With a focus on the problem previously described, the following questions summarize the intended study:

- a) Can applying beamforming in a multi-stave PMBS improve the signal processing results?
- b) How does the implied manufacturer's solution perform compared with a well-assessed conventional multibeam echo sounder?

### **1.4. Research objectives**

Three objectives were defined to answer these research questions:

- a) Develop a bottom detection algorithm that includes beamforming to transform the PMBS observables (10-element time series of complex sound pressure amplitudes) into pairs of slant-range and Direction of Arrival (DOA).
- b) Use the algorithm to assess the impact of beamforming in phase differencing depth solutions by comparing it to conventional Vernier method results.
- c) Compare datasets acquired with the PMBS multi-stave system (both the manufacturer's proprietary solution and this thesis' in-house developed) under different sonar settings and over different characteristic seafloors (rough, smooth, target filled) with a reference dataset from a conventional beamforming multibeam echo sounder.

## **1.5. Thesis structure**

The thesis will be structured into five chapters:

- Chapter 1 presented a more detailed statement of the problem, the history of work in phase differencing bathymetry, the research questions, and the study objectives.
- Chapter 2 will describe the background knowledge for deriving depths from phase differencing, focusing on the concepts necessary to answer the research questions.
- Chapter 3 will address the methodology used for the algorithm development, detailed equipment characteristics and settings used during field work, implied assumptions, used filters, and imposed limitations.
- Chapter 4 will show the results of each test performed.
- Chapter 5 will discuss the results shown in the previous chapter while trying to answer the research questions, and, in case new questions are unveiled, suggestions for future work will be pointed out.

## CHAPTER 2: BACKGROUND

### 2.1. Definition

Phase measuring bathymetric sonars (PMBS) are sensors that use multiple parallel line transducer arrays to receive sound waves in the water so that the elevation angle relative to the sonar in the side plane is assessed as a function of the difference in the time the received wavefront excites a pair of these elements. The net result is that a depth may also be derived.

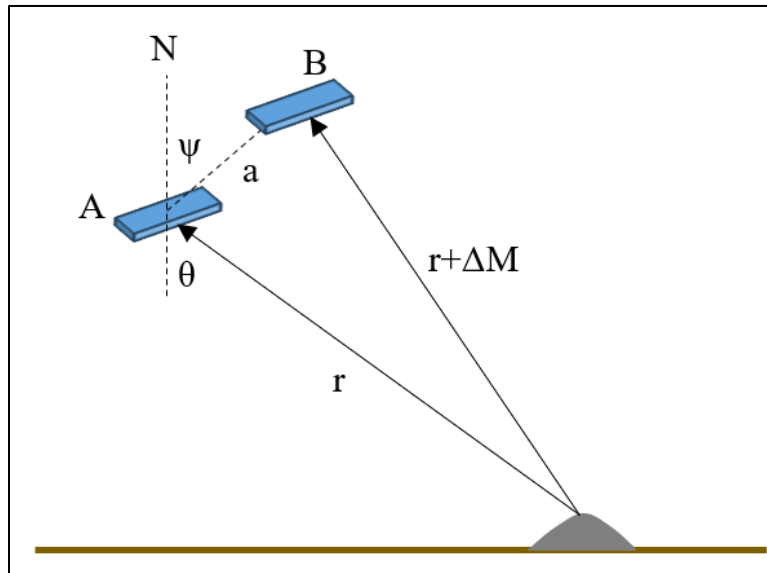


Figure 2 – Differential phase geometry from a tilted stove pair.

Figure 1 shows the generic geometry of a wavefront arriving at a pair of staves A and B in a plane normal to the long axis of the line arrays. The sound is transmitted from the sounder and interacts with the seafloor continuously as the transmitted wavefront expands to lower grazing angles. From this scheme, it is possible to perceive that the difference in the time of arrival at A and B varies with the Direction of Arrival (DOA). From the co-sine rule, the time difference caused by the incremental slant range  $\Delta M$  is also a function of depth (Equation 2.1).

$$\Delta t = \frac{\Delta M}{c} = \frac{1}{c} \left\{ \left[ \left( \frac{d}{\cos\theta} \right)^2 + a^2 + 2a \arccos(\theta + \psi) \right]^{\frac{1}{2}} - \frac{d}{\cos\theta} \right\} \quad (2.1)$$

Where:

- $\underline{c}$  is the sound speed in the water.
- $\underline{d}$  is the depth.
- $\underline{a}$  is the distance between staves.
- $\underline{\theta}$  is the direction of arrival at stave A.
- $\underline{\Psi}$  is the echo sounder tilt to the vertical (mounting angle).

It is usual to work with PMBSs in the far field so that the wavefronts arriving at the pair of staves could be considered parallel lines. Under this assumption, the problem is simplified as in

Figure 2:

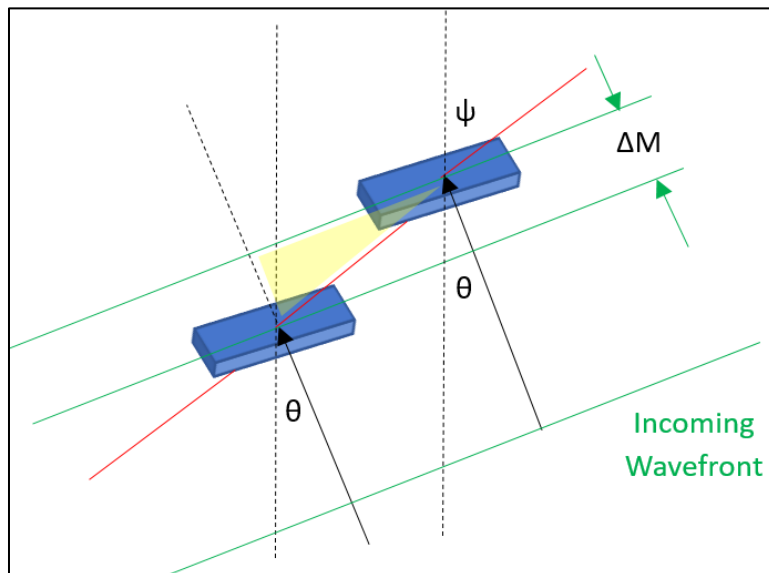


Figure 3 - Phase difference geometry assuming far field.

As both vectors arrive at the staves with the same angle  $\theta$ , a rectangle triangle is obtained as the wavefront (green) displaces from A to B, yielding Equation 2.2:

$$\Delta t = \frac{\Delta M}{c} = \frac{a}{c} \cos(\theta + \psi) \quad (2.2)$$

Due to the short timescales involved, high-cost clocks would be necessary to keep a time register with the required precision for bathymetry. As a result, signal phases are used instead of time, developing hyperboles described by Equation 2.3, equivalent to the split-aperture correlator presented in Burdic (1984, p. 329):

$$\Delta\phi = \omega\Delta t = 2\pi \frac{a}{\lambda} \cos(\theta + \psi) \quad (2.3)$$

Where:

- $\Delta\phi$  is the phase shift between staves A and B.
- $\omega$  is the radian frequency of the incoming wave.
- $\lambda$  is the wavelength of the incoming wave.

## 2.2. The phase ambiguity

By comparing phasors, systems can measure instantaneous differential phases between staves. That difference, however, is just the fraction component of the potentially multiple wavelength total phase shift because many integer cycles of phase may have elapsed within the incremental slant range. Thus, Lurton (2008) highlighted that these systems cannot provide phase shifts ( $\Delta\phi$ ) directly, but only the phase differences ( $d\phi$ ), related by Equation 2.4:



$$\Delta\phi = d\phi + 2\pi m, m \in \mathbb{Z} \quad (2.4)$$

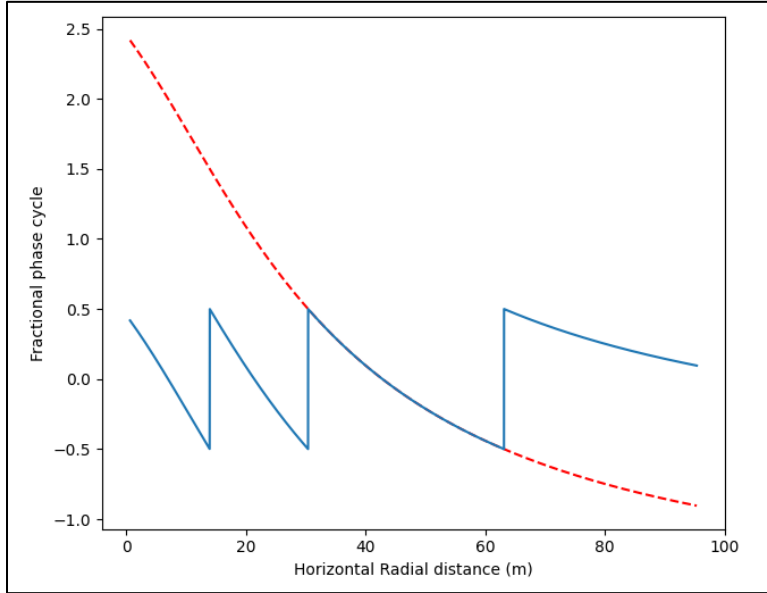


Figure 4 - Example of theoretical phase shift (red) and phase difference (blue) curves for an EdgeTech 6025 3-lambda spaced stave pair, with a mounting angle of 35° sitting 30 m above a flat surface.

### 2.3. Differential phase computation

As mentioned, a complex phasor is measured in each stave for each instant. Therefore, from the property of the product of complex numbers  $z_1$  and  $z_2$ , the phase difference can be obtained as follows:

$$z_1 = a_1 + jb_1 = A_1 \angle \phi_1$$

$$z_2 = a_2 + jb_2 = A_2 \angle \phi_2$$

Their product is equal to:

$$z_1 z_2 = A_1 A_2 \angle (\phi_1 + \phi_2)$$

Then, by using the complex conjugate of  $z_2$ , the phase difference can be obtained in a computationally efficient way, as presented in Lurton (2008):

$$\begin{aligned} z_1 z_2^* &= A_1 A_2 \angle(\phi_1 - \phi_2) \\ \theta_1 - \theta_2 &= d\phi = \arg(z_1 z_2^*) \end{aligned} \quad (2.5)$$

The complex product  $z_1 z_2^*$  is very meaningful. According to Burdic (1984, p. 209), this product contains information concerning the similarity in the form of two signals. Not only the phase difference can be obtained from it, but also it can also provide the geometric mean of the signal intensity in both staves, expected to be approximately equal:

$$\begin{aligned} I_1 &= \frac{A_1^2}{2}; I_2 = \frac{A_2^2}{2} \\ \bar{I} &= \sqrt{I_1 I_2} = \frac{1}{2} A_1 A_2 \\ \bar{I} &= \frac{1}{2} \text{abs}(z_1 z_2^*) \end{aligned} \quad (2.6)$$

#### 2.4. Estimating DOAs from differential phases

Substituting (2.4) into (2.3), and given that the transducers were designed to limit the received energy to the semi-plane facing the array, such that  $(\theta + \psi) \in [0, \pi]$ , the DOA candidates  $\underline{\theta}$  can be expressed as a function of the phase differences computed by (2.5) by the following model:

$$\theta = \arccos \left[ \frac{d\phi + 2\pi m}{2\pi \left(\frac{a}{\lambda}\right)} \right] - \psi, m \in \mathbb{Z} \quad (2.7)$$

Where  $\underline{\theta}$  is an array containing multiple possible directions of arrival, depending on the assumed phase cycle  $\underline{m}$ . The problem of having multiple solutions, called phase ambiguity, has been intensively addressed since PMBSs were conceived. Before presenting solutions to this issue, it is important to analyze how the ambiguity behaves with the transducer characteristics. Looking at Figure 5, one can notice that when the stave separation  $\underline{a}$  is reduced, the incremental slant range  $\Delta M$  also reduces, limiting the maximum phase cycles that can happen in that distance. As seen in theoretical curves plotted for a flat seafloor, the more spaced the staves are, the larger phase shifts can be achieved, causing more phase jumps in the time domain.

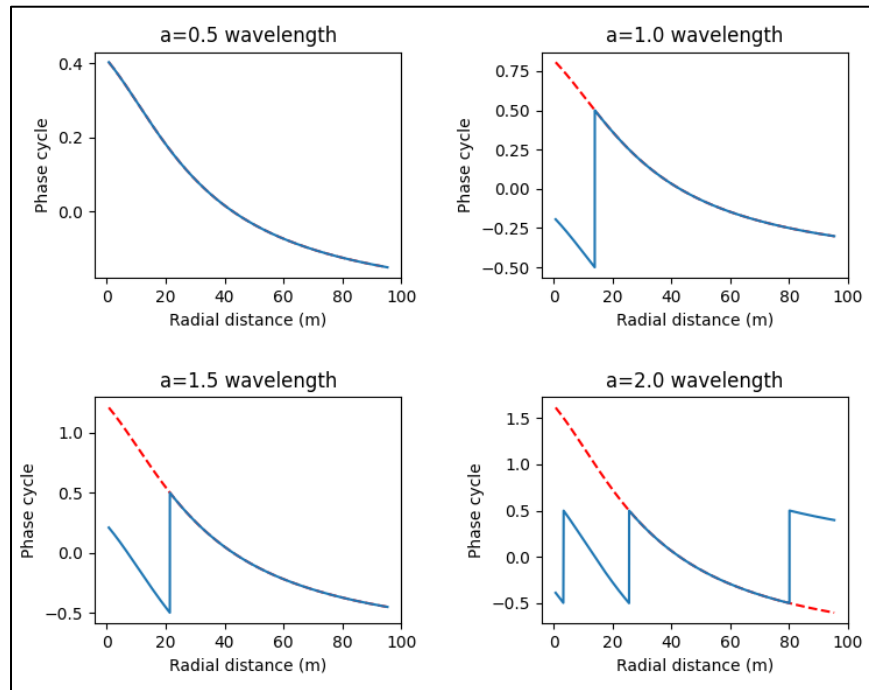


Figure 5 - Phase shifts (red) and Phase differences (blue) for an EdgeTech 6205 distinct stave spacings, with a mounting angle of  $35^\circ$  sitting 30 m above a flat surface.

As seen in Figure 5, upper-left, half-wavelength spaced staves only allow for one phase cycle over the differential distance  $\Delta M$ , having an image contained into the interval  $[-\pi, +\pi]$ . This configuration yields no phase ambiguities. Each time the baseline reaches an integer, a new phase ramp is added to the phase shift image, such that, for example, a three-wavelength spaced pair would yield phase shifts limited in the interval  $[-6\pi, +6\pi]$ , as shown in Figure 6, from Denbigh (1989).

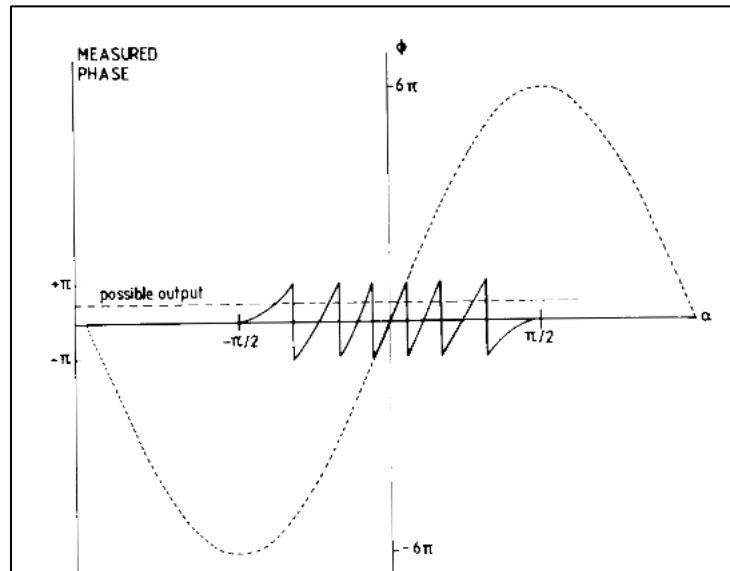


Figure 6 - Phase shift and phase difference curves in the angular domain. Retrieved from Denbigh (1989).

The phase shift image interval has two substantial impacts. First, considering that the nominal standard deviation of a PMBS for the phase measurement is  $\underline{\sigma}_P$ , Equation 2.3 can be differentiated under the law of propagation of uncertainty to find the angular standard deviation as a function of  $\underline{\sigma}_P$ , resulting in the following expression:

$$\begin{cases} \Delta\phi = \phi_1 - \phi_2 \therefore \sigma_{\Delta\phi}^2 = \sigma_p^2 + \sigma_p^2 = 2\sigma_p^2 \text{ (I)} \\ \sigma_{\Delta\phi}^2 = \left(\frac{\partial\Delta\phi}{\partial\theta}\right)^2 \sigma_\theta^2 \text{ (II)} \end{cases}$$

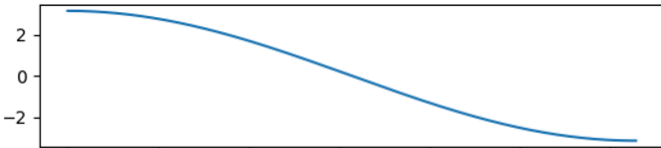
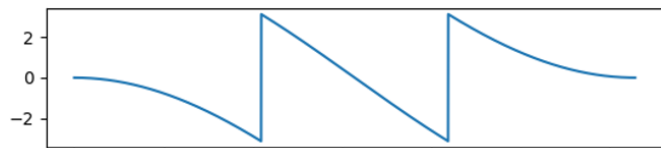
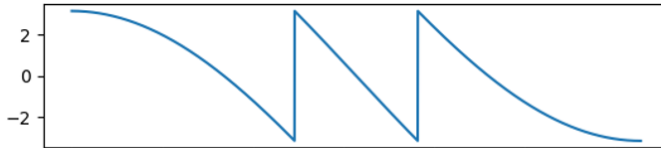


Then:

$$\sigma_\theta = \sigma_p \times \frac{\sqrt{2}}{2\pi b |\sin(\theta + \psi)|} \quad (2.8)$$

Where  $\underline{b}$  is the stave spacing per wavelength ( $a/\lambda$ ). From Equation 2.8, the angular standard deviation for a given angle is inversely proportional to the stave spacing. The same conclusion can be drawn from Figure 5, as the same range of angles is calculated from a larger set of phase shifts, depending on that spacing. Besides that, some applications that use phase zero crossings, such as MBES phase detection, also benefit from longer baselines because the hyperboles tend to cross the x-axis with less acute angles, resulting in a better estimate of the center of the ensonified area (footprint) on the seafloor.

Second, the stave spacing determines the number of viable solutions for the DOA in each instant. From the half-wavelength spaced staves, where only one value of the phase cycle  $\underline{m}$  is possible, each time the stave spacing is incremented to a new integer, a new possible phase ramp is added to each side of the phase difference curve in the angular domain, adding two possible values of  $\underline{m}$  every integer lambda spacing, as described in Table 1.

Table 1 - Phase cycle number ( $m$ ), depending on the stave spacing  $b = (a/\lambda)$ .

Stave Spacing $\underline{b}$	Phase difference curve expected	Values of $\underline{m}$ (phase ramp number)
0.5		0
1.0		-1, 0, 1
1.5		-1, 0, 1
2.0		-2, -1, 0, 1, 2
2.5		-2, -1, 0, 1, 2
Generic $\underline{b}$	-	$m_{max} = 2 \times int(b) + 1$

In conclusion, the set of viable solutions  $\underline{\theta}$  from a stave pair can be calculated with Equation 2.7 by iterating  $\underline{m}$  within the possible values, depending on the stave spacing for that pair.

## 2.5. Phase disambiguation

One of the most used methods to solve phase ambiguities is the Vernier Method, which compares the solutions of two stave pairs with different spacing. Although each will provide a series of possible angles, only one value will repeat in both sets, being the correct solution. As described in Llord-Pujol et al. (2008), Equation 2.7 can be developed for two staves,  $\underline{1}$  and  $\underline{2}$ , establishing the following relationship:

$$\cos(\theta + \psi) = \frac{d\phi_1}{2\pi b_1} + \frac{m_1}{b_1} = \frac{d\phi_2}{2\pi b_2} + \frac{m_2}{b_2}, (m_1, m_2) \in \mathbb{Z}^2 \quad (2.9)$$

In reality, each stave phasor will have an SNR, making them disagree, so the closest co-sines from both sets may be averaged to reach the best estimate for the final solution.

$$\cos(\theta + \psi) = \frac{\cos(\theta_1 + \psi) + \cos(\theta_2 + \psi)}{2} \quad \left| \cos(\theta_1 + \psi) - \cos(\theta_2 + \psi) \right| = \min(\varepsilon) \quad (2.10)$$

Where  $\underline{\varepsilon}$  is an error set containing the differences  $|\cos(\theta_1 + \psi) - \cos(\theta_2 + \psi)|$ , after iterating through all possible  $\underline{m}_1$  and  $\underline{m}_2$ .

The Vernier solution can fail if the noise is so big that a wrong co-sine is chosen in the minimization function. It happens more frequently for longer stave spacings because the difference between consecutive terms ( $m_i/b$ ) between cycles gets smaller as  $\underline{b}$  increases, making the algorithm less tolerant to noise. Llord-Pujol et al. (2008) defines an efficiency metric to evaluate the best baseline combination ( $b_1, b_2$ ):

$$eff_{1,2} \triangleq \frac{1}{2} \min \left| \frac{m_1}{b_1} - \frac{m_2}{b_2} \right|, (m_1, m_2) \neq (0,0) \quad (2.11)$$

## 2.6. Deriving depths

A PMBS records the time of transmission and then samples phase differences at a constant sampling interval. Thus, the time interval between transmission and reception (TWTT) is given by:

$$TWTT = t_{trans} + offset + SI \times n \quad (2.12)$$

Where:

- TWTT is the Two-Way Travel Time.
- t<sub>trans</sub> is the time of transmission.
- offset is the cooldown time from transmission until the system starts listening.
- SI is the sampling interval.
- n is the sample number in that transmission.

From that, each sample defines a circular geometric locus from the transducer array. Then, the intersection between this locus and the DOA results in an unambiguous position vector in the echo sounder frame. The beam vector is, then, rotated to the local reference frame using instantaneous pitch, roll, and yaw, measured by an inertial unit so that a horizontally layered ocean model can be used to ray trace the sound path in the water column. From this process, a depth, and a radial distance with respect to the transducer frame can be obtained. Finally, it is possible to derive positioning for each resolved sounding by combining the sounding vector with the GNSS



input. For illustrative purposes, a simplified relation can be used, assuming a homogeneous sound speed field, implying the sound made a straight path in the water:

$$SR = c \times \frac{TWTT}{2} \quad (2.13)$$

$$h = -d = -SR \cos \theta \quad (2.14)$$

$$x = SR \sin \theta \quad (2.15)$$

Where:

- SR is the slant range.
- h is the height (z-axis positive up)
- d is the depth w.r.t. the transducer.
- x is the radial distance from the transducer.

The processing of the port and starboard arrays is identical, but the resultant DOAs are relative to each transducer. In order to provide angles in a unified reference frame, EdgeTech (2022) defines the starboard direction as positive, registering, then, port solutions as negative angles. This way, Equations 2.14 and 2.15 can be applied directly independent of which array provided the solutions being integrated.

## 2.7. Reducing the depth variance

After converting pairs of slant ranges and DOAs into depths and radial distances, the bottom morphology obtained by a 6205 half-wavelength, unambiguous pair differential phase at a 10-meter depth was well-defined up to about 68° incidence angle, beyond which an unacceptable high depth variance was observed (Figure 7).

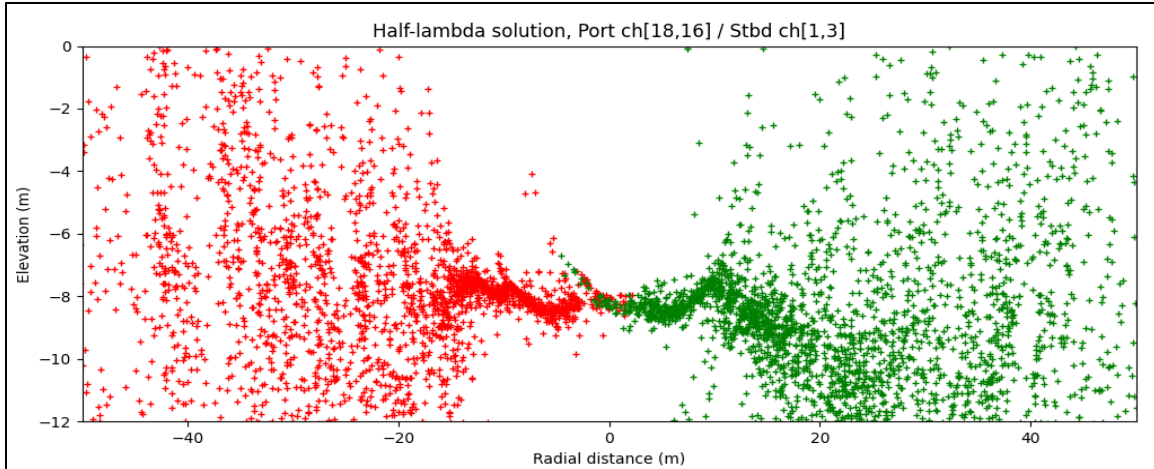


*Figure 7 – Depths calculated from an unambiguous stove pair (for each side).*

This depth variance comes from various factors: phase measurements are naturally noisy, due to the loss of SNR to effects such as the baseline decorrelation and the shifting footprint, described by Lurton (2000), and further explained in section 2.8. Besides, in the far-range, the SNR decay to the transmission loss becomes the limiting factor to delineate the seafloor. Finally, the smaller the stove spacing is (Equation 2.8), the more sensitive is the angular uncertainty to the phase variance, which is the reason for the half-wavelength solution being so noisy.

With the aim to extend useful DOAs to greater ranges, some strategies may be devised to collapse multiple samples into a meaningful averaged result, compensating the SNR loss.

### 2.7.1. Averaging equidistant pairs

According to Equation 2.10, an equal baseline yields  $\text{eff}_{1,2} = 0$ , meaning that the Vernier Method cannot be used to compute solutions from stove pairs with the same baselines. Even so, when equidistant pairs are available, their observables can be averaged to reduce the phase variance, as proved below. This possibility is particularly pertinent to the 6205 under investigation.

The individual element spacing is identical, but combining multiple identically spaced pairs of staves can generate a lower variance virtual stave pair.

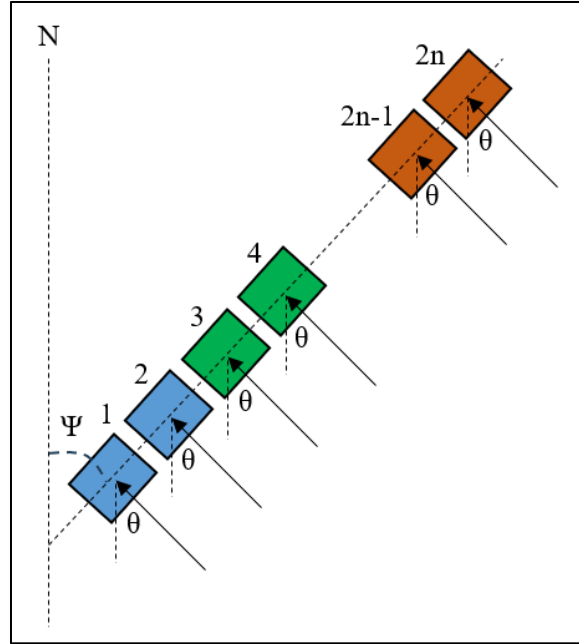


Figure 8 - A PMBS Uniform Linear Array.

Figure 8 shows a ULA of  $2n$  staves. Then, Equation 2.3 can be applied for each of the  $(2n-1)$  stave pairs of this ULA. As the phase differences are being summed, only independent pairs will be averaged so that no phase observable is canceled along the summation. Note that the measuring instant is slightly delayed due to the incremental slant range as the following pair is chosen:

$$\left\{ \begin{array}{l} \Delta\phi_1(t) = \phi_1 - \phi_2 = 2\pi \frac{a}{\lambda} \cos(\theta + \psi) \\ \Delta\phi_3(t + 2\Delta t) = \phi_3 - \phi_4 = 2\pi \frac{a}{\lambda} \cos(\theta + \psi) \\ \dots \\ \Delta\phi_{2n-1}[t + (2n - 2)\Delta t] = \phi_{2n-1} - \phi_{2n} = 2\pi \frac{a}{\lambda} \cos(\theta + \psi) \end{array} \right.$$

Summing the equations for all non-consecutive stave pairs yields:

$$\sum_{i=1}^n \Delta\phi_{2i-1}[t + (2i - 2)\Delta t] = n \times 2\pi \frac{a}{\lambda} \cos(\theta + \psi)$$

For small arrays,  $\Delta t$  is negligible when compared to the sampling interval. Then:

$$\frac{1}{n} \sum_1^n \Delta\phi_{2i-1}(t) = \overline{\Delta\phi} = 2\pi \frac{a}{\lambda} \cos(\theta + \psi) \quad (2.16)$$

And, from the law of propagation of uncertainties:

$$\sigma_{\overline{\Delta\phi}} = \frac{\sigma_{\Delta\phi}}{\sqrt{n}} = \frac{\sigma_P \sqrt{2}}{\sqrt{n}} \quad (2.17)$$

The results of averaging same-spaced pairs can be seen in Figure 9 below. Bottom morphology is now perceived up to about  $75^\circ$  incidence angle, representing a significant improvement in comparison to the half-wavelength solution (Figure 7). The half-wavelength average was implemented as the first conventional method to be used as benchmark in this study.

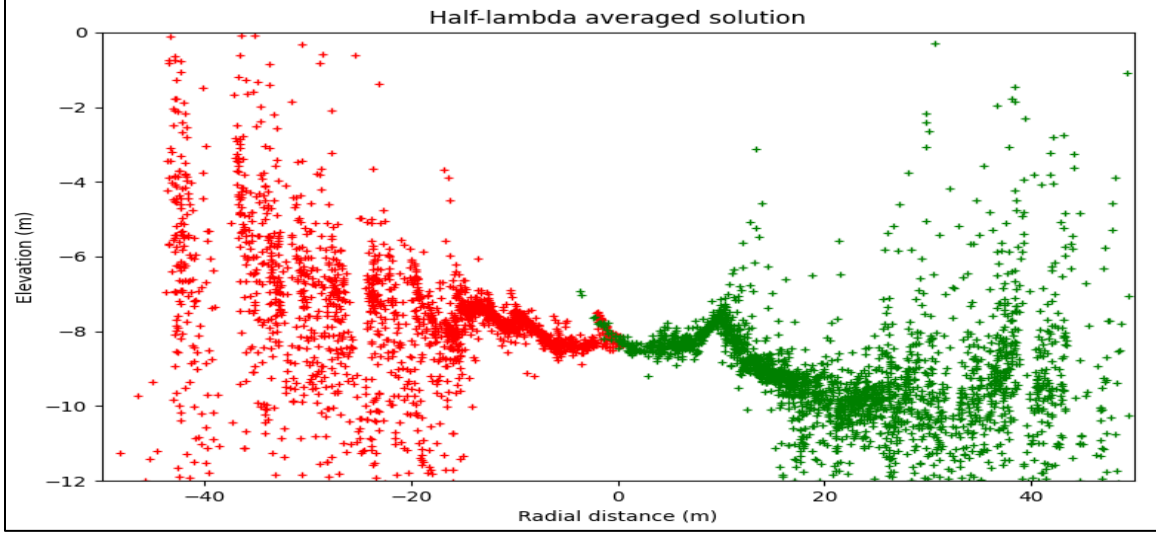


Figure 9 – Depths calculated from the average of all unambiguous pairs' phase differences.

As seen in the derivation of Equation 2.16, there will be some time smearing because the differential phase time series are slightly shifted. This smearing grows with the number of pairs being averaged, depending on the DOA. However, this smearing effect tends to be negligible in small arrays.

An additional remark is that phase differences cannot be averaged as scalar values because distortions would occur with every phase jump. Alternatively, the mean angle can be computed by the circular mean of the normalized products  $z_k z_{k+1}^*$ :

$$\overline{d\phi} = \arg \left( \sum_{i=1}^n \frac{z_{2i-1} z_{2i}^*}{|z_{2i-1} z_{2i}^*|} \right) \quad (2.18)$$

Where  $\underline{n}$  is half the number of staves being averaged. Figure 10 illustrates the average phase difference computation from two normalized products:

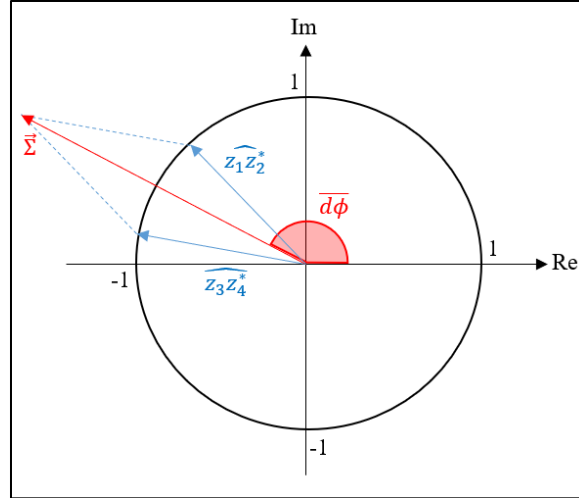


Figure 10 - Circular mean angle.

As the intensity values are a continuum, the mean intensity can be computed from a scalar average:

$$\bar{I} = \frac{1}{n} \sum_{i=1}^n \text{abs}(z_{2i-1} z_{2i}^*) \quad (2.19)$$

### 2.7.2. The Vernier Method

The preceding examples just averaged unambiguous but noisy 0.5 lambda spacing. Given that the 6205 uses ULAs with ten elements half-wavelength spaced, combining more accurate pairs with longer baselines is possible rather than simply choosing adjacent staves to obtain more precise solutions. The second conventional method implemented was a variant of the Vernier method. Unambiguous solutions were already available from the half-wavelength average but, instead of choosing them directly, they were used as a starting point to find more precise angles in the longer baseline pairs. As such, the implementation is described as follows and summarized in Figure 11.

First, a phase average is calculated for each stave spacing available (in this case, from 0.5 to 4.5 wavelengths), yielding one unambiguous and eight ambiguous differential phase averages. Then, by using the unambiguous half-wavelength solution as a first estimate, solutions for ambiguous spacings are progressively found by minimizing the difference between the current estimate and the vector of viable solutions, from the shorter to the longer spacing, from where more accurate solutions can be obtained. The disambiguation was not done directly using the 0.5 wavelength solution for all combinations, because the tolerance to noise decreases the longer are the baselines. At the end of each iteration, a new reference is obtained and used to disambiguate the next spacing. The final solution adopted is the mean of estimates for all spacings evaluated.

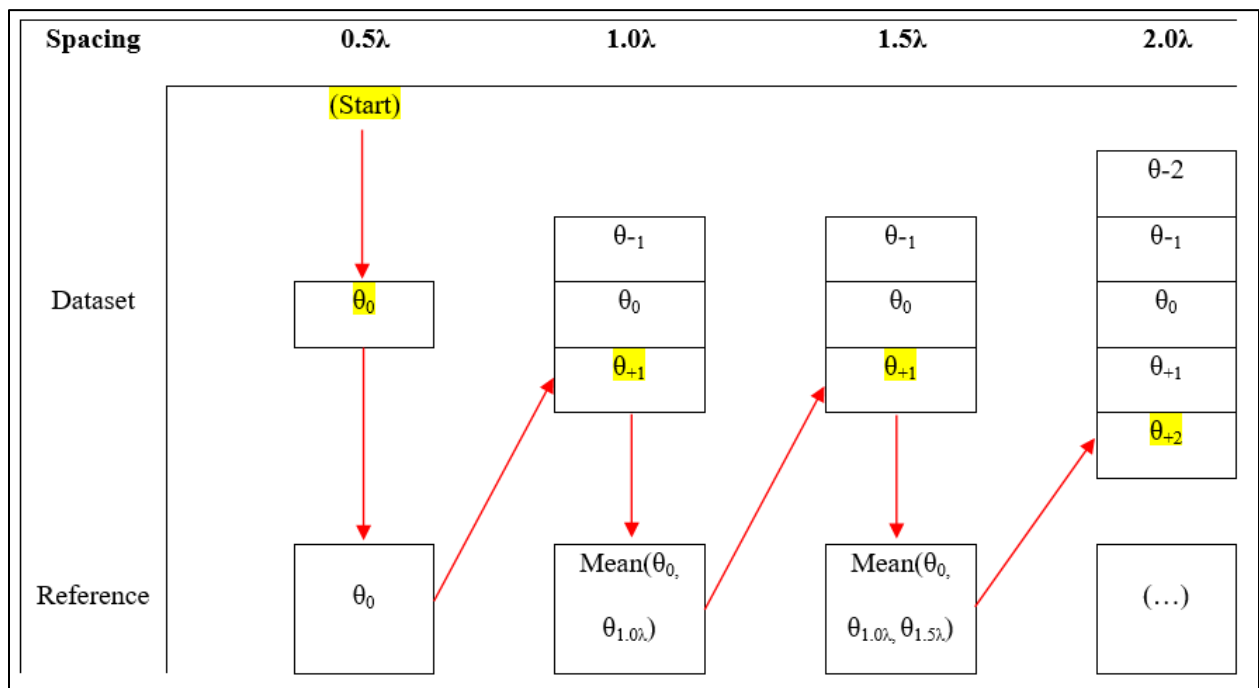
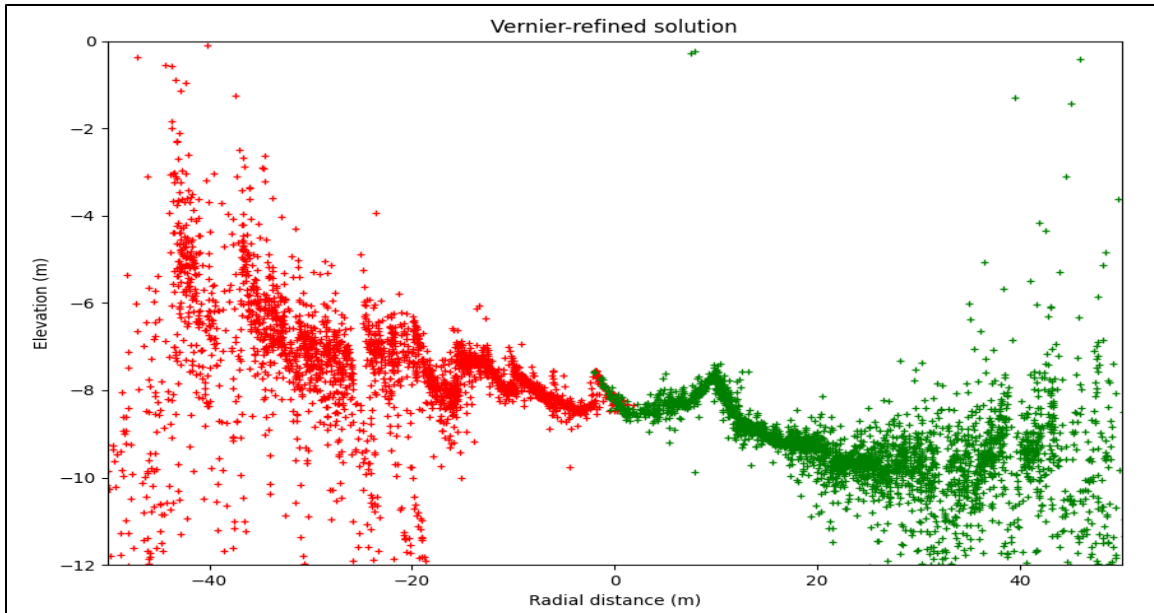


Figure 11 - The Vernier logic used in the algorithm.

After the implementation, depth solutions could be derived more accurately than using only the half-wavelength average, as seen in Figure 12.



*Figure 12 - Depths calculated using the Vernier method.*

After using the Vernier method, the bottom morphology can now be seen up to  $80^\circ$  incidence angle. It is computationally cumbersome, however, and the depths are still considerably noisy. Due to that, an additional way of reducing variance is presented as follows.

### 2.7.3. Time Average

Another strategy to increase the SNR, extending the achievable range, is to assume that groups of samples close in time may be averaged to represent one point at the seafloor. In other words, instead of deriving DOAs for individual samples, one could average a time interval of phase differences, a.k.a. a sliding window, centered at the desired sample, to derive each DOA. In that sense, the mean circle average of a window around the intended sample may be used to calculate the average phase in a process like the one presented in section 2.7.1. Figure 13 below shows a comparison of the achievable range with and without the use of windowing:



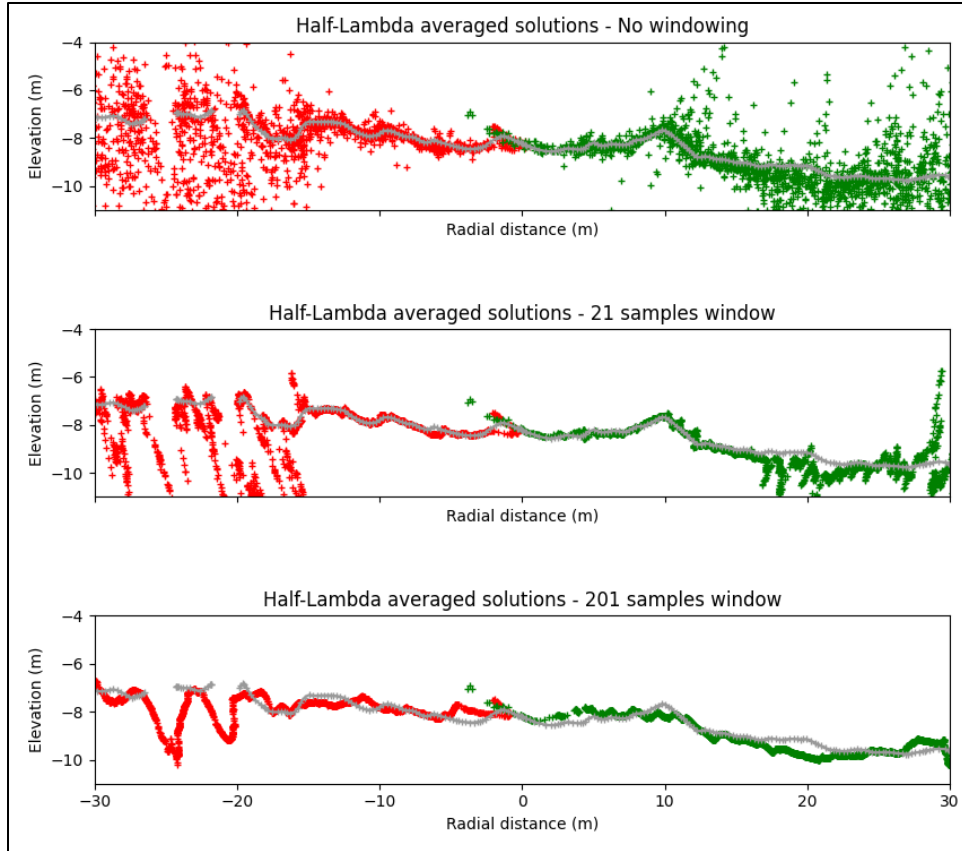


Figure 13 - Depths calculated with different sample windows. EdgeTech solutions in gray.

Figure 13 was made during tests of different window sizes in the sample domain, fixed throughout the swath. During these tests, it was possible to observe that short windows agreed with the EdgeTech solutions in close range. At the same time, larger windows were necessary to collapse far-range samples, because of the phase variance growth with range. However, increasing the window size led to smearing, underestimating targets' heights and causing mismatching (mean difference increase, or bias), notably in close range, where smaller windows would already collapse the solutions. That said, it is clear that window sizes must grow with time, but how this growth would be controlled is a point of needed research. Besides, when setting the window sizes, the developer is basically trading accuracy for across-track resolution.

Lurton (2000) mentions that the window sizes may correspond to a constant angular interval around each sample, or a constant along-track distance, to keep the across-track resolution. The impact of using the latter is accepting some level of smearing at the nadir to achieve the desired maximum achievable range. This study, then, opted for the first method, not to harm target detection at the nadir. This choice brings the benefit of reducing unnecessary smearing, but naturally incurs in loss of across-track resolution with range, as it mimics the output of a conventional equiangular spaced multibeam, thereby having the footprint grow with obliquity.

When an angular subset is taken from the differential phase curve, the ensemble average within the subset returns the differential phase of the center of the subset, multiplied by a factor  $B/\sin(B)$ , where  $B$  is half the angular subset, negligible for a small  $B$ . This is proved below:

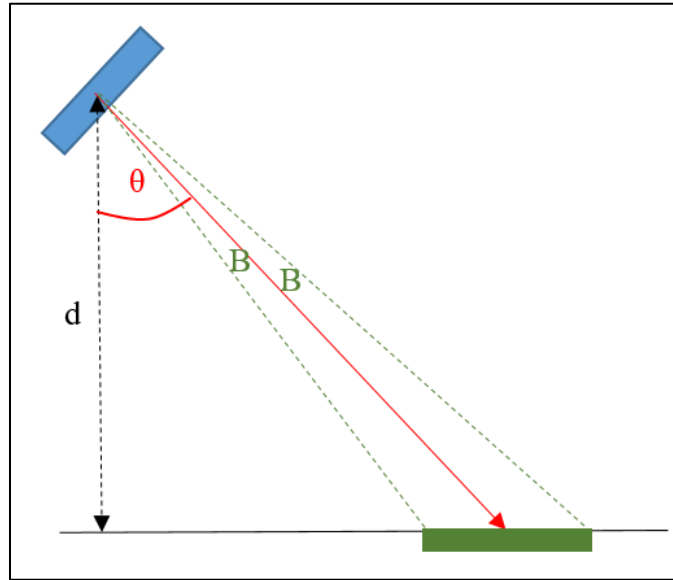


Figure 14 - Time average within an angular subset.

$$\overline{d\phi} = \frac{1}{2B} \int_{\theta_x - B}^{\theta_x + B} d\phi(\theta) d\theta$$

$$\begin{aligned}
\overline{d\phi} &= \frac{1}{2B} \int_{\theta_x-B}^{\theta_x+B} \frac{2\pi a}{\lambda} \cos(\theta + \psi) d\theta \\
\overline{d\phi} &= \frac{\pi a}{B\lambda} [\sin(\theta_x + B + \psi) - \sin(\theta_x - B + \psi)] \\
\overline{d\phi} &= \frac{\pi a}{B\lambda} [2\cos(\theta_x + \psi)\sin(B)] \\
\overline{d\phi} &= \frac{2\pi a}{\lambda} \cos(\theta_x + \psi) \frac{\sin B}{B} \\
\overline{d\phi} &= d\phi_x \frac{\sin B}{B} \\
d\phi_x &= \overline{d\phi} \frac{B}{\sin B} \tag{2.20}
\end{aligned}$$

The window is, then, chosen by setting the desired angular resolution. In this study, a bilateral window varying linearly from  $0.5^\circ$  in close range to  $0.25^\circ$  was chosen so that a resolution comparable to multibeam systems would be used near-nadir and less smearing would be induced in the far range, where the projected window is increased. The basic issue in implementing that is the need for the unknown directions of arrival, so the ensemble limits must be estimated somehow. A possibility of estimating the window limits is using the normal incidence depth, estimated from the first arrival, and assume a flat seafloor. To find the window limits in the sample domain, TWTTs must be calculated with Equation 2.12. The sampling interval and the time offset between the first sample's transmission and reception must be known. Then, using the sound speed at the probe, the window limits are obtained as follows:

$$\text{sample\_limit} = \frac{1}{\text{sampling\_interval}} \left[ \frac{2 \times \text{depth}}{c_{\text{ss\_probe}} \times \cos(\text{est\_DOA} \pm B)} - \text{offset} \right] \tag{2.21}$$

One point to be made is that the angular resolution must be reduced in close range to avoid introducing water column returns in the ensemble average. The estimated DOA under the flat seafloor assumption may be used as window up to the point it reaches the size of  $\underline{B}$ . A similar problem happens at the far-end of the differential phase time series, because the window must be reduced as the evaluated sample approaches the last sample. What remains to be discussed is the impact of using a flat seafloor assumption to estimate the window sizes.

To start with, a simple elevation change is not expected to bias the angle resolved, because the sample limits derived would still deliver a subset angularly symmetric around the evaluated sample (case 1 in Figure 15). That would change the across-track resolution and the ability to collapse depths if the window is smaller than it should be. However, in the presence of a slope (case 2), the flat seafloor window underestimates one of the window edges, making the bisector angle does not match the evaluated sample, therefore introducing some degree of error in the DOA estimation (slope bias).

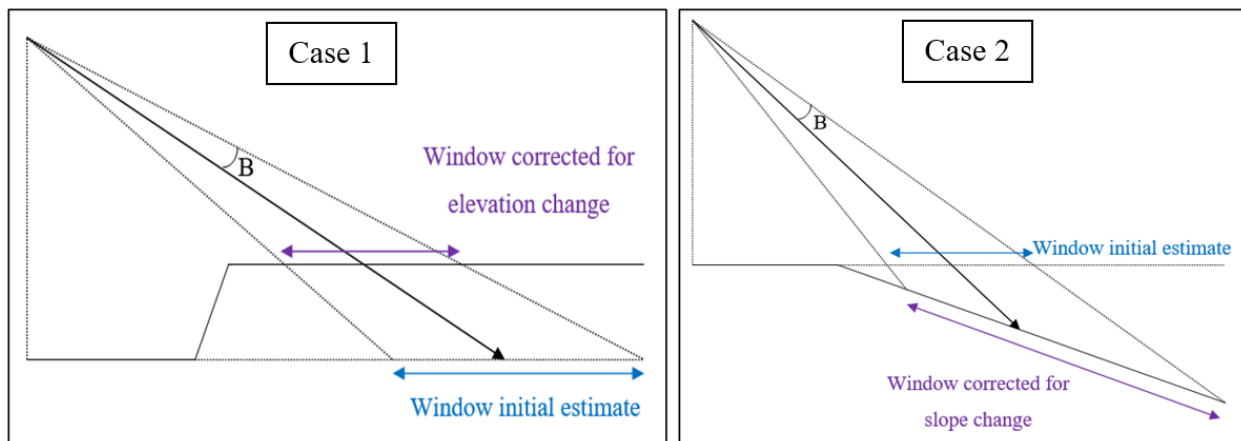


Figure 15 - Flat seafloor assumption impact on windows.

Two ways of dealing with the slope bias were considered. First, the slopes could be estimated recursively, as the samples are processed in time, making it possible to estimate windows corrected for the sloped seafloor (Figure 16), as shown below.

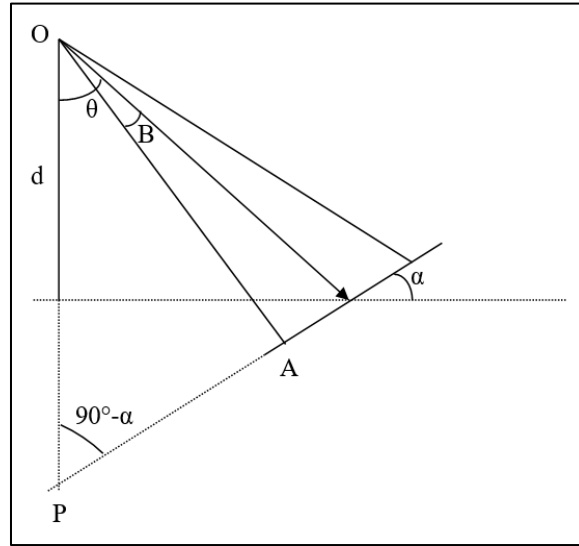


Figure 16 - Sloped angular window limit derivation.

$$\frac{SR}{\sin(90 - \alpha)} = \frac{d + x \tan \alpha}{\sin[90 - (\theta \pm B - \alpha)]}$$

$$\frac{1}{2} TWTT \times ss = \frac{\cos \alpha}{\cos(\theta \pm B - \alpha)} (d + x \tan \alpha)$$

$$TWTT = \frac{2 d \cos \alpha + x \sin \alpha}{ss \cos(\theta \pm B - \alpha)}$$

$$TWTT = \frac{2 SR_{\theta} \cos \theta \cos \alpha + SR_{\theta} \sin \theta \sin \alpha}{ss \cos(\theta \pm B - \alpha)}$$

$$offset + sample\_limit \times SI = \frac{2 SR_{\theta}}{ss} \frac{\cos(\theta - \alpha)}{\cos(\theta - \alpha \pm B)}$$

$$sample\_limit = \frac{1}{SI} \left[ TWTT_{\theta} \frac{\cos(\theta - \alpha)}{\cos(\theta - \alpha \pm B)} - offset \right] \quad (2.22)$$

Equation 2.22 could successfully adapt windows to calculated slopes. However, tests using the slope-adaptive windows induced noisy solutions. Reasons for that may include inaccuracy in the slope estimation due to noise, presence of shadows, etc., or slope variability within the windows. Due to that, this adjustment was not used in the final bottom detection algorithm. Still, it helped in reducing the backscatter image smearing, as explained further in section 2.9.3.

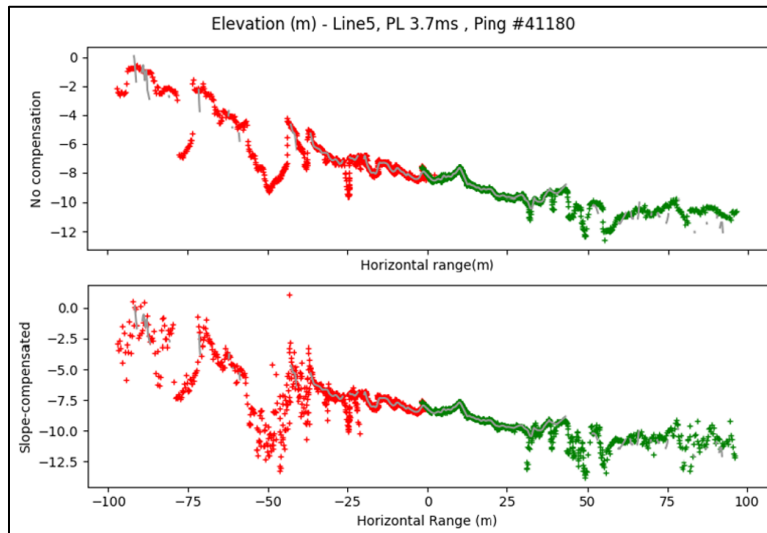


Figure 17 – The effect of window size compensation in bathymetry. EdgeTech solutions in gray.

Another reasonable choice to avoid the slope bias is using a linear regression in the time domain, instead of an average. That would bring the advantage of not necessarily obtaining the bisector angle, as the estimation would be controlled by the sample TWTT, which is precisely known. The disadvantage would be guaranteeing to perform the regression where the differential phase curve has less nonlinearity, which means the window size would need to be small and close to the MRA. Consequently, window sizes would have to consider the main lobe size. The thinner the beam, the more compressed is the differential phase curve, and the smaller must be the window to fit the interval where the differential phase is linear. This directly affects the maximum achievable range.

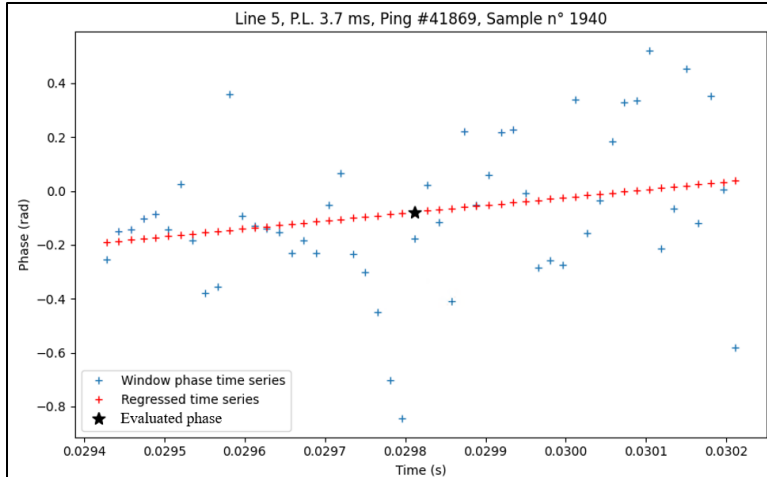


Figure 18 - Using regression (red) within an angular window (blue) to evaluate a sample.

The regression method was not extensively explored in this study, though it yielded similar results to directly averaging samples in the complex domain (Figure 19). This probably happened because the survey area slope was very gentle. In future studies, optimized methods for regression may be explored to improve phase detection results.

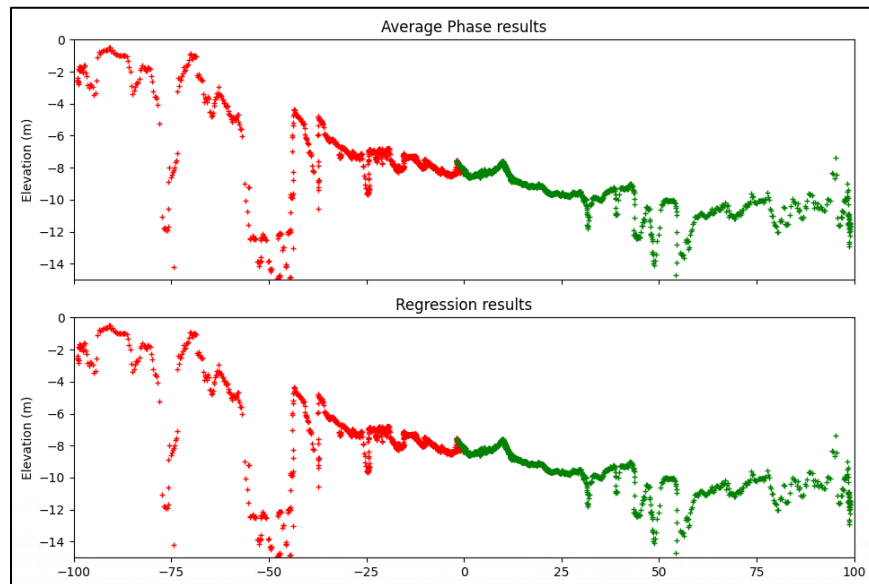


Figure 19 - Average Phase vs. Regression results.

## 2.8. Known issues of phase measuring systems

As mentioned in Chapter 1, there are issues with the PMBS detection, especially near nadir.

Six main reasons can be assigned for degrading sounding quality in these sonars:

### 2.8.1. Lower sampling density

If a phase measurement sensor is sampling evenly in time, potentially with the maximum rate possible, the same cannot be said in the space domain. For each sampling interval  $SI$ , the slant range is increased by half the product of the sound speed in the water and  $SI$ , which yields a smaller horizontal distance between samples as the incidence angle grows. A simulation was made for a flat seafloor to illustrate this effect (Figure 20):

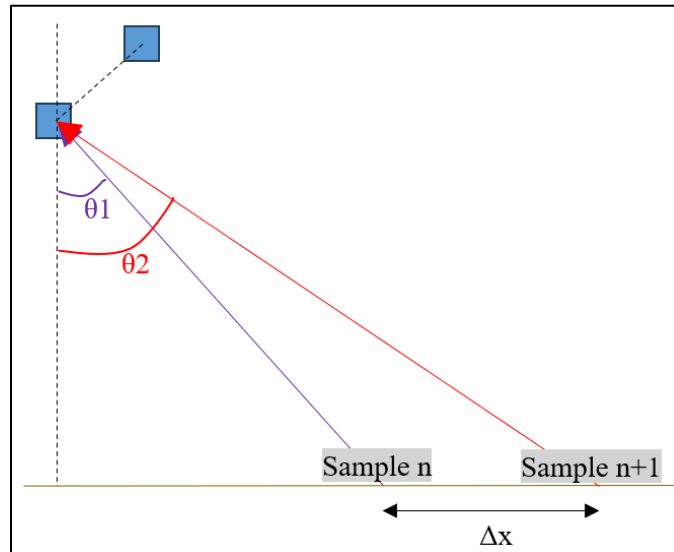


Figure 20 - Differential horizontal distance between adjacent samples.

From Figure 20, the horizontal distance between samples can be derived as follows:

$$\Delta x = r_2 \sin \theta_2 - r_1 \sin \theta_1 = \left( r_1 + \frac{c}{2} SI \right) \sin \theta_2 - r_1 \sin \theta_1 \quad (2.23)$$



Then, plotting a graph  $x$  vs.  $\Delta x$  for a flat seafloor at a 30-meter depth, with a constant sampling interval of  $15.359 \mu\text{s}$  (as used by the EdgeTech 6205), Figure 21 is obtained:

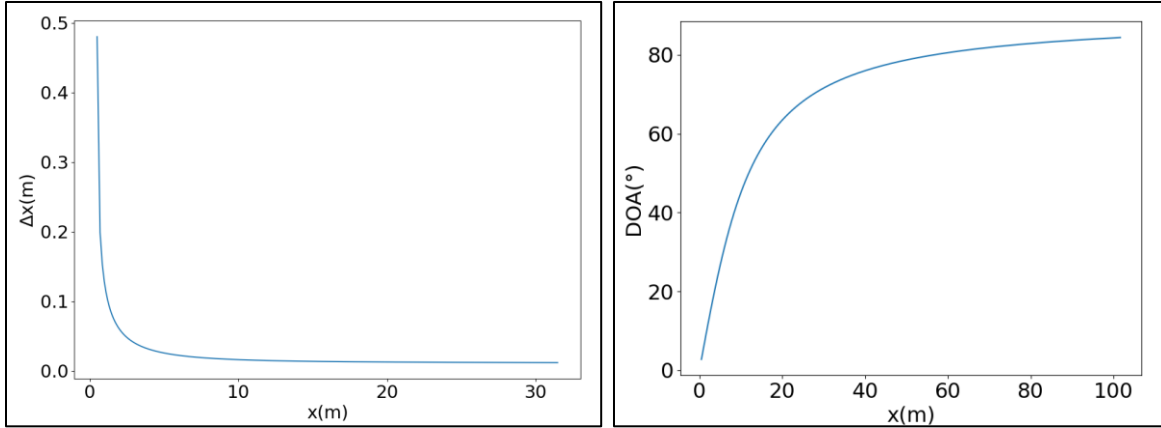


Figure 21 - Differential horizontal spacing and DOA vs. Horizontal Range.

As seen in Figure 21, as the horizontal distance grows, the incremental DOA between samples gets smaller when the DOAs approach the limit  $90^\circ$ . Because of that, the asymptotic behavior of Equation 2.23, shown in Figure 21, can be explained as follows:

$$\lim_{\theta_1 \rightarrow \theta_2 \rightarrow 90^\circ} \Delta x = \left( r_1 + \frac{c}{2} SI \right) \sin 90^\circ - r_1 \sin 90^\circ$$

$$\lim_{\theta_1 \rightarrow \theta_2 \rightarrow 90^\circ} \Delta x = \frac{c}{2} SI \quad (2.24)$$

In this simulation, at about a 30-meter horizontal range, the density due to geometry is approximately constant, in the order of magnitude of 11.5 mm. Still, the separation from the first sample in the horizontal axis to the following reaches almost 0.5 m, rapidly reducing as sampling continues.

To sum up, as the DOA relative to the sounder plate increases, the samples are less horizontally spaced. Hence, density naturally increases from the nadir to the edges of the swath. Most systems make horizontal averaging to smooth solutions in a process called binning. As a result, the smoothed data may have the same density throughout the swath, though oblique bins have many more averaged solutions than near-nadir bins.

### 2.8.2. Inherent nadir interference

Because a side scan sonar's stave is narrow in elevation, it is sensitive over a broad range of elevation angles and thus it can receive signals from multiple simultaneous directions. When those signals arrive simultaneously at the receiving transducer, it is excited by their interfered sum. In contrast, receiver beamforming systems like MBESs can restrict the range of elevation angles within narrow beams. Suppose the simultaneous arrival of two interfering signals. The resultant phase of the summed sinusoidal functions is another sinusoidal function with the same frequency but a changed phase according to the amplitude of each signal:

$$A\cos(\omega t + \phi_1) + B\cos(\omega t + \phi_2) = C \cos(\omega t + \phi_3) \quad (2.25)$$

Where:

$$C = \sqrt{(A + B)^2 \cos^2\left(\frac{\phi_2 - \phi_1}{2}\right) + (A - B)^2 \sin^2\left(\frac{\phi_2 - \phi_1}{2}\right)}$$

$$\phi_3 = \frac{\phi_1 + \phi_2}{2} - \arctan\left[\frac{A - B}{A + B} \tan\left(\frac{\phi_2 - \phi_1}{2}\right)\right]$$

Consequently, if the DOAs are derived by phase difference, these angles will be shifted depending on the contribution of each summed signal. They may not represent any of the primary sources involved, being understood as outliers in the processing steps. If the signal B is weak ( $B \ll A$ ), it will only slightly change the phase of A, and it will usually be treated as noise. In a system with multiple staves, the signals may interfere in some staves and not in others, so the stronger signal may still be resolved if low amplitude signals and not-agreeing phases are filtered from the computations.

As seen, the algorithms shown so far can only resolve one source per time, resulting in a loss of density every time there is a common slant range geometry. This geometry occasionally happens when a proud target is detected and always in near-nadir (Figure 22). In the first case, it causes the layover effect, a blending of the signal amplitudes reaching the transducer simultaneously, for example, when wrecks' masts appear closer to the nadir than they should in the sonograph. In the latter case, ambiguous signals with powerful echoes coming from the specular reflection interfere with each other, degrading the detection capability.

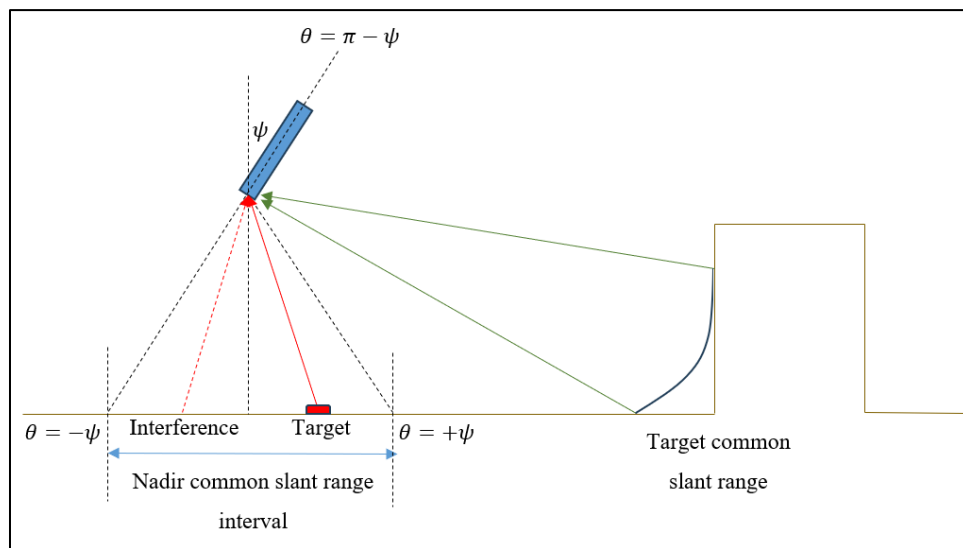


Figure 22 - Common Slant Range. Adapted from Hughes Clarke (2021).

Grall et al. (2020) mention that in a multiple-source environment, more measurements are needed to determine each constituent source's unknown amplitudes and phases. That problem, known as Multi-Angle Bathymetry, was resolved by the CAATI algorithm, devised by Kraeutner (1998). As explained, more equations are used to isolate each constituent, so his algorithm was designed for Uniform Linear Arrays (ULA) with multiple staves spaced at half-wavelength. Although the EdgeTech 6205 was built exactly like that, the system documentation (EdgeTech, 2022) states that only one source is detected at a time, implying that CAATI is not being used in the EdgeTech bottom detection algorithm. By using CAATI, an ULA with  $N$  elements can resolve at least  $\underline{M}=N/2$  sources by using both the amplitude and phase time series. The mathematical model can be found in Kraeutner (1998).

CAATI is more powerful than Vernier solutions, but its spectral model is affected by scintillation and glint across the receive array (Kraeutner et al., 2002). Scintillation is an amplitude distortion that occurs in echoes coming from extended bodies (areas or volumes) that comprises many scatterers, due to the random interference of the individual echoes. When that interference affects the signal phases, the effect is called glint. The more similar scatterers in the footprint, the less these distortions contribute to the signal, so short pulses are more penalized.

### 2.8.3. Baseline decorrelation

The use of long pulses in phase measuring systems can lead to an issue called “baseline decorrelation”. According to Jin & Tang (1996) and Lurton (2000), scintillation and glint may happen within the array at an element distance as small as a staff pair, increasing the differential phase uncertainty. The effect is proportional to the size of the projected footprint on the seafloor, naturally being more penalizing at the nadir – range  $\xi(t_2)$  in Figure 23.

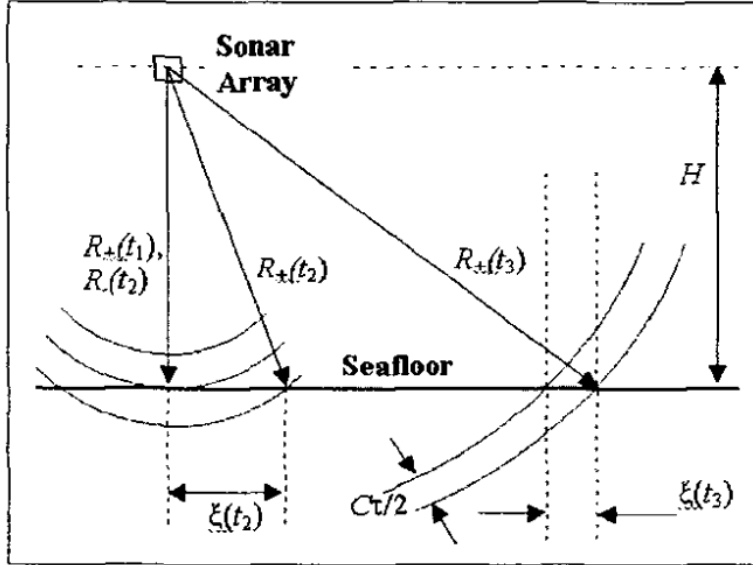


Figure 23 - Projected pulse lengths over different horizontal ranges. Retrieved from Kraeutner et al. (2002).

One estimator influenced by this effect is the field correlation coefficient (Equation 2.26), which represents how much two signals are alike within an ensemble window.

$$\gamma = \frac{|\langle s_a^* s_b \rangle|}{\sqrt{\langle s_a^* s_a \rangle \langle s_b^* s_b \rangle}} \quad (2.26)$$

Jin & Tang (1996) developed Equation 2.26 to model the baseline decorrelation contribution to the field correlation as function of the incidence angle  $\theta$ , depth  $d$ , stave spacing  $a$ , mounting angle  $\Psi$  and pulse length  $\tau$  (notations adapted for consistency with this study), obtaining:

$$\gamma_{bd} \approx \text{sinc} \left[ \frac{\pi a}{\lambda} \times \frac{c\tau}{2d} \cos(\theta) \cot(\theta) \cos(\theta + \psi - 90^\circ) \right] \quad (2.27)$$

Shallow water CW systems are specially degraded by this effect. The 6205, however, was designed to transmit a long FM pulse with a 50kHz bandwidth to counterbalance the heavy absorption loss for working at a high frequency (520 kHz). By making this choice, FM pulses kept the system resolution, but also reduced the effective pulse length, greatly reducing the baseline decorrelation (Figure 24).

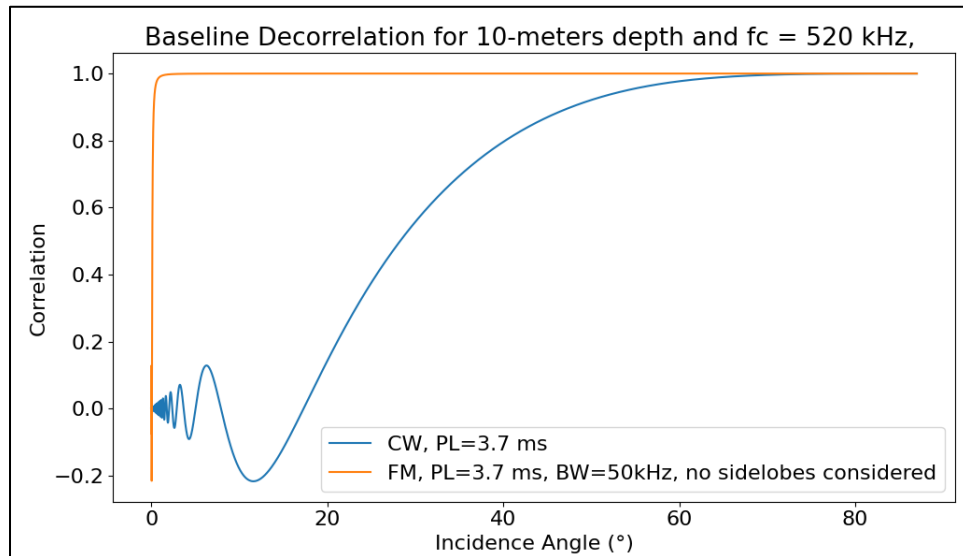


Figure 24 - Baseline decorrelation - CW vs. FM.

It is important to mention that the theoretical decorrelation improvement shown in Figure 24 is over estimated, because side lobes in the pulse compression extend the effective pulse length. This effect is, then, one of the contributors for the 6205 nadir decorrelation, and may be mitigated by applying pulse shaping (Vincent, 2013). Another reason of decorrelation related to frequency modulation is the Doppler heave effect, characterized by shifting and extending the matched filter output when the ship is heaving (Hughes Clarke, 2021).

#### 2.8.4. Shifting Footprint

According to Lurton (2000), there is another effect that affects the differential phase uncertainty, called the “shifting footprint” effect. Suppose a stove pair AB, and a signal that is transmitted from A, reaches a target T, and returns to the array. Although in far-range the DOA differences are negligible, the signal path ATA is slightly shorter than ATB, incurring some degree of decorrelation. What happens geometrically is that the footprint seen by B is slightly shifted inward or outward, depending on its position w.r.t. the transmitter A (Figure 25), causing decorrelation in the edges of the footprint.

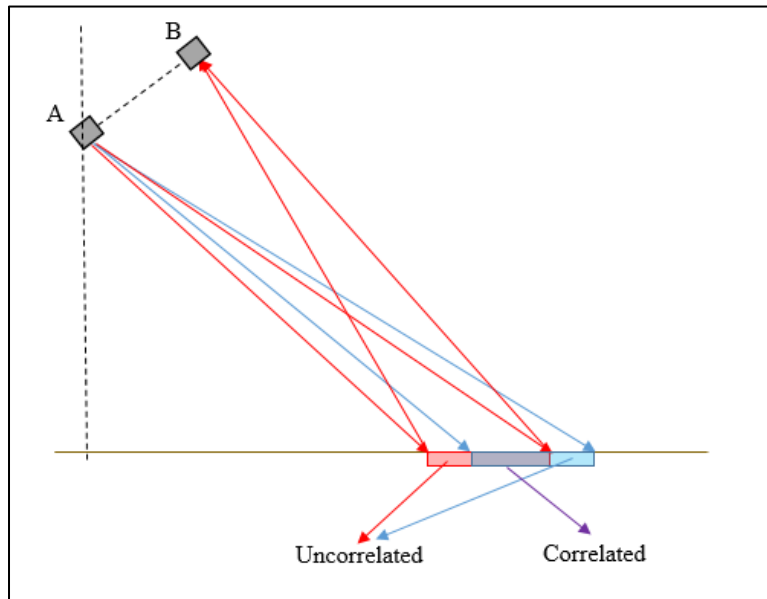


Figure 25 - Shifting footprint.

Lurton (2000) derived an approximation for the shifting footprint effect in terms of SNR, adapted here as a correlation component:

$$\gamma_{sf} = 1 - \frac{2a|\sin(\theta + \psi - 90^\circ)|}{c\tau} \quad (2.28)$$

A simulation made for the 6205 at a 10-meter depth is shown by Figure 26, comparing the baseline decorrelation and the shifting footprint effect, as function of the incidence angle. It is possible to observe that the further the incidence angle is from the array axis at 55°, the bigger is the shifting footprint degradation.

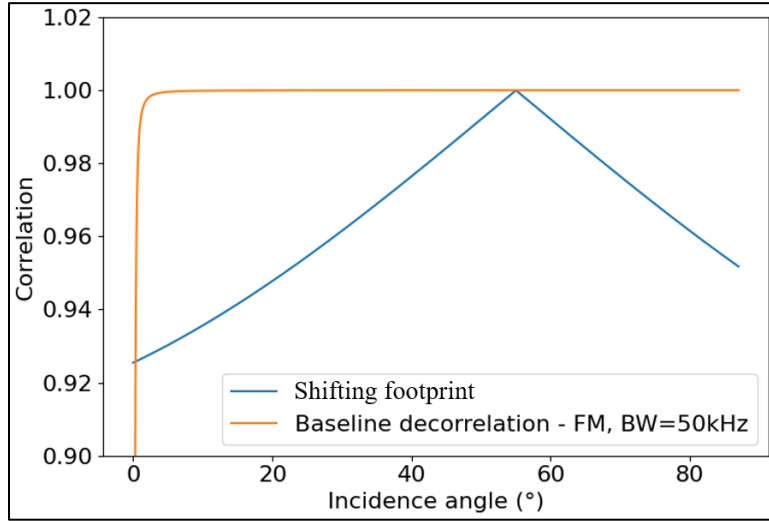


Figure 26 - 6205 shifting footprint vs. baseline decorrelation.

Analyzing Figure 26, it is possible to see that the shifting footprint is the dominant effect at the normal incidence for the 6205 in shallow waters, since it is more penalizing due to the sonar tiny effective pulse length. Regarding the far-range, it is expected that the degrading impact of the shifting footprint is surpassed by the transmission loss from a certain point on.

#### 2.8.5. Angular variance divergence

Equation 2.8 modeled the angular variance sensitivity to the phase variance, as a function of the stave spacing per wavelength  $\underline{b}$  and the DOA. Assuming a constant  $\underline{b}$  of 0.5 and a mounting angle of  $\psi=35^\circ$ , one could plot how the uncertainty sensitivity varies angularly:



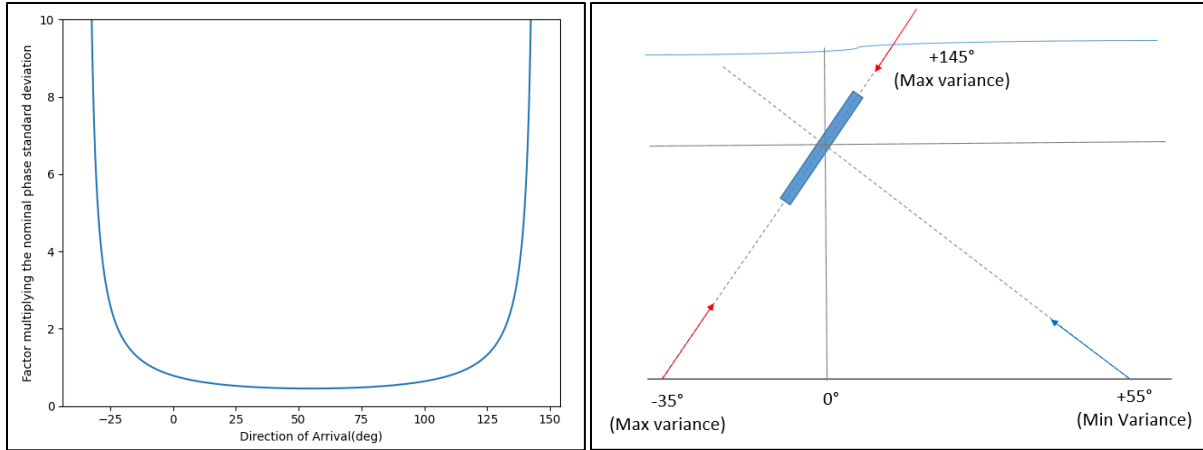


Figure 27 – Incidence angle vs. Angular standard deviation sensitivity for a half-lambda pair and 35° mounting angle w.r.t. vertical.

Figure 27 shows that the angular uncertainty sensitivity is minimum at the transducer axis (perpendicular to the transducer array), in this case at  $\theta=55^\circ$ , and it grows non-linearly as the incidence angles get further from the axis, diverging when  $(\theta+\psi)$  reaches  $0^\circ$  or  $180^\circ$ . In low grazing angles, the increase in variance is compensated for in the binning process due to a more substantial number of samples, as seen previously. The divergence is not perceived in the far range, as the transmission loss is usually the detection's limiting factor. However, the higher variance cannot be compensated in the near-nadir, so the first angles from the phase time series cannot be resolved until a certain incidence angle is reached in the negative angle domain. The unresolved signals still interfere with others arriving simultaneously, in any case.

#### 2.8.6. Multipath

As seen in section 2.7.4, PMBSs are expected to have optimal performance in oblique detection (where MBESs progressively lose resolution), because the angular variance is minimum at the transducer axis, usually directed to mid-range. However, there's also a known issue in oblique detection: the sea surface multipath. The most usual occurrence of multipath has its origins

in the sea surface, which is approximately a pressure release boundary with the air: the wavefronts are totally reflected, as if the water-air interface was a mirror. That reflection can happen both outbound (source-surface-seabed), when the energy is transmitted broadly, and inbound (seabed-surface-receiver), when the receiver sensitivity is broad:

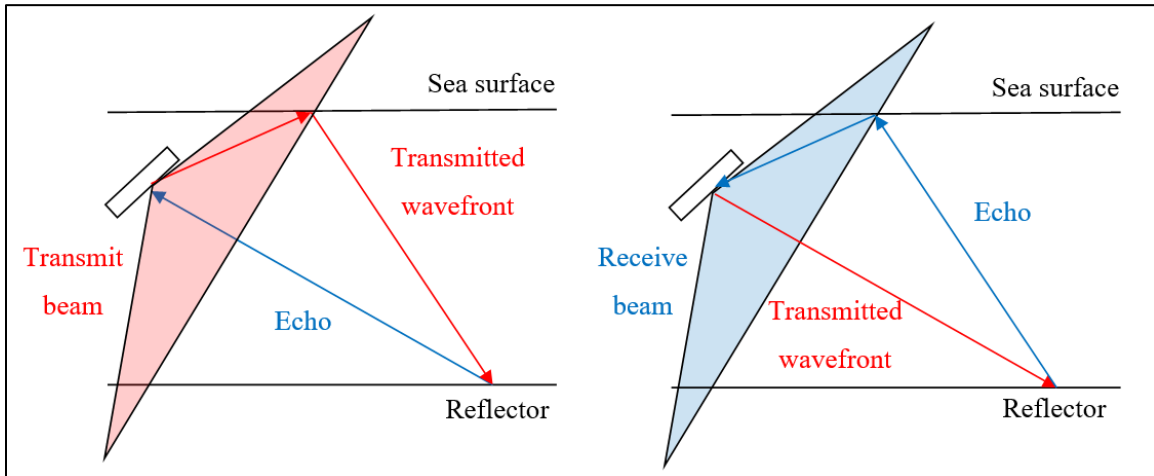


Figure 28 - Outbound Multipath (left) and Inbound Multipath (right).

The multipath signal must travel a longer distance than the direct path, so it is naturally weaker than the latter, and it commonly interferes with following echoes in the time series. The multipath is usually referred to as an oblique detection issue, because, in normal detection, the reflection arrives at the transducer zenith, where it does not have sensitivity. However, in very shallow waters, the signal may be strong enough to make a second two-way travel, these being called multiples. In that case, it may be of concern in the normal incidence detection.

## 2.9. The need for filtering

In averaging phases, incoherent noise and multipath are expected to deviate measurements from their unknown true value. Besides, echoes from sources other than the main direction being

resolved can cause heavy distortions in the measured differential phases, as seen in section 2.8.2. Weak signals from the water column also are of little interest for seafloor surveys. Due to that, it is necessary to establish metrics to evaluate the quality of measurements and, eventually, to filter the data. Although optimal filtering is not a primary concern of this study, quality metrics still are an effective way of comparing different datasets, so the ones developed or used in this study are presented below. More straightforward filtering methods were preferred to optimal alternatives found in the literature, such as the correlation-based bathymetry described in Llorc-Pujol et al. (2012).

### 2.9.1. Phase coherence

Echoes are incoherent when they arrive from different directions, either from distinct sources or from multipath interference, resulting in an inaccurate DOA estimation. Therefore, a phase coherence metric was devised to represent how much the window phasors are aligned between themselves. If  $\underline{n}$  perfectly aligned unity vectors were summed, the magnitude of the resultant vector would be exactly  $\underline{n}$ . If there is not a perfect alignment, their sum will fluctuate between zero, when all vectors point to opposite directions, and  $\underline{n}$  (Figure 29).

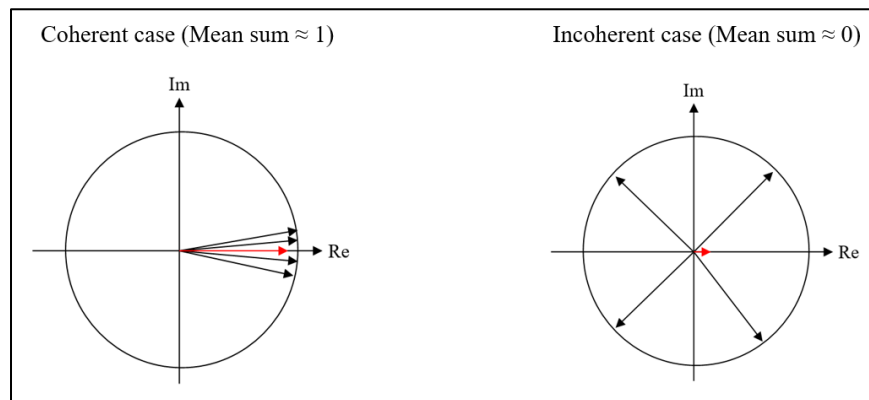


*Figure 29 – Phase coherence parameter computation.*

Therefore, the phase coherence metric was defined as follows:

$$\gamma = \frac{1}{n} \left| \sum_{window} \frac{a_i b_i^*}{|a_i b_i^*|} \right|, \gamma \in [0,1] \quad (2.29)$$

Figure 30 shows a coherence series vs. horizontal range:

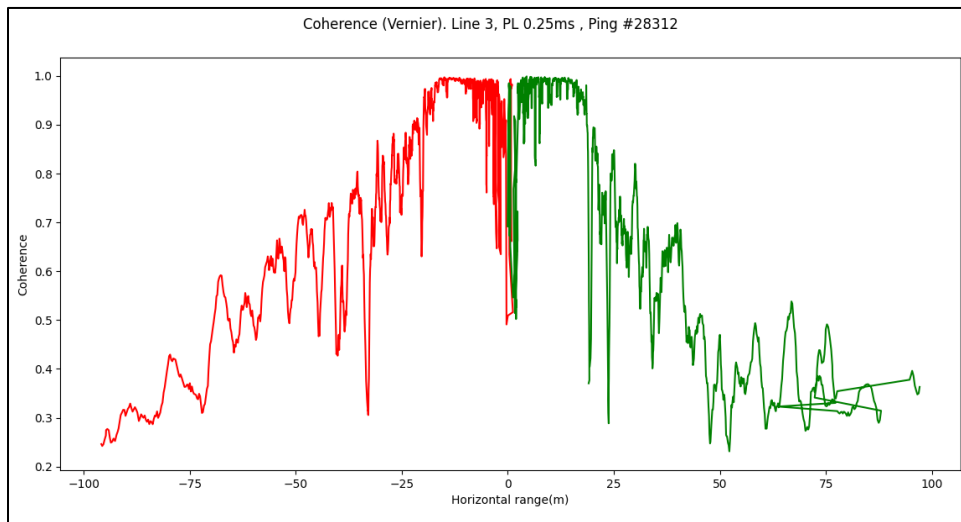


*Figure 30 - Coherence vs. Horizontal Range.*

### 2.9.2. SNR

EdgeTech (2022) mentions that the manufacturer's bottom detection algorithm compares the total signal power at the first arrival with an estimate of the noise plus all multipath echoes to derive a metric called Coherent SNR, used to trim data with significant contributions from sources others than the one being resolved. Guided by that description, an SNR estimate can be calculated in the developed algorithm for each resolved sample using the following logic:

Assuming that the vector sum direction is the best estimate of where the signal being resolved comes from, each complex product can be projected into the vector sum direction to

estimate the amount of intensity coming from the signal direction. The vector difference between the phasor and the projection component represents the amount of intensity coming from other sources. Then, each phasor's total intensity and noise are summed as scalars, and the ratio between those two is the SNR for a given sample.

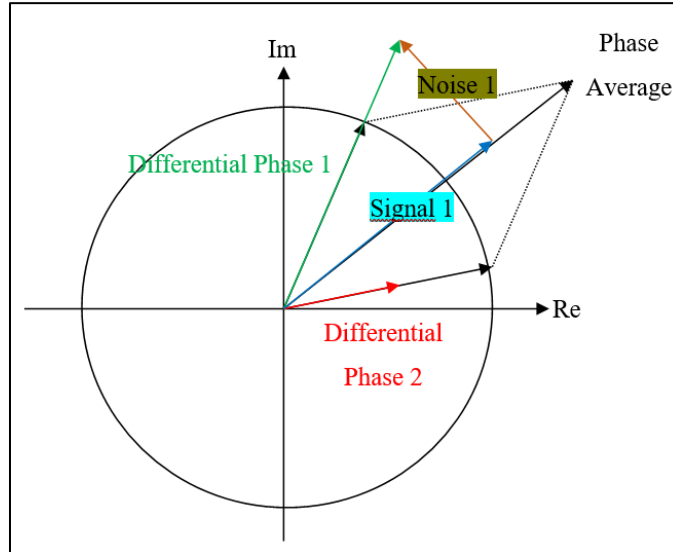


Figure 31 - Decomposing the complex products into their signal and noise component.

$$signal_i = \begin{cases} \text{real} \left( \frac{\langle a_i b_i^*, sum \rangle}{|sum|} \right), & \text{if } signal_i \geq 0 \\ 0, & \text{otherwise.} \end{cases} \quad (2.30)$$

$$noise_i = \left| a_i b_i^* - signal_i \times \frac{sum}{|sum|} \right| \quad (2.31)$$

$$SNR = 10 \log_{10} \left( \frac{\sum_{window} signal_i}{\sum_{window} noise_i} \right) \quad (2.32)$$

The SNR is especially useful to filter shadowed areas. Shadows usually result in bad quality data because returns from there do not travel in a direct path, bouncing and diffracting in the way. That is also the reason why only a small portion of the transmitted energy can make the two-way travel, inherently having low SNR. Figure 32 shows an example of the SNR time series:

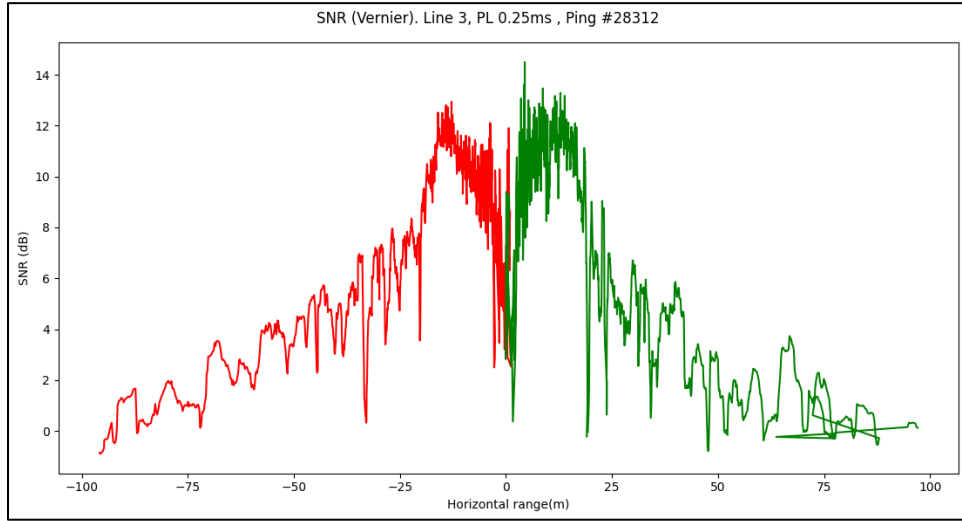


Figure 32 - SNR vs. Horizontal Range.

### 2.9.3. Window intensity

The window total intensity may be divided by the window size to obtain the mean intensity at each sample DOA. This intensity is filtered from the interference of other sources to a certain extent, as it is derived from the signal component seen above.

$$window\_intensity = \frac{1}{window\_size} \sum_{window} signal_i \quad (2.33)$$

The window intensity is used to filter weak signals, such as water column returns, because the first arrival estimation may give a loose value. Figure 33 shows an example of the window intensity time series (over the water column threshold):

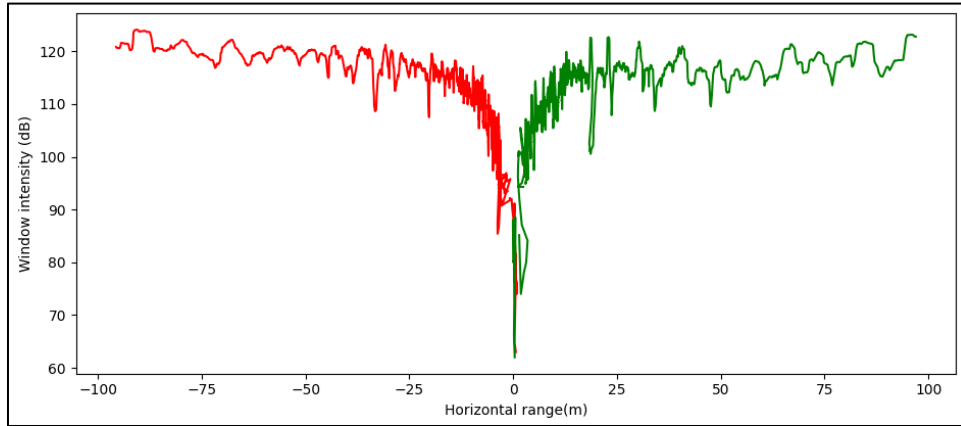


*Figure 33 - Window intensity vs Horizontal Range (water column not included).*

In addition, window intensities can be used as a backscatter product, complementing the side scan image. Figure 34 and Figure 35 shows, respectively, a side scan image, and the backscatter (window intensity) grid. The images were geo-referenced by interpolating the images' sample times in an integrated bathymetry database. TVG and beam pattern correction were applied, as described below. The TVG is used to compensate for the spherical spreading and the absorption in the ocean, according to the following equation:

$$TVG_{db} = 40\log R + 2\alpha R \quad (2.34)$$

Where  $R$  is the slant range and  $\alpha$  is the absorption coefficient in dB per distance. In turn, the beam pattern correction used was the product of an estimate of the transmit beam pattern and the theoretical receive beam pattern, resultant of array processing techniques used in this study.

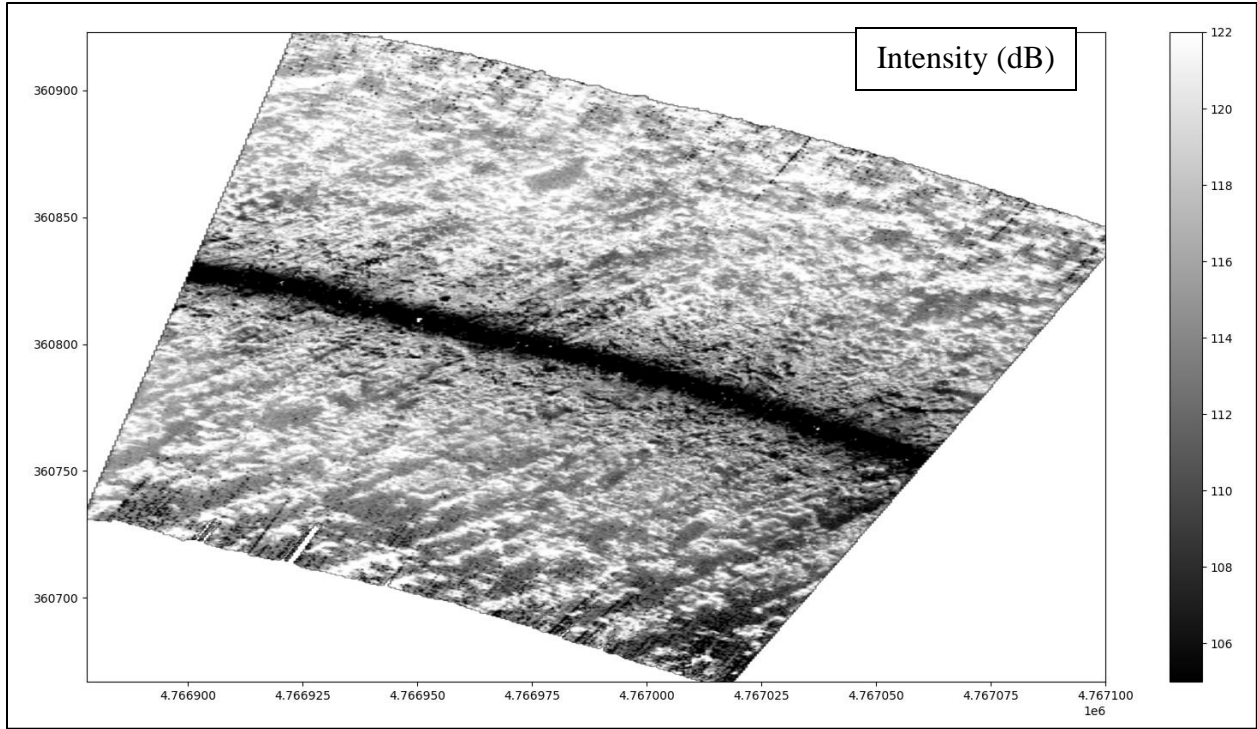


*Figure 34 - Side scan image from a 6205 line, P.L. 3.7 ms.*

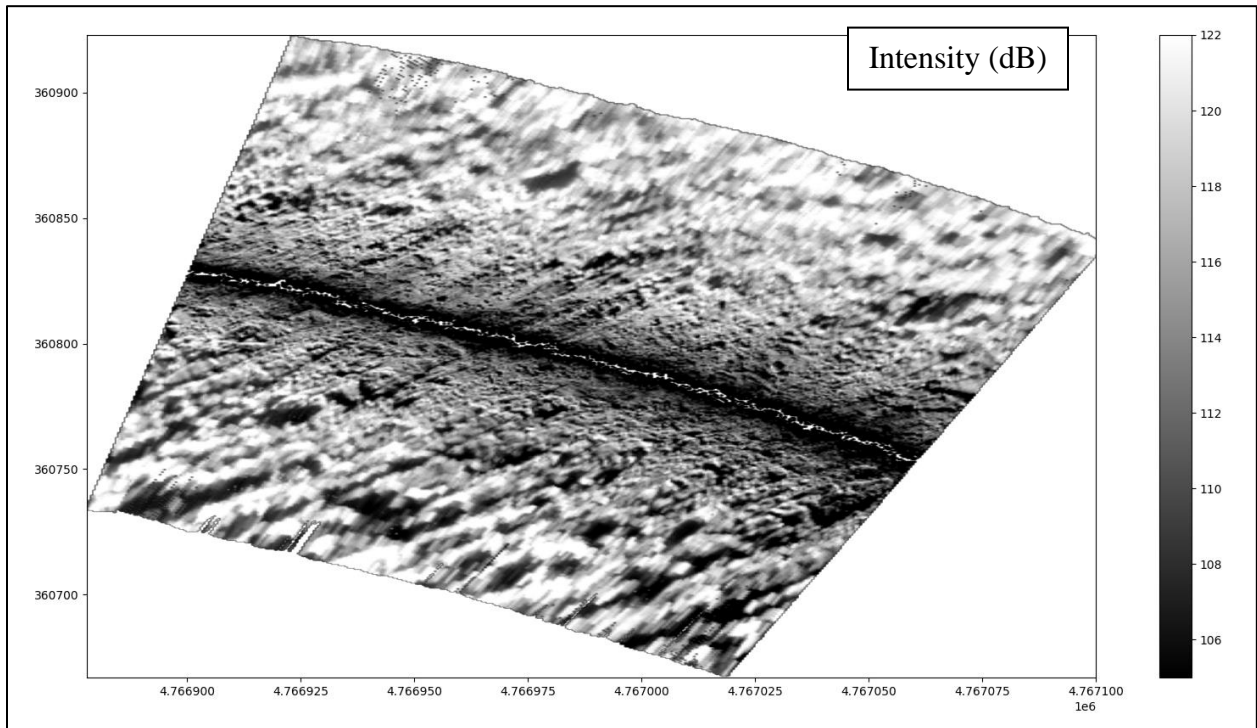


*Figure 35 - Backscatter image from a 6205 line, P.L. 3.7 ms.*



By comparing Figure 34 to Figure 35, it is possible to notice that the backscatter image is less noisy than the side scan image. This happens because the window averaging reduced the speckle variance and filtered some interference, as only the signal component from the SNR was used to compose the image. However, in the far range, severe smearing is observed. After looking into that problem, the reason behind the smearing was found to be the window proportions being distorted by the seafloor slope. The effect of the resolution change with slope, mentioned in section 2.7.2, though not helping in the bathymetry processing, aided in achieving a proper backscatter average. Figure 36 is the backscatter grid obtained by the slope-corrected window algorithm. The smearing was mitigated by the slope correction, indicating that the window proportions are important to achieve a sharper image.

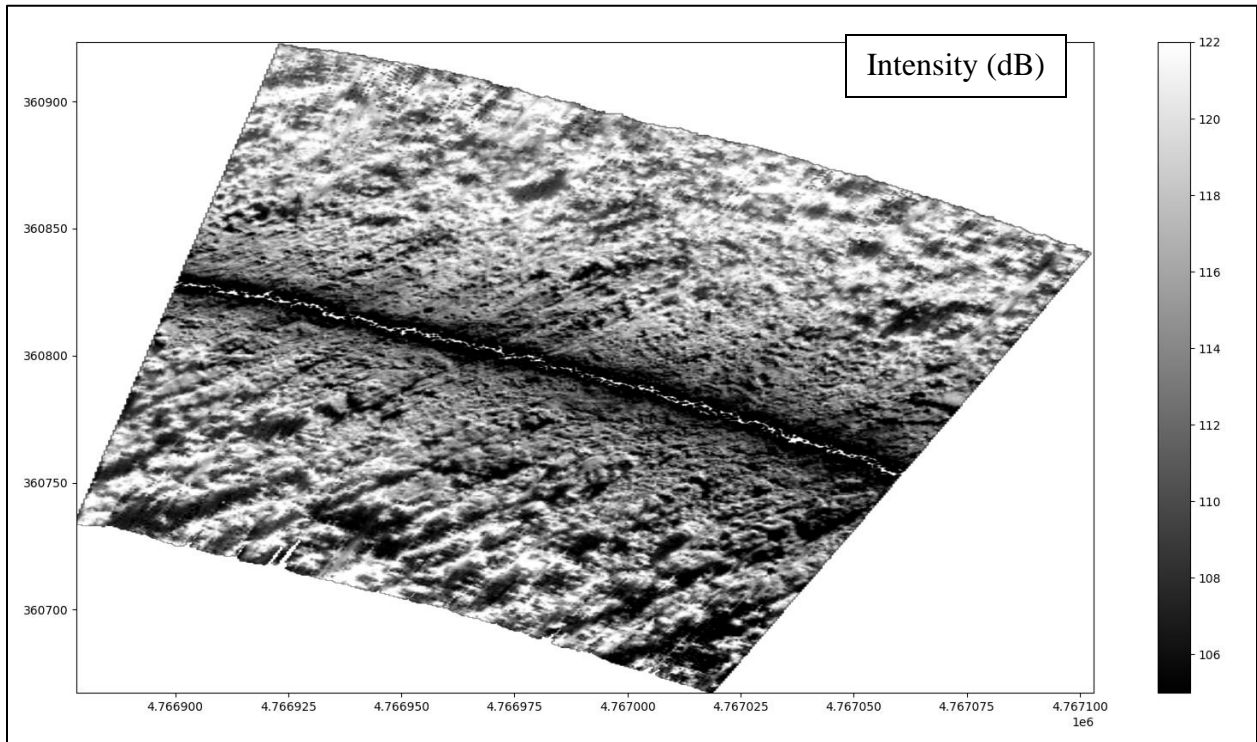


*Figure 36 – Backscatter image from a 6205 line, P.L. 3.7 ms., window average compensated for elevation and slope change across-track.*

## 2.10. Beamforming: an improvement?

Strategies to cope with sea surface multipath, when trying to resolve a single source, involve changing the transducer transmission and sensitivity to incidence angles over the horizontal, where reflections from the sea surface are expected to arrive. One technique that may meet this need is beamforming, which combines  $N$  transducers each with a given beam pattern into one, leading to a new beam pattern with more directivity. Clarifying, a beam pattern represents the transducer intensity response as function of the direction of a signal transmission or reception.

Using transmit beamforming, one could narrow the side scan sonar transmit beam, attenuating the outbound multipath. As a broad beam is desired in transmission, only a slight beamwidth reduction may be applied. This aspect was not heavily explored in this thesis, though a brief discussion is made further in this section. Alternately, beamforming can also be used during reception, potentially attenuating the inbound multipath, and increasing the receive gain at a given direction, so using it at the receive cycle may be an answer to provide more SNR near-nadir and in the far range. The receive beamforming is the focus of this study.

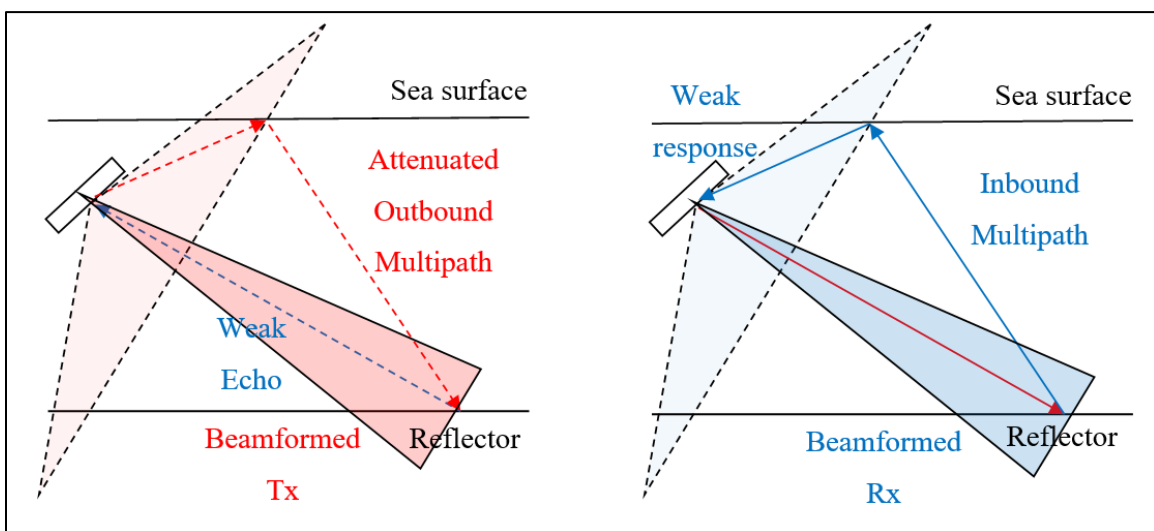


Figure 37 - Theoretical beamforming multipath suppression.

Such an approach, of course, is at the heart of multibeam receiver design. MBESs commonly use more than twenty wavelength-long receivers that ensure less than a two-degree beamwidth in elevation. In that way, the problem of multiple simultaneous echoes is reduced to within the receiver beamwidth. Moreover, they use the amplitude detection method if that situation does occur.

Bringing this concept to the present study, the EdgeTech 6205, although never described as a multibeam, does have a receiver that comprises ten rectangular parallel staves with a total spacing of 4.5 wavelengths. The manufacturer does describe beamforming as one of the advantages. This thesis thus will be investigating the feasibility of this, both by trying to understand how the system works and attempting to improve the PMBS detection, while analyzing actual results by comparison to conventional beamformed MBES. To calculate the dimensions and sidelobe characteristics of beams that could be formed with the 6205 receivers, a review of the beamforming method is thus provided.

### 2.10.1. Beamforming (unsteered)

In the across-track plane, each staff may be considered a continuous line source with length  $\underline{L}$ , whose beam pattern is theoretically known as (Kinsler et al., 2000):

$$b_{1L}(\theta) = \left( \frac{\sin v}{v} \right)^2 \quad (2.35)$$

Where:

$$v = \frac{1}{2} k L \sin \theta$$

The beam pattern of  $N$  combined identical linear staves spaced of a distance  $d$  can be derived in the far field by the Product Theorem. The exact solution for that is the multiplication of Equation 2.35 by the beam pattern of a line array, given by:

$$b_N(\theta) = \left[ \frac{1 \sin\left(N \frac{kd}{2} \sin\theta\right)}{N \sin\left(\frac{kd}{2} \sin\theta\right)} \right]^2 \quad (2.36)$$

Thus, the exact solution is as follows:

$$b(\theta) = \left[ \frac{1 \sin\left(N \frac{kd}{2} \sin\theta\right)}{N \sin\left(\frac{kd}{2} \sin\theta\right)} \right]^2 \times \left[ \frac{\sin\left(\frac{1}{2} kL \sin\theta\right)}{\frac{1}{2} kL \sin\theta} \right]^2 \quad (2.37)$$

Considering  $d$  negligible when compared to  $L$ , Equation 2.37 is simplified back into Equation 2.36. This approach was chosen because the exact stave dimensions are not documented in the EdgeTech 6205 manual. The manual also describes that the distance between stave centers is approximately half wavelength, and the central frequency is 520 kHz. Thus, considering the distance between the stave edges  $d$  approximately zero and an estimated sound speed, each stave would measure about 1.4 mm in the across-track plane.

Then, the beam patterns of one stave and nine combined staves can be plotted on a logarithmic scale, as in Figure 38. The half-power beamwidth (-3dB level) is annotated in red:

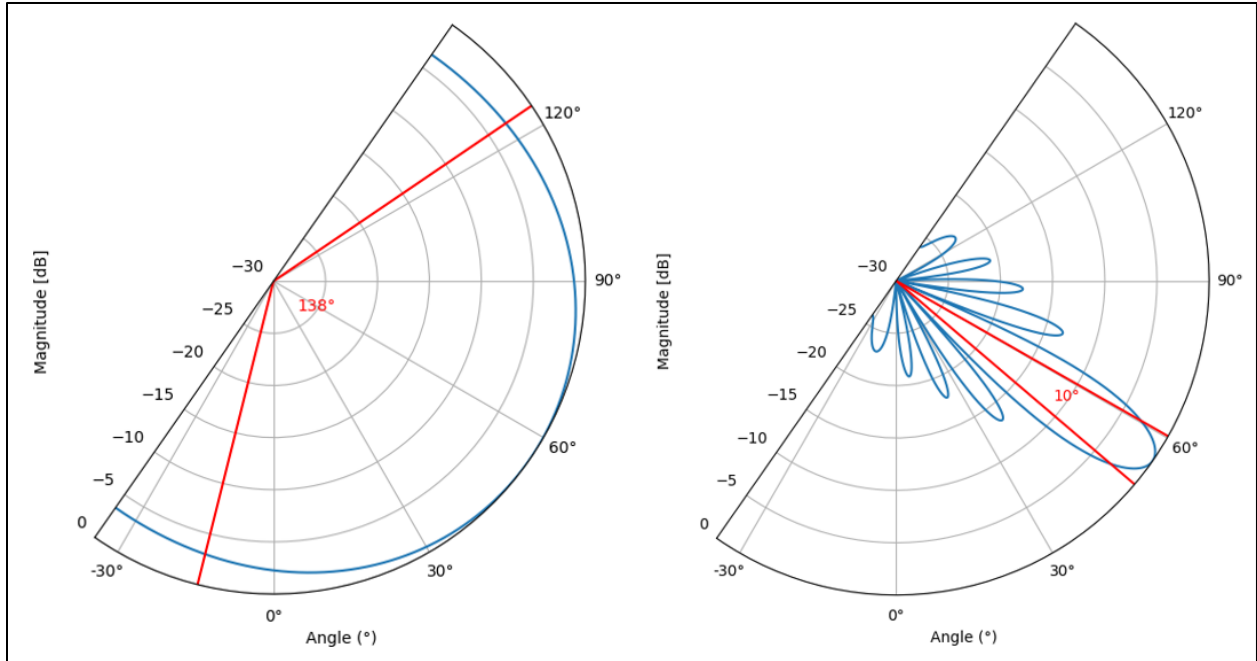


Figure 38 – Estimated beam pattern of one EdgeTech 6205 stave (left) and ten staves (right). Half-Power beamwidth in red.

As seen above, the combination of ten staves concentrates energy in the direction facing the array, reducing the beamwidth at -3dB from 138° to 10°. However, sidelobes are now present, the first at about 15° of boresight with a sidelobe suppression of -13.3 dB (as standard for unshaded line arrays – further explained in the next section).

### 2.10.2. Steering a beam

The beam patterns above would only help at the broadside. For example, for a 6205 with a mounting angle of 35° w.r.t. the vertical axis, this would improve data within a narrow range of elevations in the mid-range. Clearly, to be advantageous, we need to be able to steer this inboard and out. Suppose the stave individual contributions are not summed coherently but are time-delayed; in other words, steering is attempted. In that case, the energy coming from a given direction will be amplified, while the amount coming from other directions will be attenuated,

given that an odd number of transducers  $N = 2k + 1$  is being summed. This process is called electronic beam steering, making it possible to scan energy spatially without physically rotating the array.

According to Lurton (2008), beamforming for narrowband signals can be calculated using phase shifts, calculated from the stave spacing. In turn, Van Trees (2002) describes narrowband signals as those in which the product of the bandwidth and the maximum travel time across the array is much less than one. For the 6205, where 50 kHz of bandwidth is used and the total array measures about 14mm, this product is 0.47. A less strict definition, described by Abraham (2019), considers a signal narrowband if the ratio between the bandwidth and the central frequency is much less than 1, thus not considering the array size. For the 6205, this ratio is 0.096. Considering both metrics, the system was considered narrowband in this study, and the phase-shift beamforming model, given by Equation 2.38 below, was considered applicable to this system:

$$s(\theta_0, t) = \sum_{n=-k}^{+k} w_n s_n(t) \exp\left(-2j\pi n \frac{d}{\lambda} \sin\theta_0\right) \quad (2.38)$$

Where:

- $\underline{W}_n$  is an array of amplitude weights to reduce sidelobe influence.
- $\underline{S}_n(t)$  is the complex observable from each stave  $\underline{k}$ .
- $\underline{d}$  is the stave spacing (estimated to be half-wavelength).
- $\underline{\lambda}$  is the wavelength at the instant t. Accurate results must account for the transducer face's sound speed variation.

Equation 2.38 belongs to a class of array processing techniques named “Conventional Beamforming.” These techniques require the expected DOA as input, delivering the maximum power incoming from that direction. They are commonly used techniques in real-time applications because of their computational efficiency and satisfactory results. The initial description above treated the signal of all receiver elements equally (unshaded). In contrast, a weighting factor can be introduced to reduce the sidelobe contributions. This attenuation process is called array shading (Harris, 1978) and is achieved by applying decreasing weights from the center stave to the edges of the array.

The main drawbacks of shading the array are an overall power loss, as contributions of staves are progressively reduced, and a directivity loss because attenuating the extremities make the array behaves as a smaller transducer. Given the clear need for balance, different weighting kernels were studied for best sidelobe attenuation while maintaining power and directivity. One of the most used is the Dolph-Chebyshev kernel, which achieves a minimum beamwidth while fixing the sidelobe level at a specified value (Stegen, 1953). The set of Chebyshev weights is calculated for ideal arrays, and they can be obtained by knowing the number of staves and the intended sidelobe reduction in decibels. The Chebyshev weighting kernel can be found in Alexopoulos (2005), and is usually included in signal processing packages, such as Python’s `scipy.chebwin`.

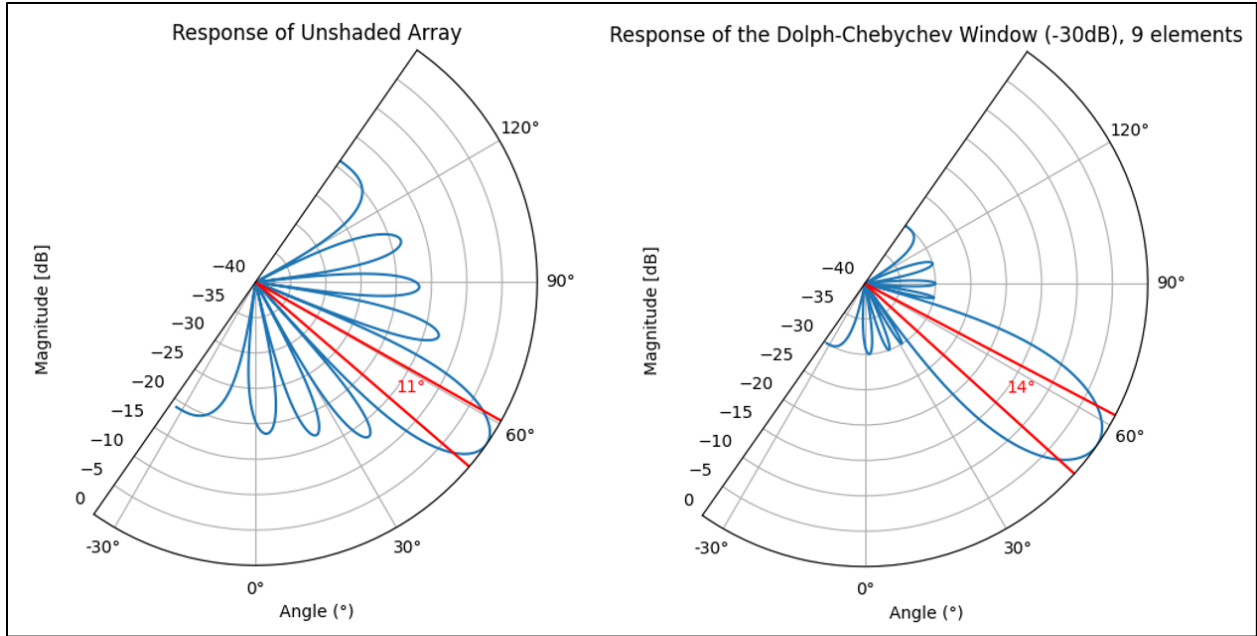


Figure 39 – Unshaded response vs. Dolph Chebyshev response for nine elements, 0° steering, and SLL=-30dB. Half-Power Beamwidth in red.

With respect to the directivity loss, Stegen (1953) defined an expression to approximate the half-power beamwidth (HPBW) of a Chebyshev-shaded array, given by:

$$\theta_{HP} = \frac{A}{L\lambda} \quad (2.39)$$

Where:

- $\underline{A}$  is a constant depending on the desired attenuation level.
- $\underline{L}$  is the array length.

The ratios obtained by Equation 2.39 can be seen in Table 2:



*Table 2 - Half-Power Beamwidths for a 9-element Chebyshev-shaded array.*

<b>Kernel</b>	<b>A</b>	<b>HPBW (°)</b>	<b>Ratio Shaded/Unshaded</b>
Unshaded	-	11.9179	-
Chebyshev -20dB	51.1	11.9953	1.0065
Chebyshev -30dB	60.6	14.2253	1.1936
Chebyshev -40dB	68.7	16.1268	1.3531

Regarding the possible attenuation values, while theoretically possible, a -40dB sidelobe suppression is never physically realizable as array elements are never perfectly identical and aligned. Thus, -30 dB attenuation is the usual choice for sidelobe suppression.

Another use of shading is controlling the beamwidth, to avoid transmitting energy to the sea surface and incurring in the outbound multipath (see section 2.8.6). For example, during the transmission cycle, according to Grall et al. (2020), the 6205 has an across-track beamwidth of 100°, which is a thinner beam than the 138° provided by the 1-element main lobe. This reduced beamwidth could have been achieved by using a larger transducer for transmission only. Another possible realization can be achieved using shading: the system needs a wide beam, though investing energy in the other side of the swath or the water column would only reinforce ambiguity and outbound multipath. Thus, the central element may receive complement power from the two adjacent staves, but just a fraction, not enough to form sidelobes in the transmission pattern. In this context, it is important to mention that there is no statement in the use of shading within the EdgeTech documentation available.

A hypothesis of how the transmit beam was formed to 100° is summing about 10% of power from adjacent elements, for example, using a transmit weighting kernel of [0.1007, 1, 0.1007]. This configuration would yield the beam pattern shown in Figure 40. Slight steering could still be applied by delaying the transmission pulses to place the HPBW optimally, but this was not considered in the beam pattern below.

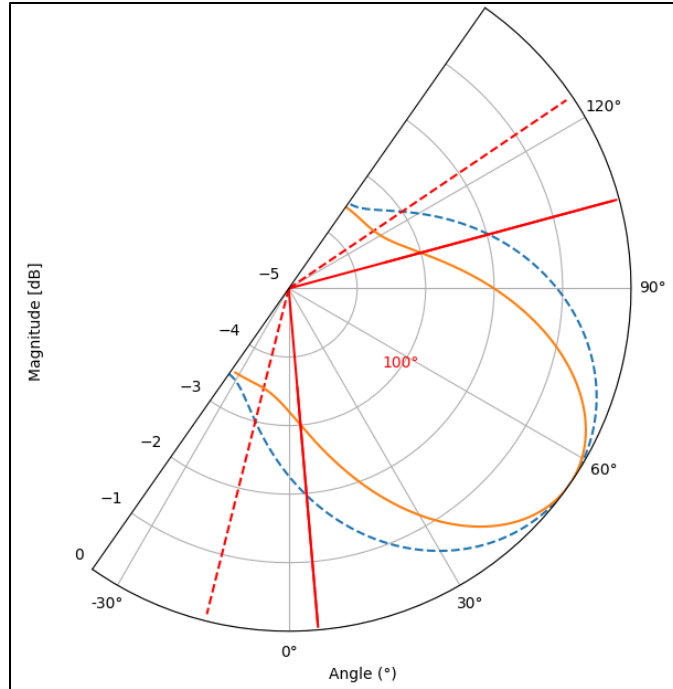


Figure 40 - Hypothetical transmit beam pattern, achieved with a 3-element beamforming, shaded by the kernel  $[0.1007, 1, 0.1007]$ . Dashed line: Single-element beam pattern.

Additionally, the beam steering effectively changes the array beam pattern. An array with length  $\underline{L}$  steered by  $\underline{\theta}_0$  behaves approximately equal to a virtual array of length  $L_0 = L \cos \theta_0$  for angles close to the steering direction. The beam pattern of a steered line array is also given by Equation 2.36, though using the following argument  $v$ :

$$v = \frac{1}{2} k L \cos \theta_0 \sin(\theta - \theta_0) \quad (2.40)$$

As such, the more steered the angles, the more the beamwidth increases. For example, the EdgeTech 6205 has ten staves and a mounting angle of  $35^\circ$  down w.r.t. the vertical. Discarding the first or the last stave, one could steer a 9-stave combination down by  $55^\circ$ , yielding the following unshaded beam pattern:

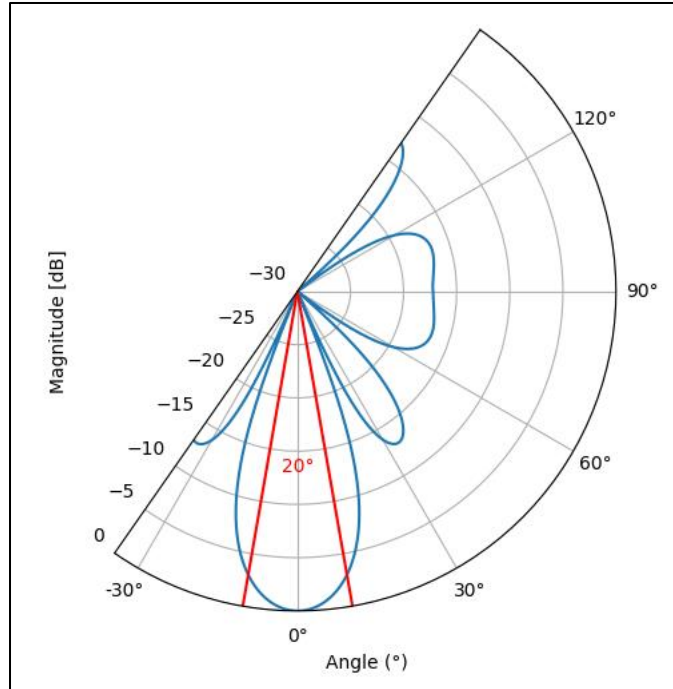


Figure 41 - Steering down 55° an EdgeTech 6205 9-stave split-array.

Furthermore, if shading was applied to the array, the ratio shown in Table 2 could be applied to estimate the beam patterns, resulting in the following beamwidths per steering angle:

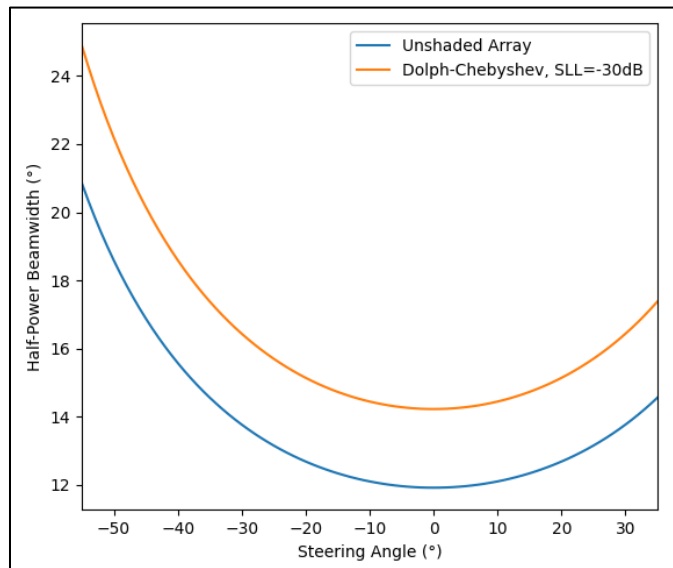


Figure 42 – Estimated Main Lobe Half-Power Beamwidth per Steering Angle for the EdgeTech 6205. A -55° steering faces the array to the nadir, while a +35° steering faces the array to the horizontal plane.

Another point beamforming helps detection is increasing the directivity. By making the sensitivity beams thinner, the transducer also directionally rejects noise, decreasing the noise level component of the SNR by the amount of directivity. The directivity is calculated by the ratio between the spherical volume and the HPBW solid angle, approximated by Equation 2.41:

$$DI = 10 \log_{10} \frac{4\pi}{\Theta_x \Theta_y} \quad (2.41)$$

For the 6205 case, the receive directivity for one element ( $1^\circ \times 138^\circ$  HPBW) is 24.7 dB, while a 9-element beamformed array at far-range ( $85^\circ$  incidence,  $1^\circ \times 16.3^\circ$  HPBW) provides a directivity of 34.0 dB, yielding a 9.3 dB SNR amplification.

In conclusion, for the beam pattern of one stave (Figure 38, left), one can observe that near the nadir, the intensity response does not vary so much, so signals from symmetric directions w.r.t. nadir may have similar amplitudes, thus interfering considerably. Through beamforming (Figure 38, right), the receiver sensitivity can be focused and steered down to attenuate ambiguous sources. For the far range, the beamforming may help attenuate the surface multipath, expected to arrive from over the horizontal, away from the MRA.

More than one virtual array is necessary to calculate phase differences, so combining all ten of the 6205 staves is pointless, as there is nothing to compare with. Consequently, the longest arrays that can be combined are two, composed of nine staves and separated by half wavelength (Figure 43):

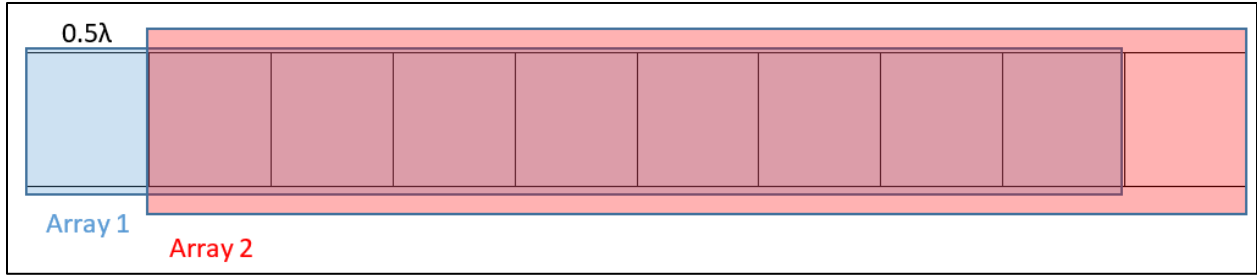


Figure 43 - 9-stave split array.

This configuration would yield the narrowest possible beams and an unambiguous phase difference solution. By reducing the number of staves in each split array, the main lobe would be slightly widened, but now more arrays spaced by half wavelength could be created. Figure 44 presents a 7-stave split array, which shows stave spacings of  $0.5\lambda$  (arrays 1&2, 3&4),  $1.0\lambda$  (arrays 1&3, 2&4), and  $1.5\lambda$  (1&4).

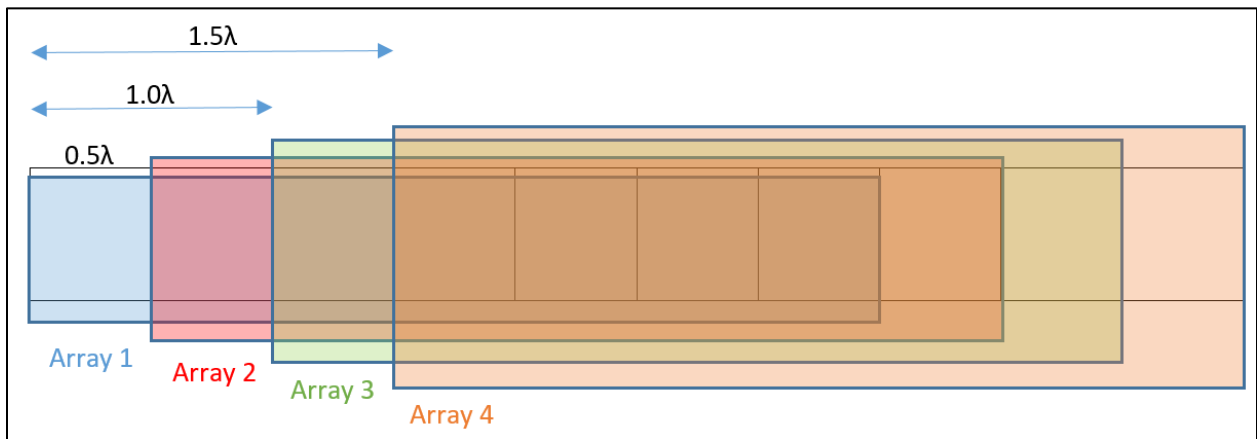


Figure 44 - 7-stave split array.

Two other split arrays can be formed by reducing a pair of combined staves, making possible two more half-wavelength spacings. Unambiguous solutions are already possible just by using the half-lambda pairs differential phase average, but these solutions are noisy, as seen before. By creating virtual arrays with longer baselines, ambiguous, though more precise solutions can be derived and combined with the unambiguous solutions to achieve a refinement by averaging

equidistant pairs or another array processing method. However, more computational power would be required, as beamforming would be made for each virtual array. Besides, as fewer arrays are combined, the beamformed main lobe is wider, reducing the multipath suppression power. Therefore, there is a compromise between the variance reduction by averaging more stave pairs and the directivity achieved by combining more staves, thus having fewer virtual elements. ZHOU et al. (2005) recommends using small subarrays to enlarge the length of the phase difference curve to reduce the function fitting error, as explained in section 2.7.3. They also mention that the use of beamformed ambiguous pairs would need a phase unwrapping before estimating the phase slope. In contrast, by using half-wavelength pairs only, the solutions will not benefit the more accurate pairs, though each can be obtained directly. Bearing in mind these benefits and detriments, as this study chose to use complex averages instead of regressions to perform the time average, 9-element beamforming solutions would be less affected by the phase curve nonlinearities.

### 2.10.3. Adaptive beamforming

Conventional beamforming is often the most suitable array processing method for real-time applications because of its efficiency. Nevertheless, other beamforming methods, known as adaptive beamforming or high-resolution methods, exist. While conventional beamforming needs a pre-defined weighting kernel and the expected direction of arrival, adaptive beamforming makes use of the data itself to estimate optimal weights and the direction of arrival from where a given constraint is achieved, such as best SNR, minimal variance, among others, or even suppressing a direction from where noise is expected, such as the surface reflection (Blomberg et al., 2013). Many of these methods can detect multiple sources simultaneously.

Reasons for the improvement include weighting kernels being designed to ideal arrays and not considering imperfections that may happen in the manufacturing process. Also, beam patterns are influenced by the propagating mean, so the theoretical performance of ideal weights or steering will usually be reduced. Although adaptive beamforming is very promising, it greatly affects efficiency. For instance, the MUSIC (Multiple Signal Classification) algorithm computes a pseudo-spectrum of the signal coming from every direction, as specified by an input search grid, as implemented by Wang (2018), based on Van Trees (2003).

The highest peaks will reflect the source locations, meaning another process is needed to estimate the number of sources. A way of earning efficiency is by imposing constraints to avoid searching the whole subspace and resolving a set of equations instead. This approach is used by parametric methods, among which one is known for superior performance in bathymetry: the Root-Music algorithm.

According to Van Trees (2003), the Root-Music algorithm receives the estimated sample covariance matrix as input, then computes its Eigen decomposition. The MUSIC spectrum is, then, redefined under a polynomial form, valid for ULAs only, and it is evaluated on the unit circle, finding solutions that correspond to the original MUSIC spectrum peaks. The estimated covariance matrix, needed as input for the Root-Music algorithm (and many of the adaptive beamforming methods), is given by:

$$R = \frac{1}{K}XX^H \quad (2.42)$$

Where:

- $\underline{R}$  is the N-by-N array covariance matrix estimated for  $\underline{N}$  staves at the reception of a given signal.
- $\underline{K}$  is the number of sample snapshots (or time slices).

-  $\underline{\mathbf{X}}$  is an N-by-K complex sample matrix containing the sample time series of a given stave in each line.

-  $\underline{\mathbf{X}}^H$  is the Hermitian transpose, or conjugate transpose, of  $\underline{\mathbf{X}}$ .

A conclusion that can be taken from Equation 2.42 is that many snapshots (or time slices) are needed to derive one sample. In this case of study, each sample is expected to be received once by each stave, so it is deemed to compute a poor estimate for  $\underline{\mathbf{R}}$ . The solution is to use a time average, similarly to the explained in section 2.7.3. The consequence of this choice impacts the resolution achieved since a group of samples is being used to derive each DOA.



## CHAPTER 3: METHODOLOGY

### 3.1. The EdgeTech data format

The first step of this research was writing a Python reader to extract the sensor observables from the JSF format used by EdgeTech. The EdgeTech 6205 is operated using the manufacturer's controller software called Discover. Two main characteristics of the system made this research possible: the possibility of recording the staves' unprocessed observables in the acquisition software, presented by the manufacturer as a diagnosis tool (Figure 45), and a detailed and updated document describing the JSF file (EdgeTech, 2022).

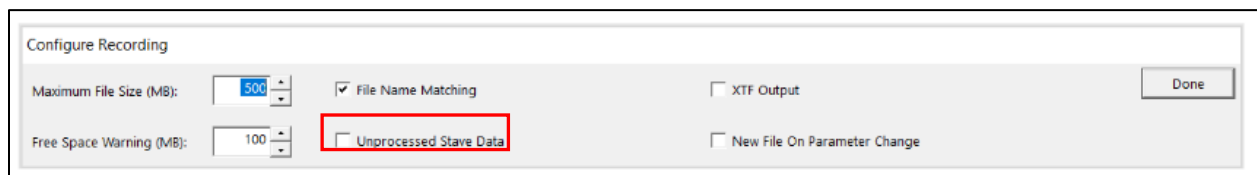


*Figure 45 - Discover Recording Settings*

If the unprocessed stave data option is chosen, the bathymetry and stave files will be recorded simultaneously. The bathymetry file is the final default product of the system in which a set of reduced (binned) DOAs are provided together with synchronous navigation data. The stave data file, in contrast, contains just the raw observables from which the DOAs are derived. Both are recorded in the same JSF format, the difference being which fields are recorded. Sample data from a different system (an AUV 2205 equivalent model) was used to write the JSF reader because, at this point, the data analyzed in this thesis had yet to be collected.

The JSF file is a binary file stored using the little-endian format, structured in sequences of standard messages. The message type, a field registered in the header of each message, identifies

what kind of information and structure is present in the following fields. The essential message types used in this study were:

*Table 3 - JSF Message Types and Core Information*

<b>Message Type</b>	<b>Message</b>	<b>Core information</b>
80	Sonar Data	Side scan sonar amplitudes (stave complexes or side scan compounded amplitudes)
3000	Bathymetric Data	Processed TWTT and DOAs, Altimeter (single beam) depth.
3001	AttitudeMessageType	Heading, Pitch, Roll, and Heave
3002	PressureMessageType	Probe sound velocity
3004	PositionMessageType	Latitude and Longitude

An aspect being highlighted is that the stave file does not bring all the information needed for the bathymetry processing, notably the probe sound speed information, required for the beam steering process, as mentioned in Section 2.10, so both the binned file and the stave file were used in this study's development.

The data is organized in the file per ping number, data format, and subsystem channel. The most important data formats are the real amplitude (value 0), used to record the compounded side scan image, and the complex amplitude (value 1), used to register sonar traces. As for the subsystem channels, even numbers are port channels (or the port compound, if the data format is 0), while odd numbers are starboard channels (or the starboard compound, if the data format is 0).

Table 4 lists how the sonar data was recorded in the JSF file:

*Table 4 - Sonar Trace Record Organization*

<b>Ping Number</b>	<b>Subsystem Channel</b>	<b>Data format</b>	<b>Sonar Trace</b>
10000	0	0	Port side scan amplitude (real)
10000	1	0	Starboard side scan amplitude (real)
10000	0	1	Stave 0 complex amplitude
10000	1	1	Stave 1 complex amplitude
10000	2	1	Stave 2 complex amplitude
	(...)		
10000	19	1	Stave 19 complex amplitude
	NEXT PING		
10001	0	0	Port side scan amplitude (real)
	(...)		

The main difference between bathymetry and stave files is that the first contains all the additional bathymetry messages (3000 series) and message 80's sonar traces, then includes side scan imagery. As for the stave files, their message 80 also includes the stave complex sonar traces, but no bathymetry message is included. Comparing the physical memory needed to store both, stave files were about ten times larger than bathymetry files. The channel numeration sequence in Table 4 matches the physical arrays, as shown in Figure 46. This information needs to be considered when planning the split arrays and when computing phase differences because, as the model was conceived, the lower channel should be multiplied by the conjugate of the upper; otherwise, the mounting angle will be changed to the supplement of itself.

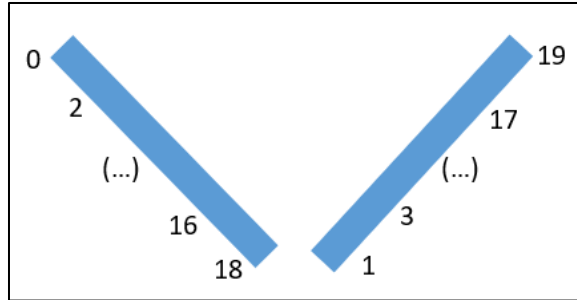


Figure 46 - EdgeTech Subsystem Channels

As described by the manufacturer, any TVG used in real-time is not applied to the recorded amplitudes of message 80. A standard 50 dB/100m TVG (changeable in advanced options) is applied during the bathymetry processing, which impacts the bathymetry values only.

The TVG is especially important for backscatter, where the amplitude statistics may be used to infer characteristics of the seafloor, such as bottom sediment classification. For bathymetry, though, this value can be roughly estimated. To verify if the TVG applied is reasonable, a simulation was made to compare the theoretical TVG from Equation 2.34 to the levels adopted by EdgeTech (Figure 47).

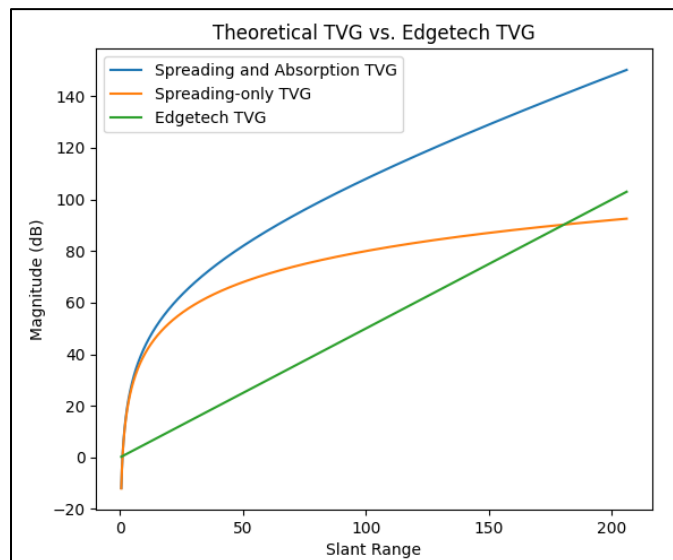


Figure 47 - Theoretical TVG vs. EdgeTech TVG.

Figure 47 was obtained using an estimated absorption coefficient for ocean water at 5°C, salinity of 35 ppt, and pH of 8, at depths ranging within the system nominal specifications (0 to 50 m), at the 6205 nominal center frequency (520 kHz). The National Physical Laboratory (NPL) seawater absorption calculator, available at <http://resource.npl.co.uk/acoustics/techguides/seaabsorption/>, was used to estimate the value of alpha, found to be around 0.140 dB/m for the three models available (Fisher and Simmons 1977, François and Garrison 1982 and Ainslie and McColm 1998). The maximum slant range in the plot was obtained for a 50-meter depth and 200-meter horizontal range, the latter being the maximum available for the 6205.

Comparing the three TVG curves, a 50 dB/100m value is an underestimated compensation for the spherical spreading only, as seen in Figure 47. The full-TVG and the spreading-only TVG curve grow far from the EdgeTech TVG from 0 to 10-meter slant range, reaching about a 50 dB difference. Then, while the full-TVG maintains that offset, the spreading TVG converges to the EdgeTech TVG, resembling the last at about 180-meter slant range. It remains unclear if applying the model from Equation 2.34 would improve the system detection somehow.

## **3.2.The data collection**

### **3.2.1. The systems used**

The echo sounders used in this study were the PMBS EdgeTech 6205 and the MBES Kongsberg EM2040P. Both systems are designed to be compact, composed of a processing or deck unit, connected to a transducer and a sound speed probe under the water. To obtain high-quality, geo-referenced data, the controller units must also receive positioning, motion, associated offsets and alignments, and a synchronization signal from ancillary systems. In this survey, an Applanix POSMV 320 V5 inertial system was used to fill that need, providing a PPS sync and

integrated motion and position aided by an RTK base station owned by UNH. Finally, a dedicated P.C. is connected to the controller unit to provide a human-machine interface. A general scheme for both systems is presented in Figure 48 below:

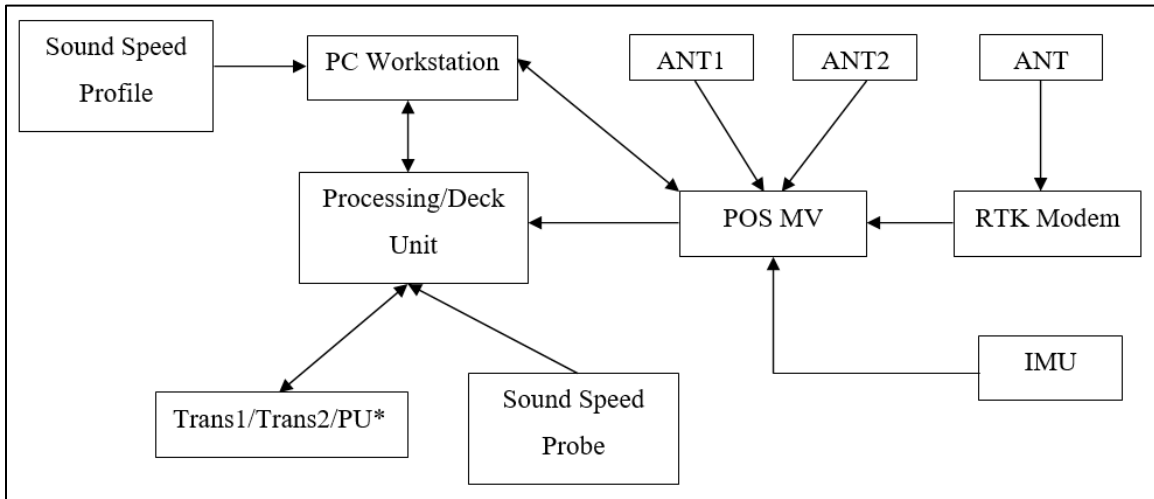


Figure 48 - General scheme for the swath systems used.



Figure 49 - EM2040P main components. Left: Tx/Rx transducers. Right: Processing Unit. Retrieved from Kongsberg.com.



Figure 50 - EdgeTech 6205 main components. Left: Sonar unit (dual transducers and sonar processing unit). Right: Rack mount deck unit (retrieved from EdgeTech.com).



Figure 51 - Applanix POSMV 320 V5 main components: Processing unit, dual antennas, and Inertial Measurement Unit (IMU). Retrieved from Applanix.com.

For this survey, the EdgeTech 6205 was controlled by its manufacturer’s software, Discover version 42.0.1, and the survey was planned and executed using Hypack 2020. The EM2040P was controlled, planned, and executed using the manufacturer’s Seafloor Information System (SIS) version 5, which is fully integrated with the echo sounder controller software K-Controller. Table 5 and Table 6 lists the main specifications of the systems used in this study:

Table 5 - Echo sounder specs. Retrieved from the manufacturer's manuals, Kongsberg (2020) and EdgeTech (2020), and from Grall et al. (2020)

Parameter	EM2040P	EdgeTech 6205 (520kHz Bathy)
Central Frequency (kHz)	200 – 400	520
Beamwidths	1.3° x 1.3° at 300 kHz	1° x 100°
Operating Depth	Up to 450m at 400 kHz	Up to 50m
Max swath width	140° at 300 kHz	200°
Pulse Modulation	CW & FM	CW & FM
Max survey speed	Unspecified*	4-5 knots

\* Limited by the needed density and environmental noise.

Table 6 - Inertial System specs. Retrieved from the manufacturer's manual Applanix (2017).

Parameter	Applanix POSMV (after GAMS*)
Roll	0.03°
Pitch	0.03°
Heave	5cm or 5% of depth (whichever is greater) for periods of 20s or less
Heading	0.03° with 2 m antenna baseline
RTK positioning – Horizontal**	8mm + 1ppm x baseline length
RTK positioning – Vertical**	15 mm + 1ppm x baseline length
Velocity accuracy	0.05 m/s horizontal

\* GAMS stands for GNSS Azimuth Measurement Subsystem, an Applanix-designed field calibration process to improve heading accuracy. More details can be found in Applanix (2017).

\*\* Estimated for 1m IMU-GNSS antenna offset

### 3.2.2. Installation

The systems were installed in the UNH Research Vessel Gulf Surveyor, a 48-foot (14.63m) long catamaran with a beam of 5.35m and a maximum draft of 1.68m. The vessel was specially designed for hydrographic surveys, having two main structural mounts for echo sounders: a retractable central strut in the rear and a removable over-the-side pole on the port side. The central strut is more stable since it is more rigid, and it has the support of two stabilizers that mitigate vibration and bending.



Figure 52 - R/V Gulf Surveyor. Retrieved from ccom.unh.edu.



Given the objective of comparing the PMBS and the MBES systems, the transducers were installed in the same structure one at a time and used the same ancillary system installation. The lever arms between each sensor and the Ship Reference Frame (SRF) origin were found by measuring by tape the distances over each axis to the closest monument (points in the ship with known coordinates in the SRF). The transducers' angular offsets were obtained by in-field calibration (patch test), for the IMU rotation considered. The lever arms and angular offsets used are described in Table 7, Table 8, and Table 9 below:

*Table 7 - Sensor lever arms (meters).*

<b>Point</b>	<b>X(+forward)</b>	<b>Y(+starboard)</b>	<b>Z(+down)</b>
Origin	0	0	0
6205 Transducer	-1.466	+0.014	+2.288
EM2040P Transducer	-1.319	-0.024	+2.294
Applanix IMU	-1.548	+0.018	+1.939
Applanix Antenna 1	+3.320	-1.845	-4.319

*Table 8 - Sensor rotations (degrees).*

<b>System</b>	<b>Roll</b>	<b>Pitch</b>	<b>Yaw</b>
6205 Transducer (Port)	+0.205	-3.334	+0.342
6205 Transducer (Stbd)	-0.198	-3.268	-0.447
EM2040P Transducer	-0.19	-0.6	+0.1
Applanix IMU	0	-90	0

*Table 9 - Water line height (meters).*

<b>Day</b>	<b>System used</b>	<b>w.r.t. Origin</b>
10/25/2022	6205	+1.023
10/26/2022	EM2040P	+1.034

### 3.2.3. Survey area

The chosen survey area was seaward of the Odiorne Point State Park in Portsmouth, New Hampshire, where there is known existence of interleaved sand sheet, rocks, and bedforms of

varied sizes, suitable for testing resolution and target definition as a function of grazing angle, and a regionally sloped seafloor extending from 3 to 14-meter charted depth (MLLW). The idea was to occupy a depth range equivalent to typical shallow rivers, where the benefits of extra-wide angular sectors would be most beneficial.

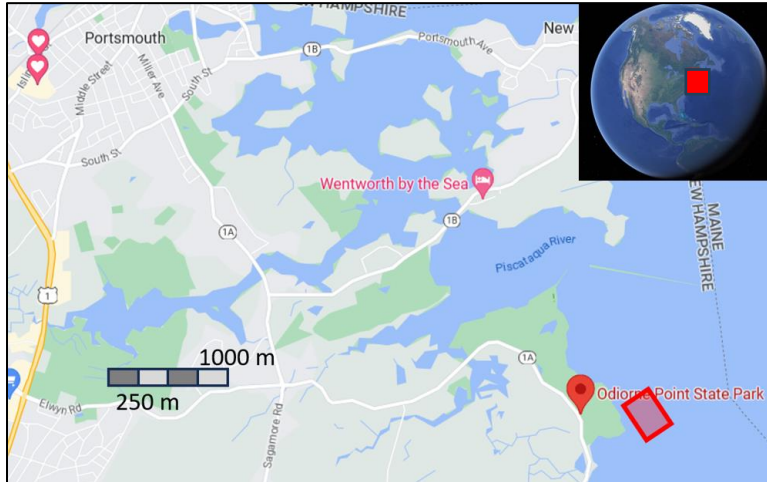


Figure 53 - Survey Location

Five survey lines, parallel to the coast and spaced by 50 m, were designed so that the survey would be made as shallow as possible to evaluate the performance of the PMBS in a challenging environment, where it is expected to provide the most advantages compared to traditional systems.

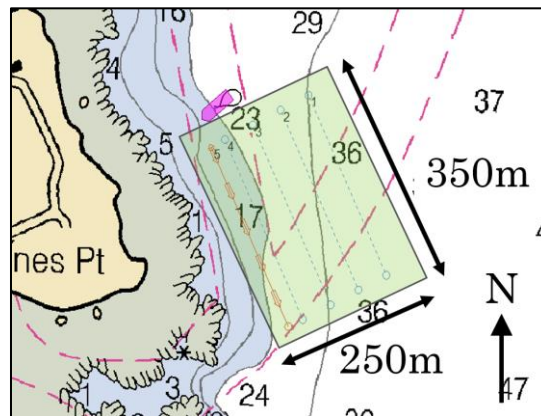


Figure 54 - Survey Line Plan. NOAA chart 13283 - depths in feet.

### 3.2.4. The PMBS survey

a) The data collected:

On 10/25/2022, an EdgeTech 6205 dataset was acquired, exploring as much as possible the most settings available in the system. The lines were numbered offshore to inshore from 1 to 5. The lines run and the configurations used are summarized in Table 10:

*Table 10 - Settings used during data collection.*

<b>Lines</b>	<b>Range (m)</b>	<b>P.L. (ms)</b>	<b>Bin Size (m)</b>	<b>Misc.</b>
1 to 5	100	0.25	0.25	-
1 to 5	100	0.50	0.25	-
1 to 5	100	1.00	0.25	-
1 to 5	100	2.10	0.25	-
1 to 5	100	3.70	0.25	-
1 to 4	50	0.25	0.10	-
5	200	3.70	0.50	-
5	50	3.70	0.10	-
5	100	3.70	0.25	TVG off
5	100	3.70	0.25	Multipath suppression 1
5	100	3.70	0.25	Across Track Average 0.24
4	200	3.70	0.50	Water column filter only.

After the survey, the data was processed using Qimera 2.3.5. Figure 55 illustrates a DTM made with processed data from the lines run with a 50-meter maximum range and pulse length 0.25 ms.

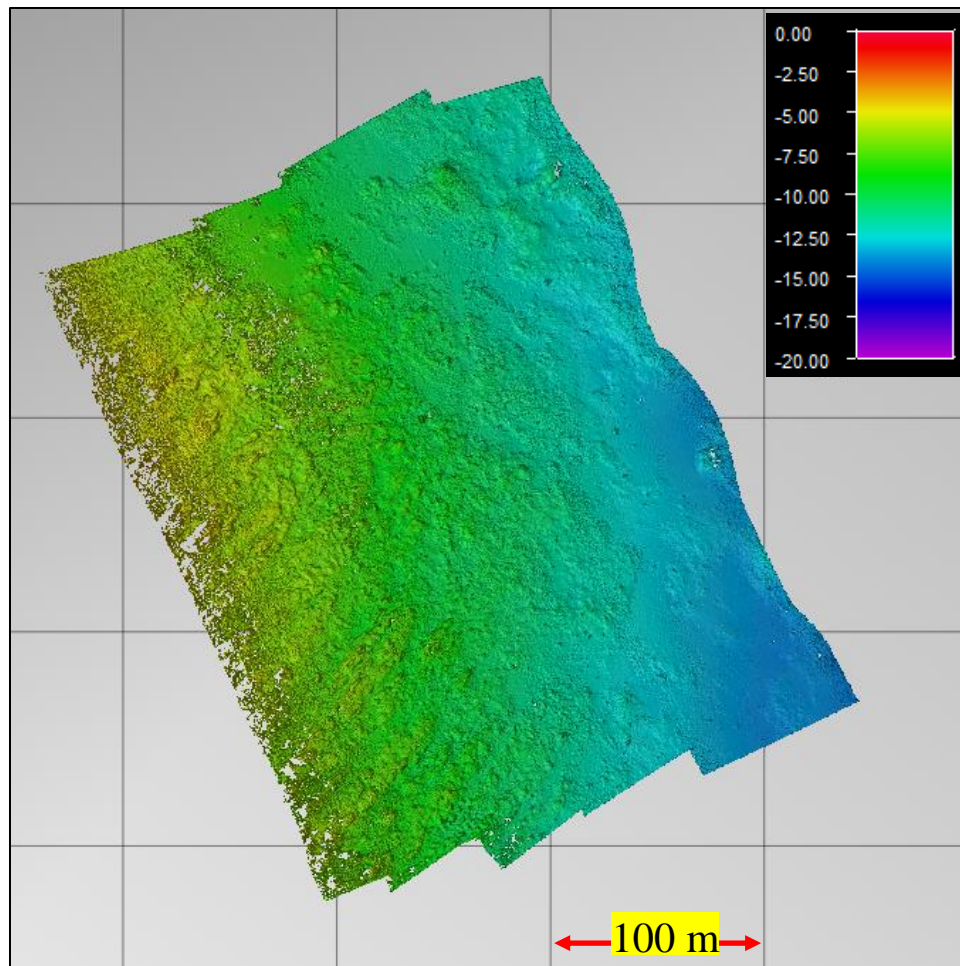


*Figure 55 - EdgeTech 6205 dataset - Max range 50m, PL 0.25ms.*

b) The operator settings:

Under the “Advanced Bathymetric Controls” section, the operator can change the maximum sonar range depending on the survey objective. Figure 56 shows the interface:

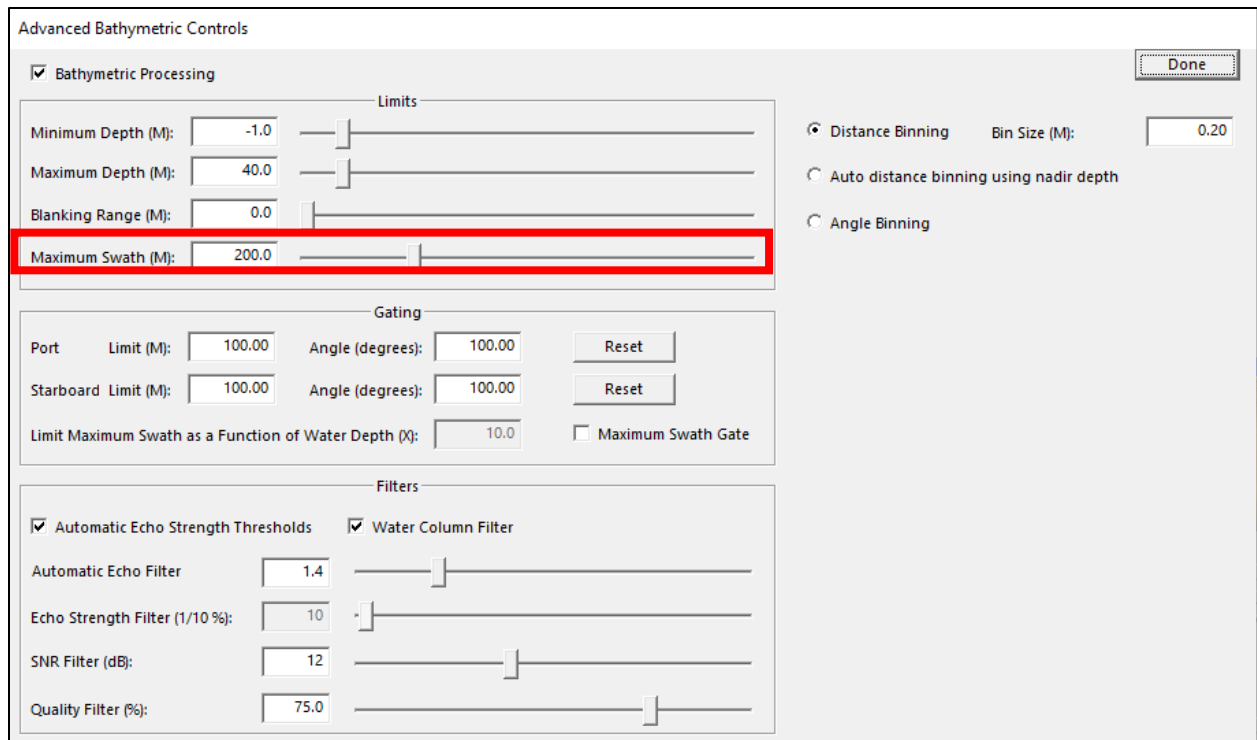


*Figure 56 - Discover advanced bathymetric controls.*

Among the options, the maximum range is of particular interest. It can be set up to 200 m, directly affecting the along-track density because the wider the range, the more time the transducer stays listening, making the system work with a lower ping rate. Secondly, filtering strength is also available, having a reasonable explanation in the system manual.

c) The sonar controls:

The transducer operation can be altered by changing the pulse length in the “Advanced sonar controls” tab between 0.25 ms, 0.5 ms, 1.0 ms, 2.1 ms, and 3.7 ms. The system default is to have the pulse length chosen automatically, but the operator can choose to override it and force the desired configuration.

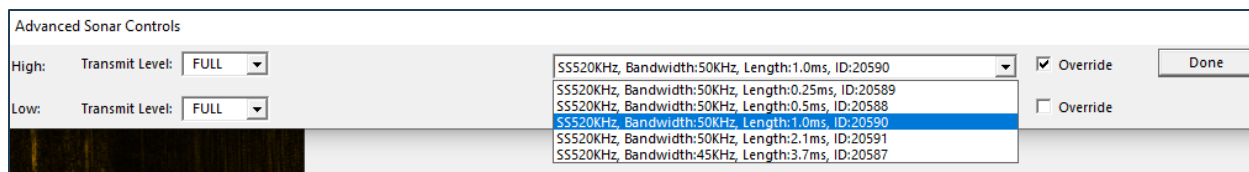


*Figure 57 - Discover advanced sonar controls.*

The system works with Frequency Modulated (FM) pulses as default, so the change of pulse length only affects the system’s maximum range. At the same time, bandwidth controls the resolution, which always lies at 50 kHz, except when the longest pulse is chosen (3.7 ms, 45 kHz). The transmit power cannot be changed, as it is FULL or NONE.

Longer pulses achieve greater ranges. Reasons for that include the fact that more energy is being transmitted in each cycle, and that there is an increase in the bottom backscatter strength, directly proportional to the ensonified area on the seabed. Additionally, the use of FM pulses also adds a compression gain to the SNR, dependent on the time-bandwidth product.

For the 6205, a 50-kHz bandwidth corresponds to a range resolution of 1.5 cm. If the system worked with Continuous Wave (CW) pulses, the needed pulse length to maintain that resolution would be 0.02 ms, more than ten times the lower pulse length available in the 6205 settings. Therefore, the system guarantees an SNR increment of at least 10 dB using FM pulses. Then, why not always choose the most prolonged pulses possible?

The main reason for that lies in the transducer duty cycle. Any transducer needs a cooldown before transmitting again to preserve the piezoelectric material lifetime. When the maximum range set is small, the system can fire faster, as the receiving time is reduced, but it still may be limited by the transducer duty cycle. That is the reason for having options for shorter FM pulses: when a small range is set, the system automatically chooses a pulse length that will not overload the transducer. For example, compare the ping rates performed by the 6205 at the 100-meter range and 50-meter range for the shortest and the longest pulse available:

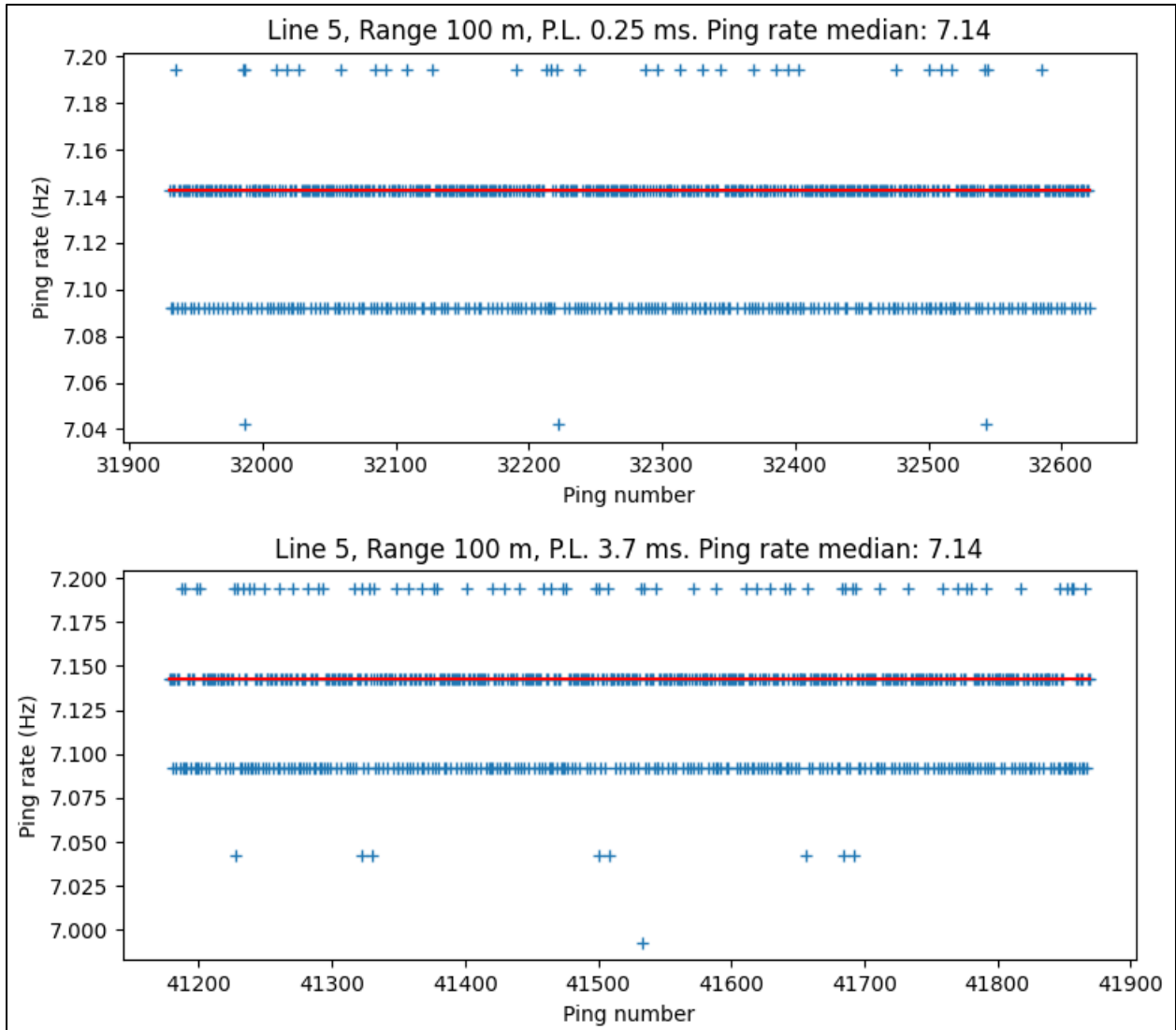


Figure 58 - Ping rate for 100m maximum range, about 8m depth, and pulse lengths of 0.25 ms (Top) and 3.7 ms (Bottom).

Figure 58 shows the ping rate obtained at Line 5, with a nadir depth of about eight meters, for a 100-meter maximum range. In this case, the receiving time for the maximum slant range provides enough cooldown so that the transducer can fire immediately after stopping listening, performing about 7.14 pings per second. Now, compare these with Figure 59:

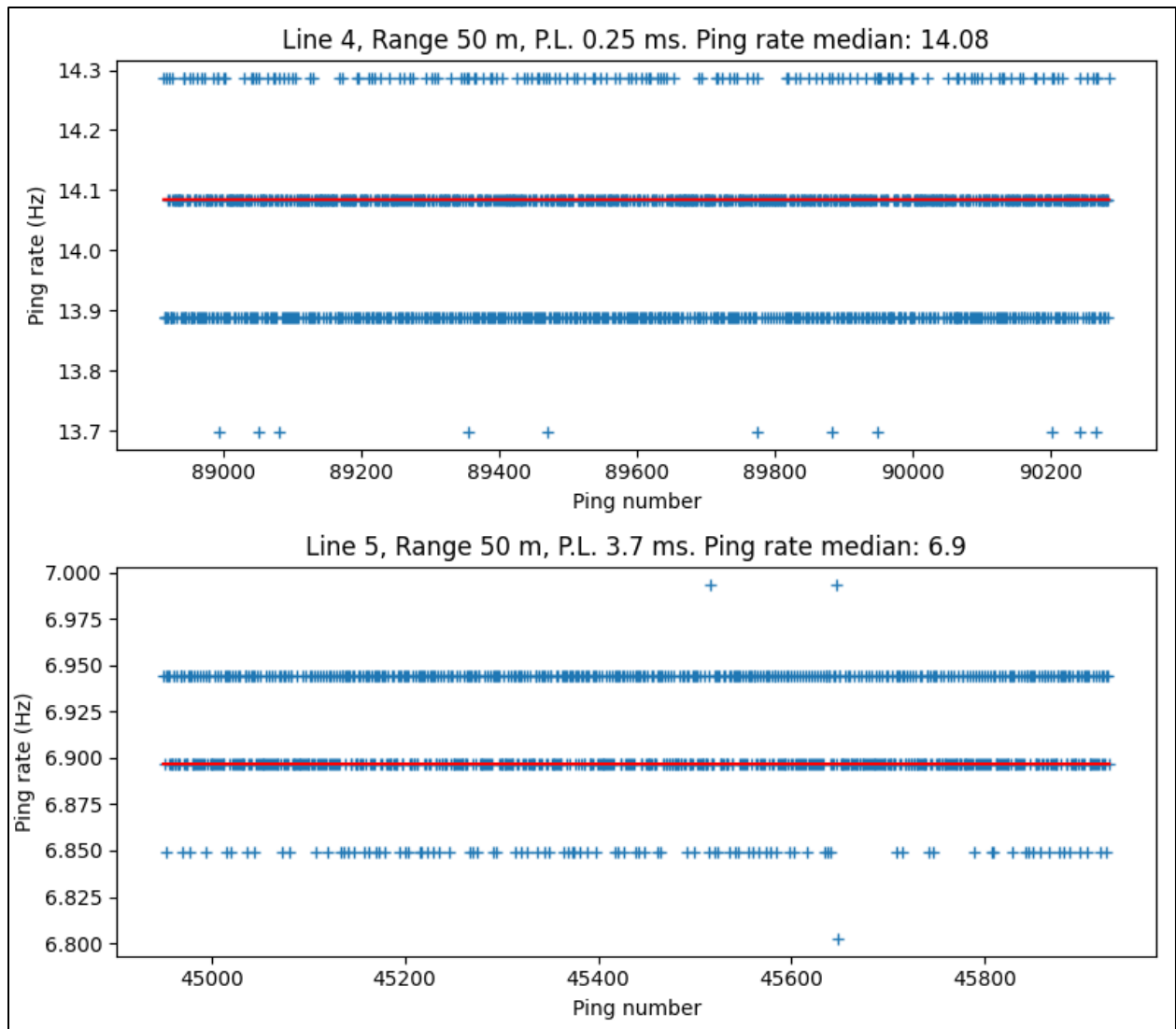


Figure 59 - Ping rate for 50m maximum range, about 8m depth, and pulse lengths of 0.25 ms (Top) and 3.7 ms (Bottom).

By reducing the maximum range, the system can fire about 14 pings per second if it were not for the duty cycle. Figure 59 clearly shows how using an unnecessarily long FM pulse may negatively affect the data collection. For a 50-meter range, the system detected the bottom satisfactorily with the shortest pulse length, achieving almost two times the ping rate achieved with the 3.7 ms pulse length. That said, letting the system choose the pulse length automatically seems beneficial, depending on the depth, SNR, and maximum range set.



d) The engineering controls:

The system also has engineering configurations, which are not expected to be changed by routine. Among them is the TVG used during the bathymetry processing, the multipath suppression level, and the maximum across-track average size. The default parameters are shown in Figure 60.

Bathymetric Processing Engineering Parameters

Warning: Changing these parameters will have significant effects on the data. These parameters should not be altered unless the user has a complete understanding of the consequences.

Done

Altitude Determination

Auto Detect Altitude

This feature should only be disabled under extreme circumstances. Such as when the bathymetric processor consistently fails to determine the altitude, or the seafloor is beyond the acoustic data.

Processing Refinements

Bottom Track Data Source: Product

TVG (dB / 100M): Default 50

Max TVG (dB): 60

Advanced Processing Refinements

Multipath Suppression Level: 3

Maximum Across Track Average Size (M): 0.10

Figure 60 - Discover bathymetric processing engineering parameters.

I – TVG:

EdgeTech (2022a) states that the TVG feature helps increase the bathymetric range in soft bottom conditions. Consider the Figure 61 below:

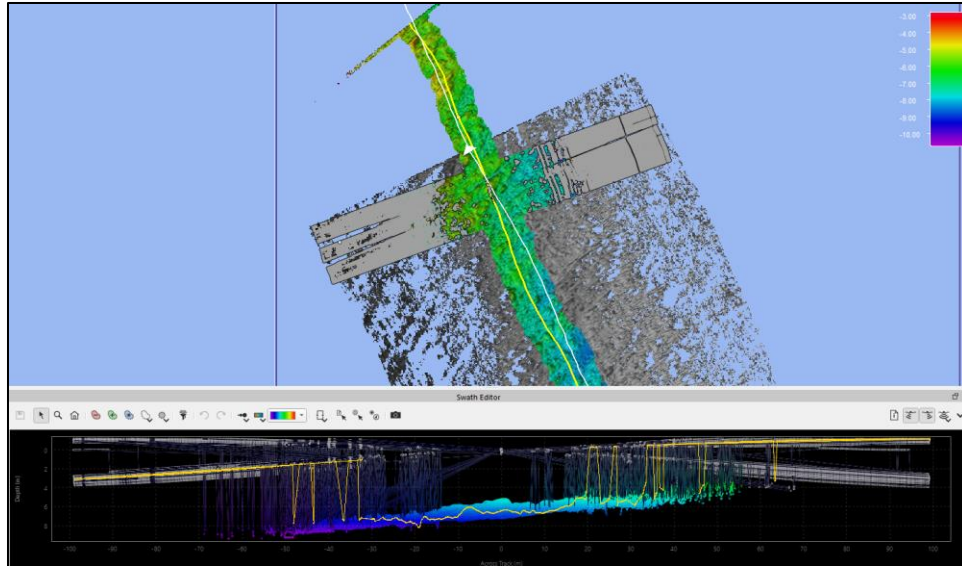


*Figure 61 - TVG off (rainbow) vs. Default TVG - 50 dB/100m (gray).*

Figure 61 compares a line run with the default TVG (50 dB/100m) and a second line run over the previous without TVG. After taking out the TVG, the effective swath length was reduced from 70 m to 25 m. However, in Qimera’s line editor tool, it was possible to observe that the coverage from 25m to 70m was not lost, but rejected instead, meaning that the absence of TVG didn’t hinder the bottom detection, but it made the intensity thresholds automatically reject mid-to-far range soundings. However, it is still being determined if this setting has additional effects on bottom detection.

## II – Maximum across-track average size:

EdgeTech (2022a) describes combining multiple adjacent time samples to improve SNR before phase estimation. This logic implies a windowing process like the one explained in section 2.7.3, is being used in the bottom processing. This setting limits the maximum across-track region size to be averaged so that the system can guarantee a defined minimum resolution.

### III – Multipath suppression level:

According to the Discover software manual, this setting controls how many elements will be combined through beamforming to provide multipath suppression. The operator can choose:

- 1 for no multipath suppression, meaning the phase estimation method is used on the ten half-wavelength staves without prior beamforming.
- 3 to combine three adjacent elements, resulting in eight virtual half-wavelength spaced elements. This option is the default.
- 5 to combine five adjacent elements, resulting in six virtual half-wavelength spaced elements.

From this setting, it is possible to estimate the beam pattern in use by the system, but still, the array processing method used to synthesize the virtual arrays and to perform the phase estimation is not public. This study explores the conventional phase beamforming method, but EdgeTech may use other array processing techniques.

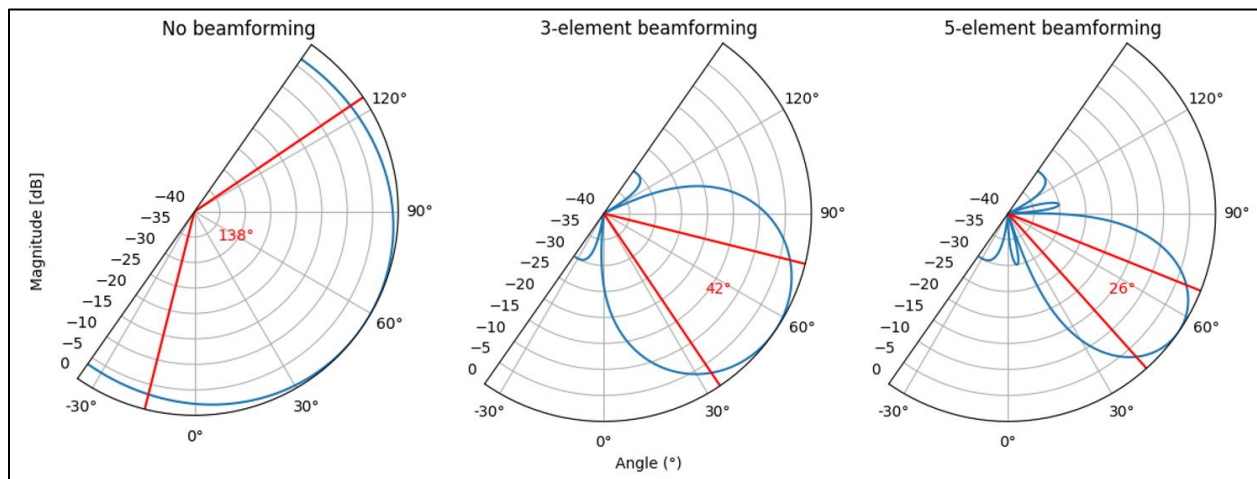


*Figure 62 - Expected beam patterns for the different multipath suppression levels (a -30dB Dolph Chebyshev shading was used).*

### 3.2.5. The MBES survey

On 10/26/2022 (1 day later), the Kongsberg EM2040P sonar was mobilized and used to survey the same area with 100% overlap. The MBES survey was conducted as closely as possible in time after the PMBS survey to minimize environmental changes on the seafloor (such as bedform migration). The system was operated at 300 kHz, in high-density mode, dynamic dual swath (along ship angle between fans dynamically changed to provide uniform along-track density), with a 140° swath coverage. Tighter spaced lines were used by the 2040P so that 100% overlap was achieved with a smaller swath coverage than the 6205's.

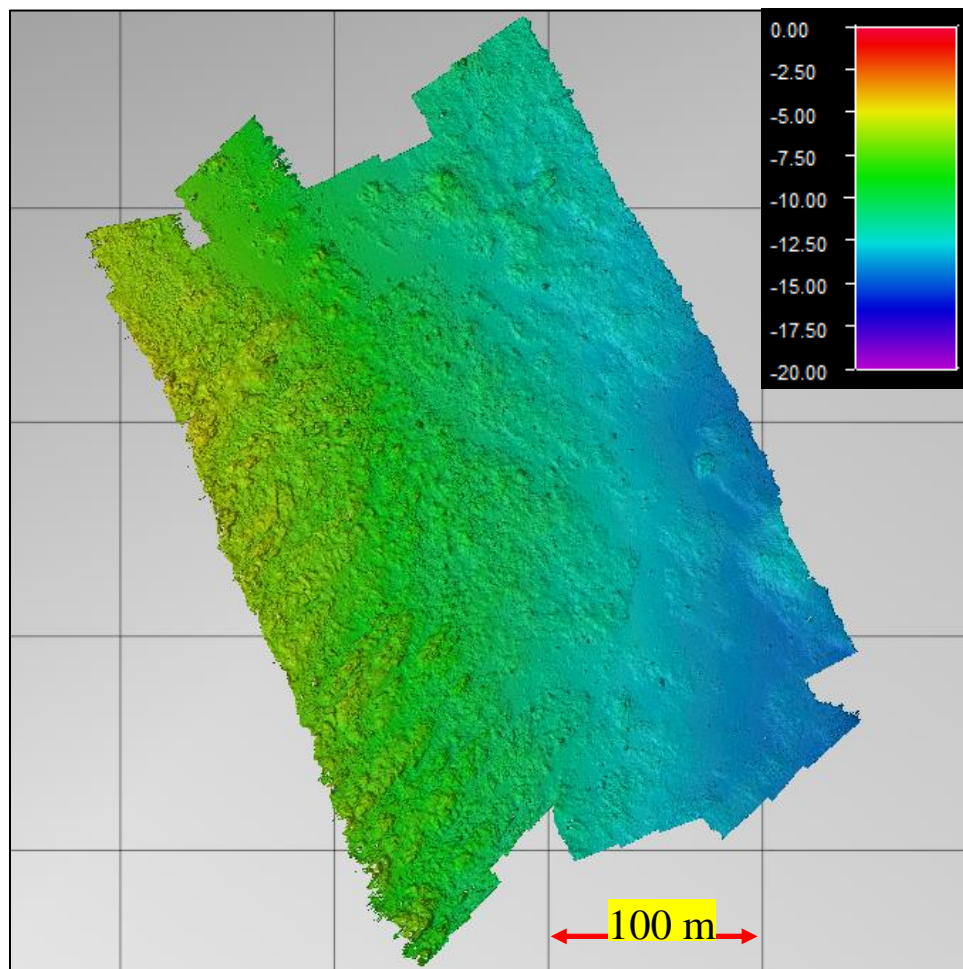


*Figure 63 - EM2040P dataset.*

The EM2040P dataset is intended to be used as a reference, so it must achieve well-recognized quality standards. A hydrographic survey quality assessment is usually made by comparing metrics with the standards defined by the country's hydrographic office. Still, the International Hydrographic Organization (IHO) also publishes its standards to serve as a common reference: the publication S-44, now in its 6<sup>th</sup> edition (IHO, 2022).

The S-44 standards categorize surveys in Orders, from the least stringent to the most: Orders 2, 1b/1a, Special Order, and Exclusive Order, being the Special Order the standard reference of quality for swath systems. The mean depth cross-check estimates the Total Vertical Uncertainty (TVU), one of the criteria to define the S-44 survey order and is implemented in most bathymetry post-processing software. The method is detailed in section 3.7.5.

Using Qimera's cross-check tool, the EM2040P reference dataset was compared to two EM2040P raw check lines. Rough surfaces tend to penalize vertical accuracy statistics, as the slightest horizontal positioning error may misalign sloped areas, such as the edges of rocks and boulders. Even so, the dataset still reached S-44 Special Order, proving itself as a reasonable reference.

The inshore side of the EdgeTech survey could not be entirely reproduced because the EM2040P swath was narrower, and the ship could not navigate closer to shore due to safety reasons, even surveying during high tide. Conversely, the 6205 surplus area in the west side is due to a broader operational swath width range when compared to the MBES.

### **3.3. Why include beamforming in the bottom detection? And how?**

The intent of adding beamforming to the bottom detection algorithm was to focus the array sensitivity on directions where detections were expected to occur in the reception cycle, hopefully

attenuating recurring multipath from sources other than ones contained in the beamformed main lobe and thus reducing interference.

The starting point for the concept development was combining the transducer staves as described in section 2.10. Combining  $N$  elements (3, 5, 7, or 9) and creating  $(11 - N)$  virtual beamformed arrays, with centers spaced by half-wavelength, the DOAs could be directly derived from the average phase difference between a two-by-two combination of virtual arrays. However, if no steering is applied following the time progression, correct solutions would be derived only for the main lobe, on the mid-range.

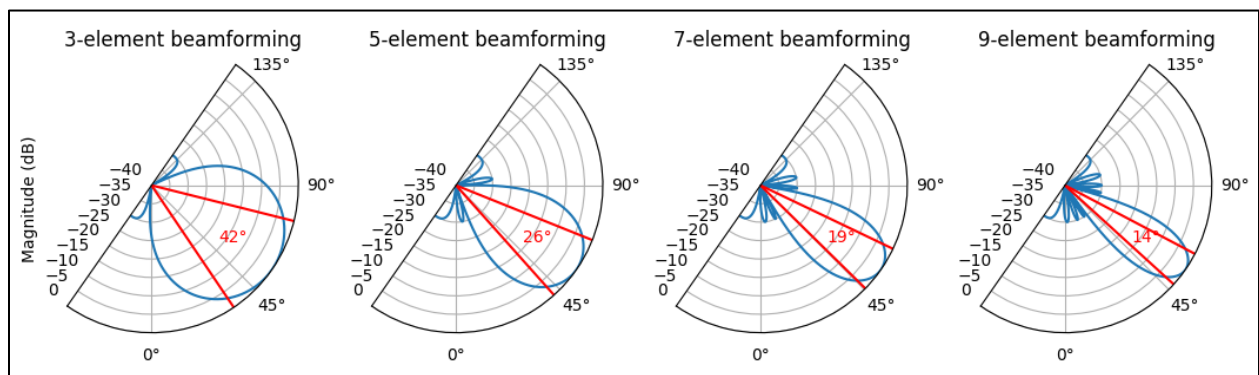
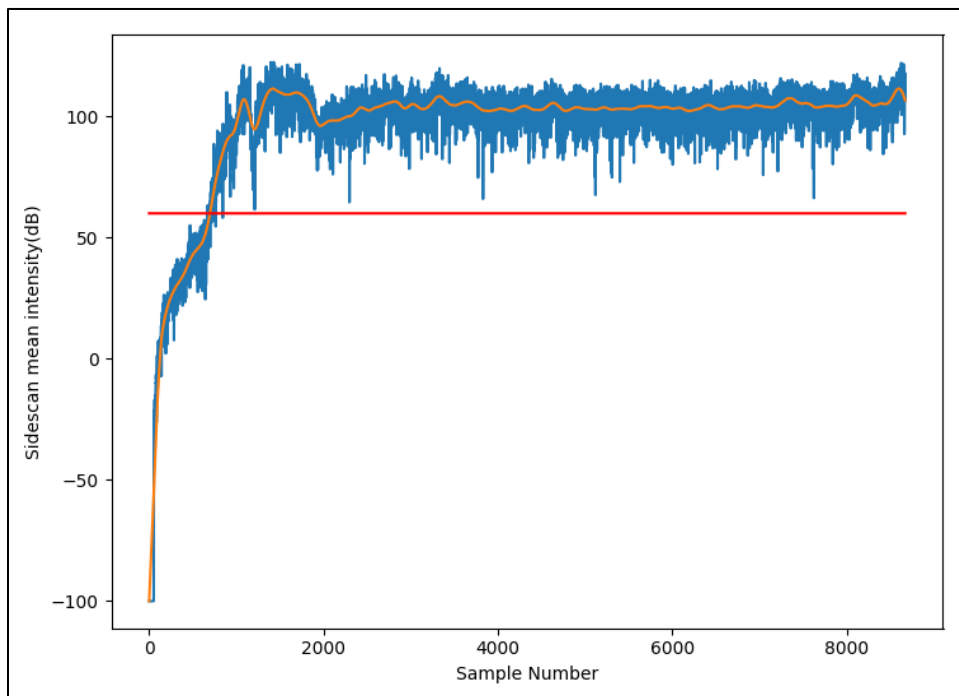


Figure 64 - Theoretical beam patterns (unsteered) that can be used in the algorithm.

Due to that, there is the need to progressively change the steering angle to the direction where the wavefronts are expected to arrive; in other words, there is a need to control how the array is steered as a function of time, as the echo changes in elevation angle. Given that the detection of a PMBS resembles a radar, in the sense that the wavefronts tend to arrive chronologically from the nadir to the far range, the array can be steered to the nadir until the first arrival, which is an instant characterized by a jump in the amplitude time series. Thus, the first arrival is the trigger to start the progressive beam steering.

### 3.3.1. The steering control

Estimating the first arrival involves defining an intensity threshold to determine when the jump will be considered to happen. The process needs to account for absorption and spherical spreading; otherwise, the first arrival will occur at different intensity levels, depending on the depth. Since calibrated backscatter is not a central concern of this thesis, the absorption coefficient used was roughly estimated to be 0.100 dB/m, with the only interest of processing signals independent of range. A TVG-corrected intensity time series can be seen in Figure 65.



*Figure 65 - Intensity time series (log scale). Blue: Intensity samples. Orange: moving average curve. Red: 60dB threshold.*

The time series were filtered using a 100-sample moving average forward and backward. In sequence, a threshold of 60 dB was used on the side scan time series to determine the first arrival time (Figure 65). This threshold was intentionally loose so that no valid bottom returns would be rejected.

Up to this moment, the information available is the nadir depth derived from the first arrival and the TWTTs obtained from the regular sampling. From there, a first estimate of the directions from where incoming wavefronts will reach the receiver can be derived considering a flat seafloor projection of the nadir depth, as follows:

$$est\_DOA = \arccos\left(\frac{nadir\_depth}{\frac{TWTT}{2} \times probe\_ss}\right) \quad (3.1)$$

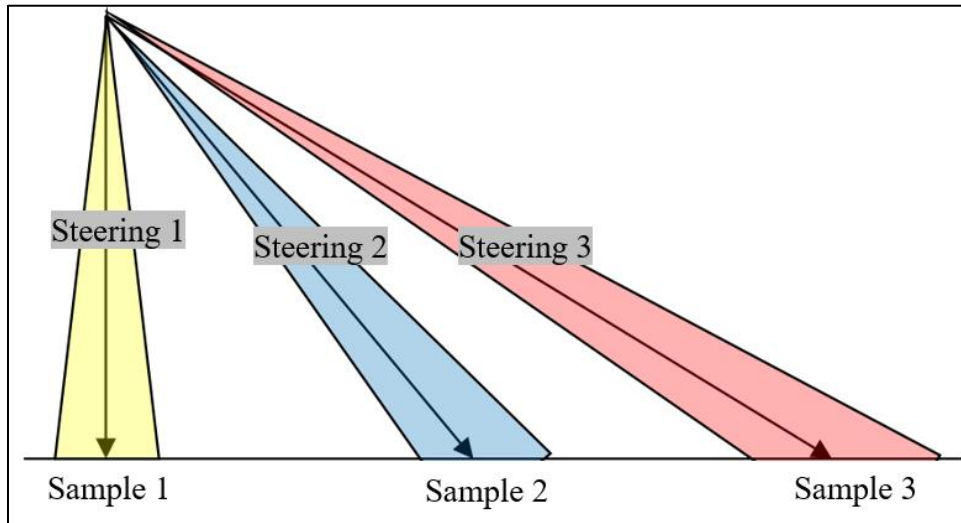


Figure 66 - An initial concept for the beam steering.

Using the estimated DOAs from Equation 3.1, the receivers can be progressively steered to face those DOAs, aiming to have the maximum energy from that expected direction. Implementing that idea, in a convention where positive steering angles are counterclockwise, a steering vector can be derived from a given estimated DOA vector by the relation:

$$\theta_{steering} = estimate\_DOA - 90^\circ + mount\_angle \quad (3.2)$$



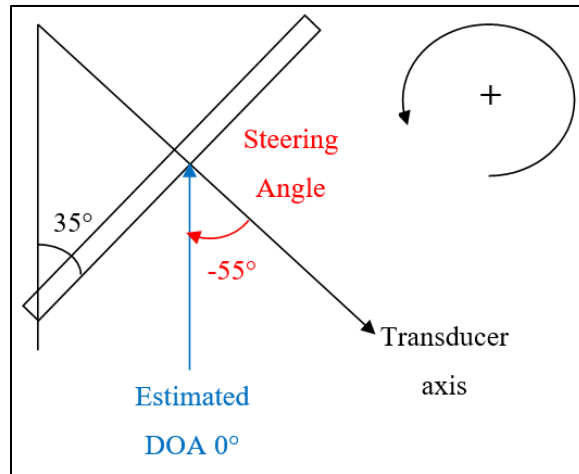


Figure 67 - Steering angle (red) for a  $0^\circ$  estimated DOA.

### 3.3.2. Converting beam steered differential phases to DOAs

Because phase shift beam steering alters the phases of each compounding stave before performing a summation (Equation 2.38), there is a need to review the differential phase-to-DOA conversion model for beam steered phasors. Suppose an array of three elements, beam steered to an angle  $\theta_{st}$ , and two virtual arrays formed by the elements 1-2 and 2-3. Consider that each element had an instantaneous phase of  $\varphi_0$ ,  $\varphi_1$ , and  $\varphi_2$  and received a multiple of  $\delta\varphi$  as the beamforming additional phase:

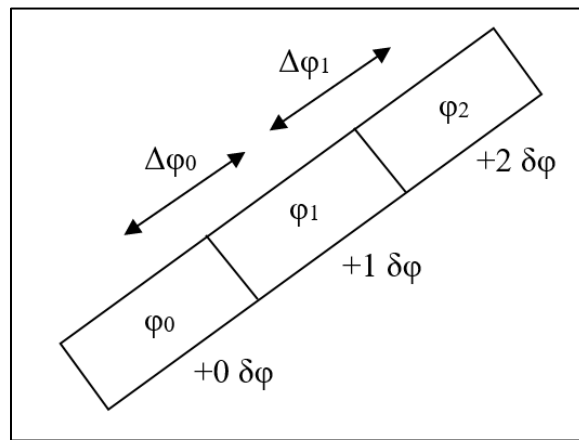


Figure 68 - Fictitious 3-stave array.

Besides, let us assume that the signal amplitudes received by each element are close and equal to  $\underline{A}$ . In that sense, the compounded signals ( $VT_n$ ) for the virtual arrays are given by:

$$\begin{aligned}
 VT1 &= A\angle\phi_0 + A\angle(\phi_1 + \delta\phi) \\
 VT1 &= A\cos(\phi_0) + jA\sin(\phi_0) + A\cos(\phi_1 + \delta\phi) + jA\sin(\phi_1 + \delta\phi) \\
 VT1 &= 2A\cos\left(\frac{\phi_0 + \phi_1 + \delta\phi}{2}\right)\cos\left(\frac{\phi_0 - \phi_1 - \delta\phi}{2}\right) + \\
 &\quad + j2A\sin\left(\frac{\phi_0 + \phi_1 + \delta\phi}{2}\right)\cos\left(\frac{\phi_0 - \phi_1 - \delta\phi}{2}\right) \\
 VT1 &= 2A\cos\left(\frac{\phi_0 - \phi_1 - \delta\phi}{2}\right) \times \left[ \cos\left(\frac{\phi_0 + \phi_1 + \delta\phi}{2}\right) + j\sin\left(\frac{\phi_0 + \phi_1 + \delta\phi}{2}\right) \right] \\
 VT1 &= 2A\cos\left(\frac{\phi_0 - \phi_1 - \delta\phi}{2}\right) \angle \frac{\phi_0 + \phi_1 + \delta\phi}{2}
 \end{aligned}$$

Analogously:

$$VT2 = 2A\cos\left(\frac{\phi_1 - \phi_2 - \delta\phi}{2}\right) \angle \frac{\phi_1 + \phi_2 + 3\delta\phi}{2}$$

The phase difference between  $VT_1$  and  $VT_2$  is then:

$$\begin{aligned}
 \Delta\phi_{st} &= \frac{\phi_0 + \phi_1 + \delta\phi}{2} - \frac{\phi_1 + \phi_2 + 3\delta\phi}{2} \\
 \Delta\phi_{st} &= \Delta\phi - \delta\phi
 \end{aligned} \tag{3.3}$$

But, from the phase beamforming Equation 2.38:

$$\delta\phi = -2\pi \frac{a}{\lambda} \sin(\theta_{st})$$

Then:

$$\Delta\phi_{st} = 2\pi \frac{a}{\lambda} \cos(\theta + \psi) + 2\pi \frac{a}{\lambda} \sin(\theta_{st})$$

$$\Delta\phi_{st} = -2\pi \frac{a}{\lambda} \sin(\theta + \psi - 90^\circ) + 2\pi \frac{a}{\lambda} \sin(\theta_{st})$$

Considering that  $\theta_{st}$  is the estimate for  $(\theta + \Psi - 90^\circ)$ , the approximation used by Lurton (2010) to define the beam pattern of a steered line array can be applied as follows:

$$\sin\theta - \sin\theta_0 = \cos\theta_0 \sin(\theta - \theta_0)$$

$$\Delta\phi_{st} = 2\pi \frac{a}{\lambda} \cos(\theta_{st}) \cos(\theta + \psi - \theta_{st}) \quad (3.4)$$

Equation 3.4 is similar to the original phase-to-DOA conversion model. However, two differences can be raised: the stave size in wavelengths is now projected by the steering angle, and the mounting angle is now deducted from the steering angle. This implies that the wavefronts behave as if they were received by the virtual array, with a projected size and a new mounting angle (Figure 69).

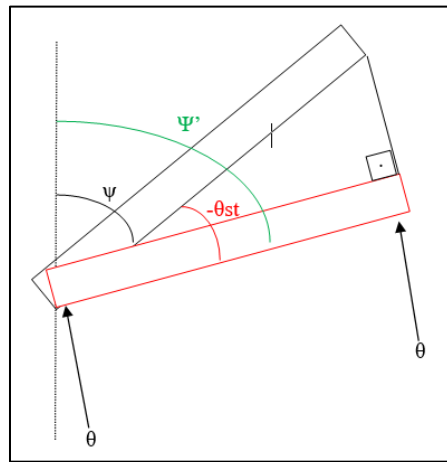


Figure 69 - Virtual mounting angle  $\Psi'$ .

### **3.4. Beamforming and Time Average**

The beamforming for each sample could be implemented in two ways. If each sample were being treated individually, local steering could be devised by deriving steering angles for each expected direction of arrival. Though, if any averaging or regression is being made across time, each locally steered sample would have its virtual mounting angle, incurring errors by simply averaging them using the window center virtual mounting angle. Due to that, there is a need for all the samples within each window to be beam steered at the same direction.

#### **3.4.1. Defining the discrete steps**

As sample sliding windows are to be used in this algorithm, the beam steering must be made in discrete angular steps to guarantee that all averaged samples follow the model derived in the previous section. Each discrete step had its complexes steered to the interval bisector, attempting to treat both sides of the window equally. Roll was not considered in this computation, as it was practically constant within the same ping. One aspect that needs to be mentioned is that samples at the edges of the step have windows surpassing the step limit, so a given number of samples at each step must be re-beam steered (Figure 70).

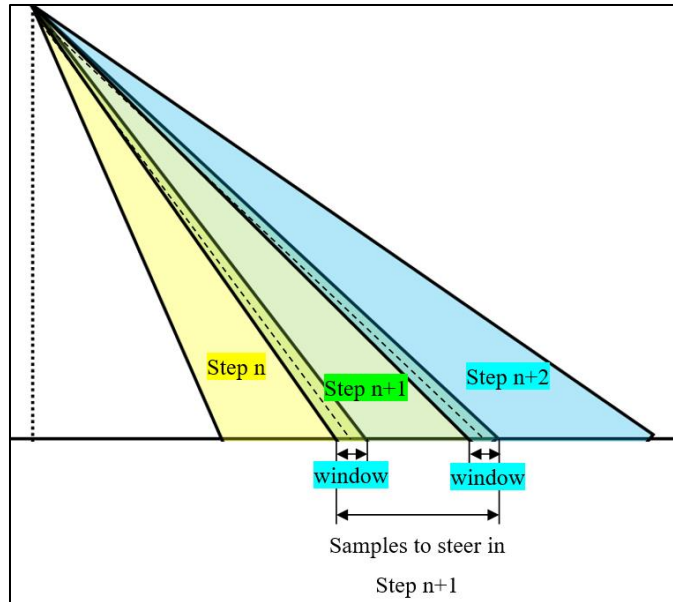


Figure 70 - Samples to be beam steered at each step.

When designing the step sizes, some issues must be taken care of. To begin with, the steps cannot extend to the point of reaching nulls in the beam pattern because the attenuation will distort the resultant phase (Figure 71). To avoid distortions, the half-power beam width may be considered the upper limit to the angular steps.

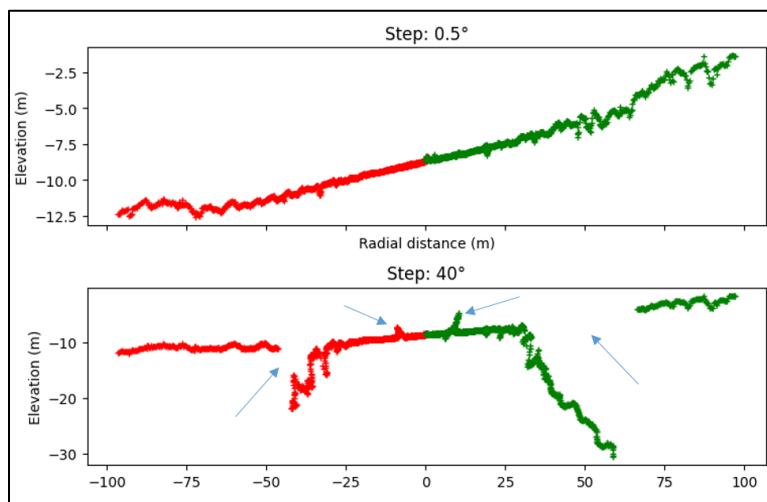


Figure 71 – Bottom detection with a step size lower than the HPBW (top) vs. a step higher than the HPBW (bottom). Discontinuities and artifacts due to nulls can be seen in the bottom plot (blue arrows).

### 3.4.2. The steering error

The larger the size of the steps, the more misaligned the main response axis and the DOAs obtained at the edges of each step. It was observed that this misalignment, now called the steering error, was distorting the obtained solutions. During the algorithm development, it was first noticed when the algorithm solutions matched well the EdgeTech solutions in the center of the swath but systematically diverged in the far range.

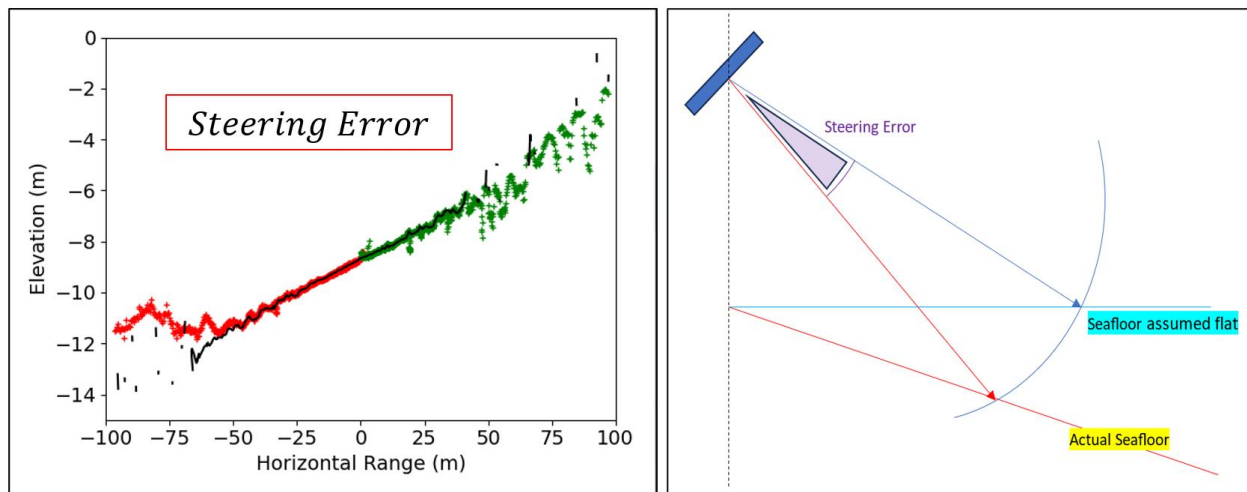


Figure 72 - A profile comparing the Algorithm and EdgeTech Solutions. Brown curve: Algorithm Profile. Green curve: EdgeTech Profile.

To understand this effect, the beam steered differential phase curve must be analyzed. Within the main lobe, the phase ramp is pretty much linear, though it is increasingly more curved and variant as the samples get further from the MRA (Figure 73). Besides, other phase ramps may be formed for sidelobes. In consequence, a steering error may lead to the inclusion of noisy samples in the averaging window, and to the amplification of uncorrelated noise at the direction of steering. As stated by Vincent (2013), as incoherent signals are included in the ensemble average, the differential phase is biased towards zero, causing depth solutions to drift towards the MRA.

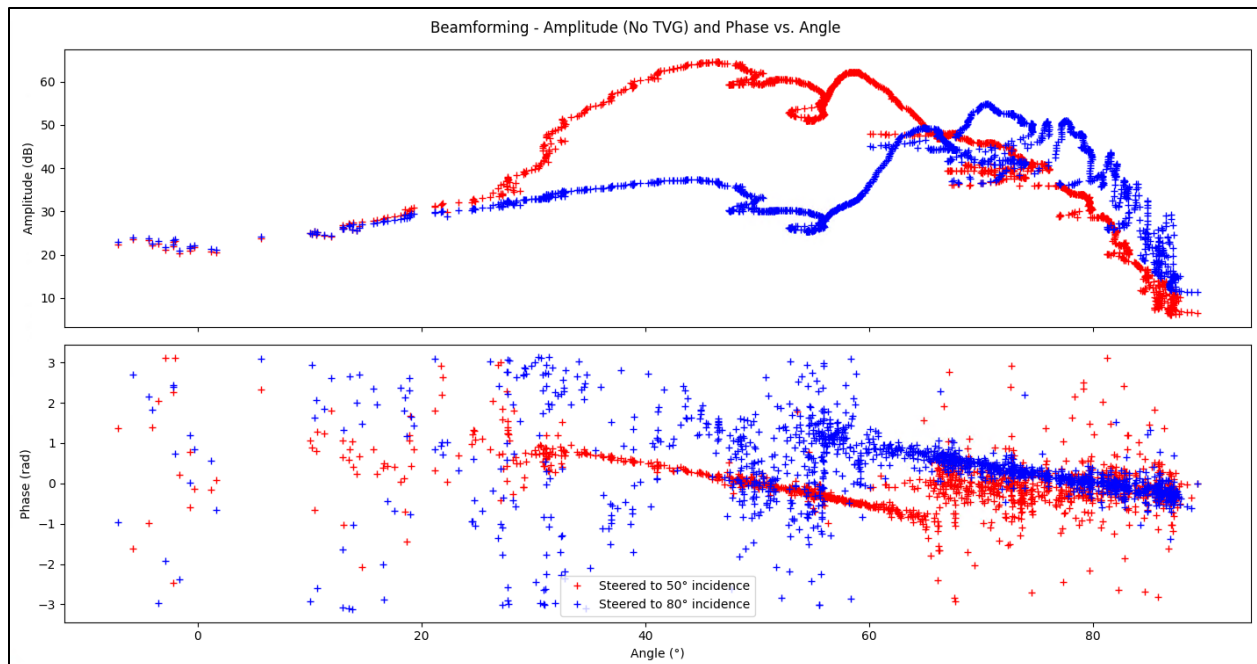


Figure 73 - Beamformed Amplitude and Phase Time Series.

### 3.4.3. Mitigating the steering error

Tests with the data showed that elevation changes in the seafloor increased the error between the expected direction of arrival for a flat seafloor and the actual one, distorting the DOAs resolved. That reinforces the statement that the drift is caused by processing sources that are actually far from the steering direction. To address this issue, two ways of mitigating the steering error were devised.

a) Recursively use previous solutions to update the steering direction:

In this method, after each step, an updated elevation was calculated using the median of all depths from previous iterations to mitigate this error so that the next steering angle matched the new height. To avoid including depths from shadows in this process, the median only considered solutions with at least a 12dB SNR. Figure 74 illustrates the relationship modeled by Equation 3.5 below:

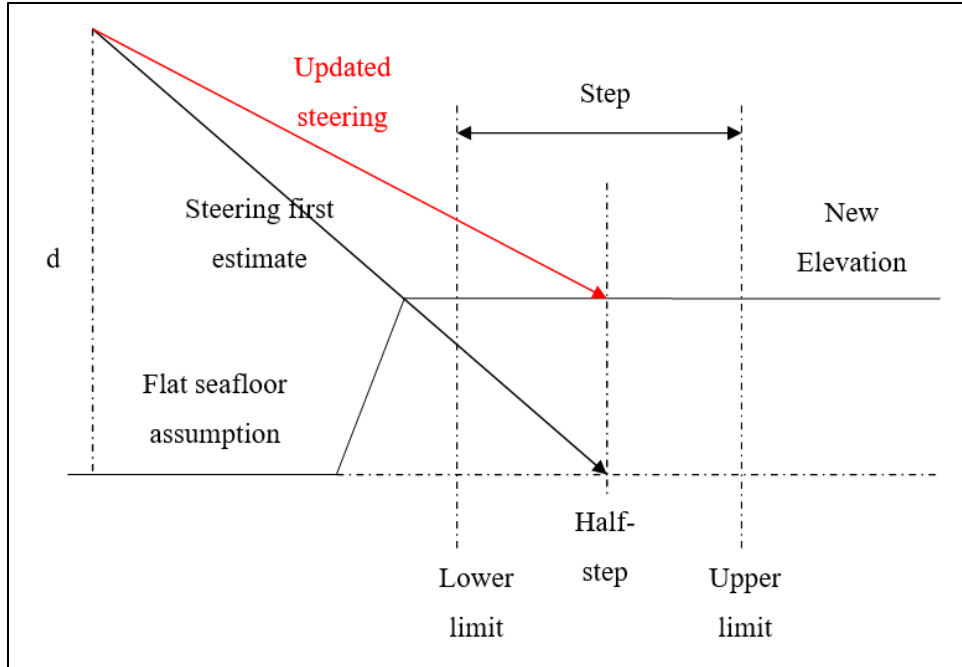


Figure 74 - The impact of changing elevation on the beam steering vector.

$$\theta_{st}^{n+1} = \frac{d^n \tan(\text{step}_{end}^n)}{d^{n+1}} + \frac{1}{2} \text{step\_size} \quad (3.5)$$

The results of correcting the steering angle can be seen in Figure 75. The smaller the angular step size, the more accurate the depth used as a reference for the steering angle calculation, which explains why smaller steps are more effective in mitigating the depth drift in the far range. Because of this, the algorithm was set to use an angular step of  $0.5^\circ$ . Another option that may be considered is using the previous ping profile to guide the steering.



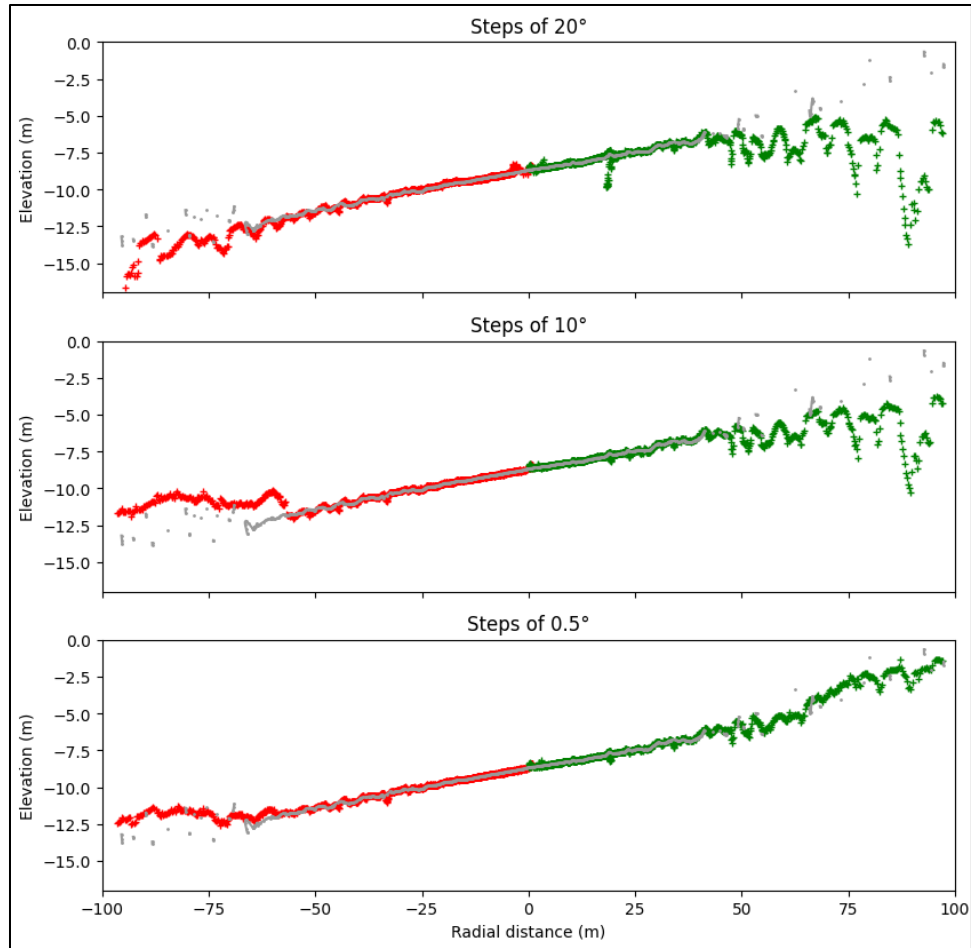


Figure 75 - Correcting the elevation in steps of  $20^\circ$ ,  $10^\circ$ , and  $0.5^\circ$ . EdgeTech solutions in gray.

Another aspect of importance is that even with the smallest possible angular step, there is still drift in the swath ends. That may be caused by the SNR decay due to the transmission loss, introducing higher levels of uncorrelated noise, biasing the DOAs towards the MRA, or alternately because depths were not accurate enough to guide the steering accordingly. Due to that, an alternative way of estimating the steering direction was devised, as explained further.

b) Steering the entire time series to fixed beamforming channels:

Considering that conventional beamforming applies the most gain at the steering direction, one could steer the whole time series to a set number of fixed channels, encompassing the angular

interval from where signals are expected to arrive, in this case, from  $0^\circ$  (normal incidence) to  $90^\circ$  (horizontal). Then, for each sample, the channel to be used for computing its solution would be the one with the higher resulting amplitude (Figure 76). The amplitude time series were filtered by a 100-sample back-and-forth moving average before making comparisons, as scintillation of raw amplitudes were making the algorithm occasionally choose the wrong channel, resulting in noisy solutions.

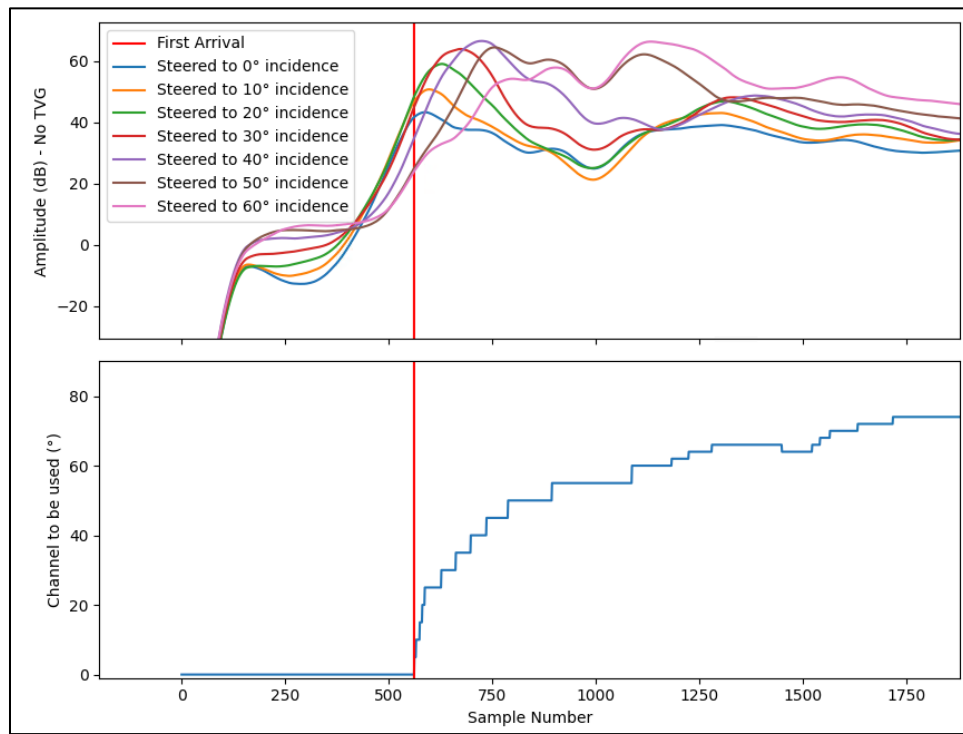
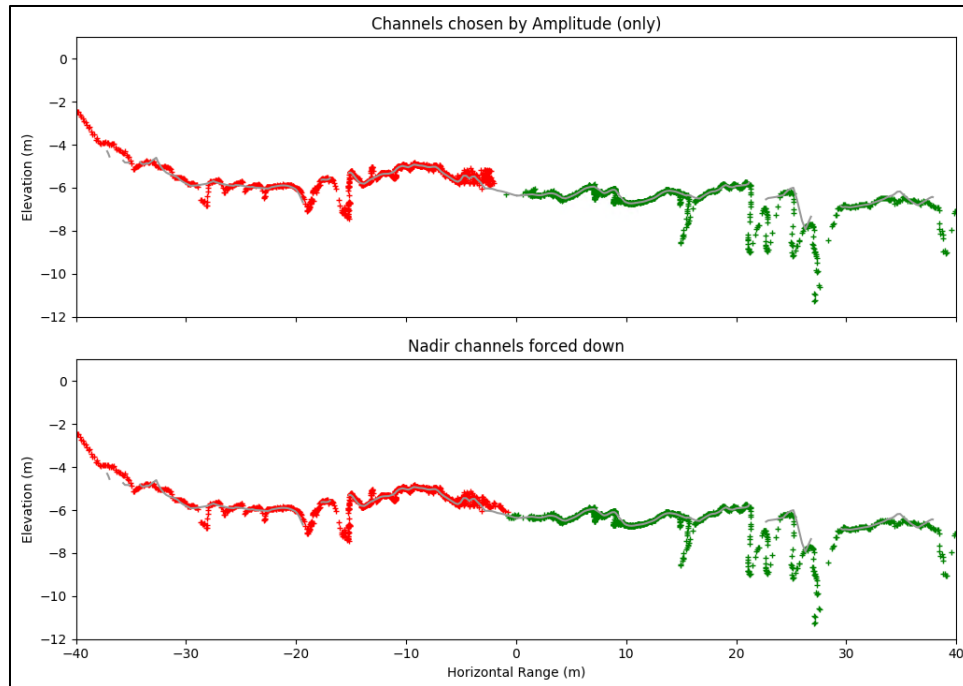


Figure 76 - Choosing beamforming channels using the Amplitude Time Series.

Using fixed beamforming channels yielded similar results to the recursively adapting the steering angle, except in the normal incidence. In this region, where the SNR is inherently lower (see section 2.8), water column returns had amplitude levels high enough to interfere with the bottom detection. Due to that, from  $0^\circ$  to  $15^\circ$ , the steering direction had to be forced down according to the flat seafloor estimated direction of arrival. At the normal incidence, this degree

of approximation was reasonable since the depth sensitivity to angular variations is very low near the nadir. The results can be seen in Figure 77.



*Figure 77 - Bottom detection using amplitude-chosen beamforming channels.*

Even applying amplitude-chosen beamforming channels, the loss of SNR in the far-range makes some degree of bias unavoidable. For this reason, the drifted solutions must be rejected in filtering processes, explained further. One point that needs to be highlighted is that the recursive steering solution is much more computationally efficient than using fixed channels, because the time series is steered only once in the former. Because of that, recursive steering was adopted as default. However, with available dedicated hardware (e.g., beamforming boards for each channel), the second method may be advantageous, as each sample is processed independently.

Other than that, adaptive beamforming methods may help improve the solution because there is no need to choose a direction to be amplified. Figure 78 compares the two methods of mitigating the steering error with the Root-Music result for the same ping (algorithm adapted from

Wang, 2018). Both were considered acceptable, as they yielded very close results to the Root-Music algorithm.

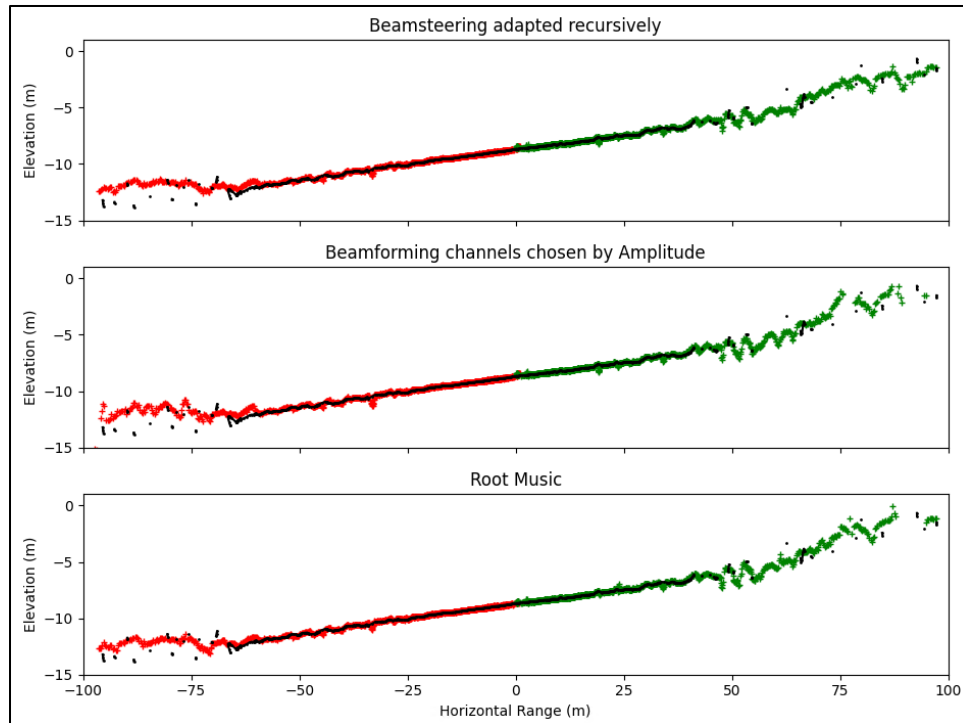


Figure 78 - Result from a Root-Music algorithm devised by Wang (2018) vs. Algorithms devised in this study. EdgeTech solutions in black.

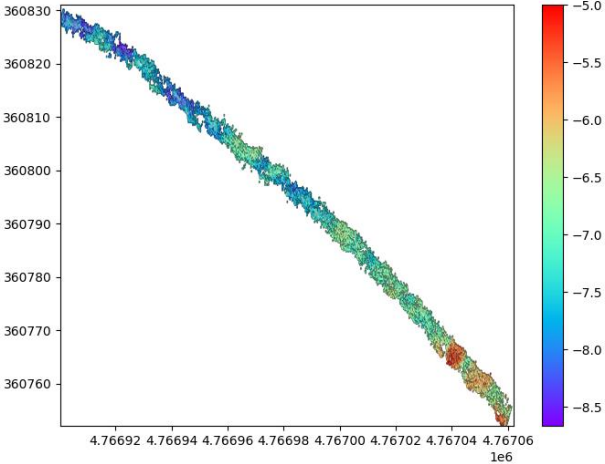
### 3.5. Beamsteering at nadir

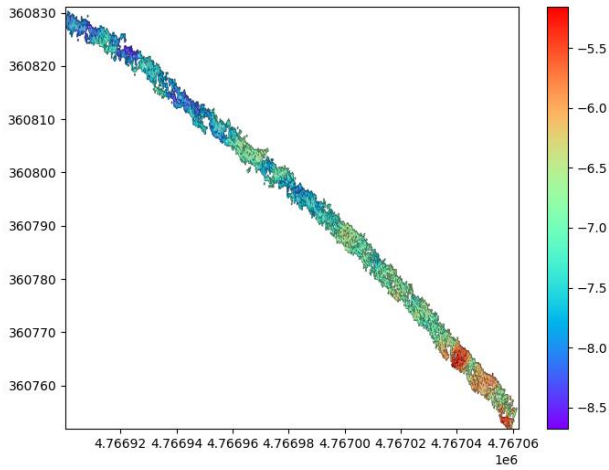
As mentioned in section 2.8.2, without receiver beamforming, solutions arriving from  $0^\circ$  to  $35^\circ$  (the EdgeTech 6205 mounting angle) can potentially interfere with signals from the symmetrical direction on the other side of the nadir. With beamforming, however, energy focusing and shading will attenuate interference from outside the main lobe, as already explained. That said, this system has a small number of staves when compared to the usual MBES, meaning that the beamformed beam widths are still considerably broad (even more when shading is applied).

With that in mind, for angles close to normal incidence, one could try to slightly deviate the MRA from the expected DOA in the first beam steering step (away from normal incidence and particularly the other side of the swath), attempting to attenuate the negative angles' contributions (from the other side of the nadir).

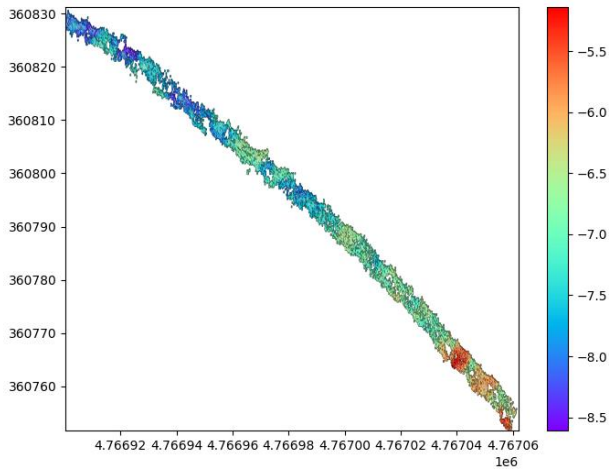
Applying this concept, solutions were computed for different steering angles at the first step, using a 9-element beamforming, starting from  $0.25^\circ$  (the smallest possible due to the window size), and then  $5^\circ$ ,  $10^\circ$ ,  $15^\circ$ ,  $20^\circ$  and  $25^\circ$ . Then, a whole line was processed for different first steering angles at the first step until the range of two meters. A grid with a cell resolution of 0.25 m was made to be compared to the EM2040P reference grid, which has that resolution. Creating a grid with a small cell size and cropping it to the area of interest is to avoid smoothing statistics by including data not affected by the parameter in evaluation. Then, Qimera's surface difference tool was used to evaluate how well each grid would agree to the reference dataset. The results can be seen in Table 11 below:

*Table 11 - Normal incidence steering statistics against the EM2040P reference dataset.*

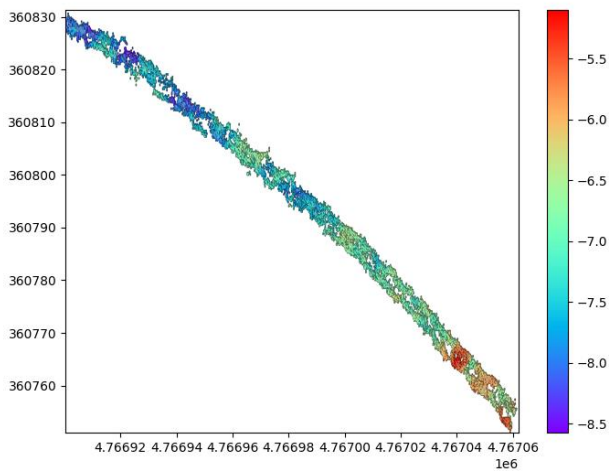
Grid	Surface difference statistics
	<p>MRA: <math>0.25^\circ</math></p> <p>Median: -0.05 m</p> <p>Mean: -0.09 m</p> <p>Std.Dev: 0.18 m</p>



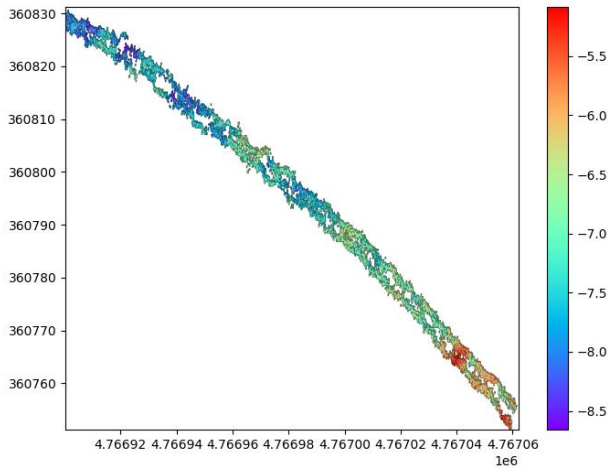
MRA: 5°  
 Median: -0.06 m  
 Mean: -0.10 m  
 Std.Dev: 0.20 m



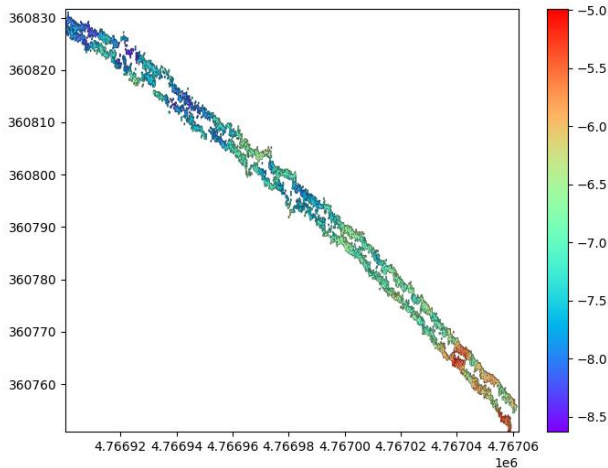
MRA: 10°  
 Median: -0.08 m  
 Mean: -0.12 m  
 Std.Dev: 0.20 m



MRA: 15°  
 Median: -0.08 m  
 Mean: -0.14 m  
 Std.Dev: 0.21 m



MRA: 20°  
 Median: -0.09 m  
 Mean: -0.15 m  
 Std.Dev: 0.21 m



MRA: 25°  
 Median: -0.10 m  
 Mean: -0.17 m  
 Std.Dev: 0.24 m

As seen in Table 11, the more steering is applied to the first step, the more gaps are seen close to the nadir and the less comparable are the solutions to the EM2040P dataset. What may be happening is the steering off nadir is resulting in amplification of water column noise, the same reason why the fixed channel algorithm was failing at normal incidence. As a result, the depth solutions at the nadir get corrupted and they are rejected by the filters, creating these gaps.

In conclusion then, steering directly to the nadir seems more beneficial than applying steering deviations from the MRA, because the amplification of noise from the steering deviation

caused more signal corruption than the common slant range interference. Due to that, the bottom detection algorithm was set to make the first steer at  $0.25^\circ$ .

### 3.6. Beamforming algorithm implementation

The concepts built in the previous steps were, then, implemented. First, all samples are steered within each angular step interval, plus the additional samples on the borders. This logic was devised by setting at least two virtual split-arrays.

Equation 2.3 was modeled for collinear staves, so a vertical offset would change the Phase-to-DOA model. To combine these staves using the conventional beam steering equation, it is important to use a common element as the pivot, so that no vertical offset is created between the virtual arrays. Figure 79 illustrates the difference in geometry between the two cases:

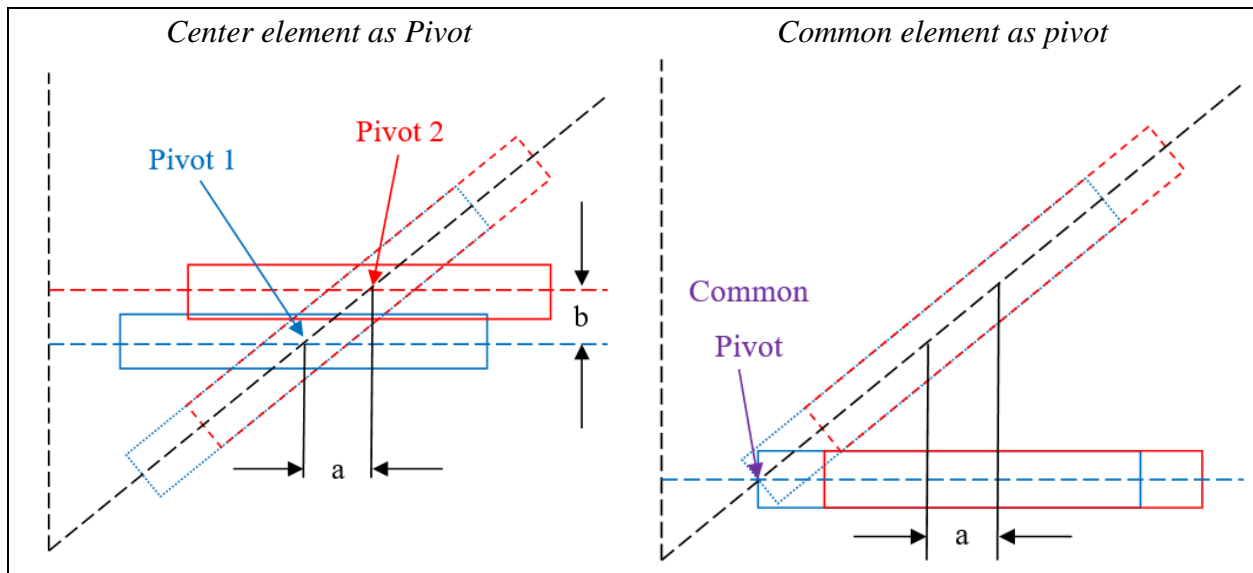


Figure 79 - Center pivot beam steering (left) and Common pivot beam steering (right).

In this study, the edge pivot center geometry was chosen to perform the beam steering so that Equation 2.7 could be used directly.



### 3.6.1. Stave spacing calibration

One challenge of this study was somehow estimating the stave spacing, a known parameter by the manufacturer but not precisely documented. EdgeTech (2022) do clearly state that the elements are spaced by half-wavelength, though. In that line of thought, this study assumed that the array was built to achieve half-wavelength at a specific sound speed value and a 520 kHz center frequency (as registered in the JSF datagram). The equations that needed the spacing were modified to a ratio between the design sound speed and the actual environment sound speed:

$$\frac{d}{\lambda_{actual}} = \frac{b\lambda_{design}}{\lambda_{actual}} = b \frac{\frac{c_{design}}{f}}{\frac{c_{actual}}{f}} = b \frac{c_{design}}{c_{actual}} \quad (3.6)$$

Since using the wrong design sound speed would distort the final results, the strategy devised to estimate the actual physical stave spacing was comparing the study's algorithm solutions for a set of design sound speeds and EdgeTech solutions (Figure 80). This calibration was made with the Vernier algorithm since the steering error could influence the beamsteering results.

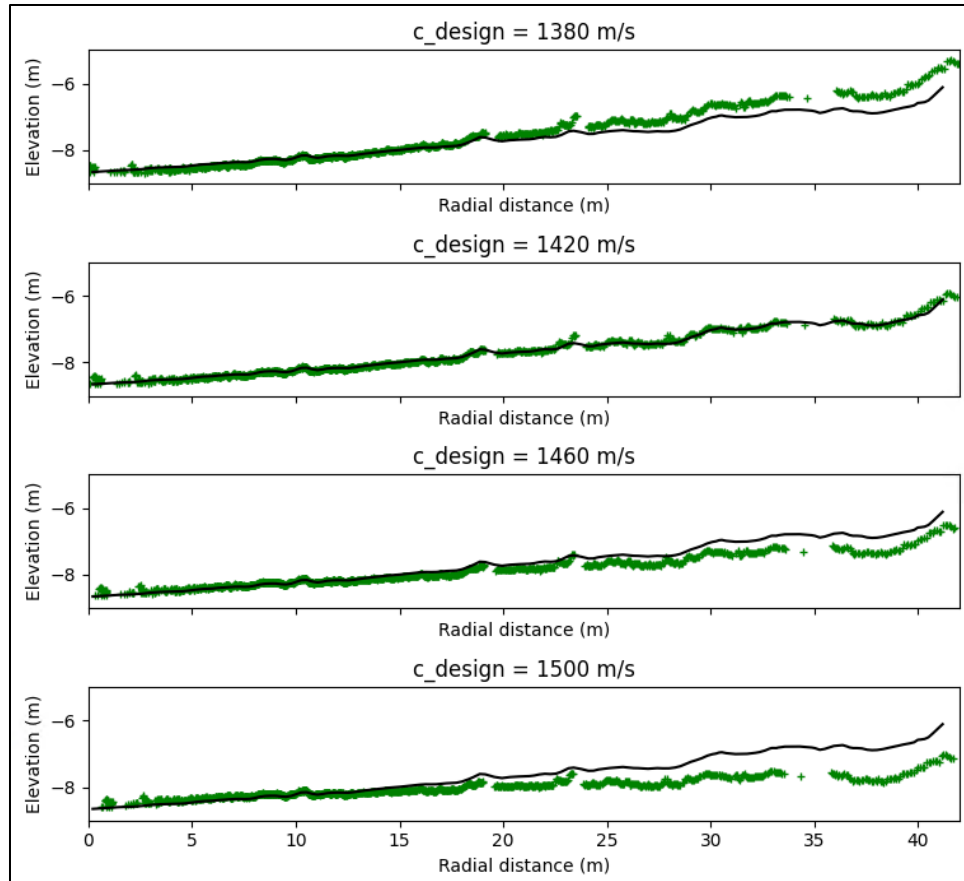


Figure 80 - Calibration of the sound speed of the design using Vernier solutions. EdgeTech solutions in black.

During the comparison tests, it was noticed that varying the design sound was causing either a frown or a smile pattern in the swath, somewhat analogous to the errors of applying a wrong sound speed profile in ray tracing. That said, the design sound speed assumed as accurate was the one that made the algorithm solutions best fit the EdgeTech solutions. This comparison was made graphically in steps of  $10^\circ$ , and the chosen value was 1420 m/s.

The chosen design sound speed was standardized in all models used in this study that depended on the element spacing. However, in real applications, this value is expected to be known precisely by the manufacturer, as said before. Applying the mentioned adaptations to Equation 2.38 yields:

$$VT_n = \sum_{k=0}^{2k} w_{Cheb(-40)} s_k(t) \exp\left(-2j\pi b \left(k + \min\_channel_n // 2\right) \frac{c_{design}}{c_{probe}} \sin\theta_{st}\right) \quad (3.7)$$

To verify the behavior of Equation 3.7, the beam steered complex intensities were checked using an intensity plot vs. slant range (Figure 81). The data was from a line run with a 3.7 ms pulse length with the sonar at about 9-meter altitude.

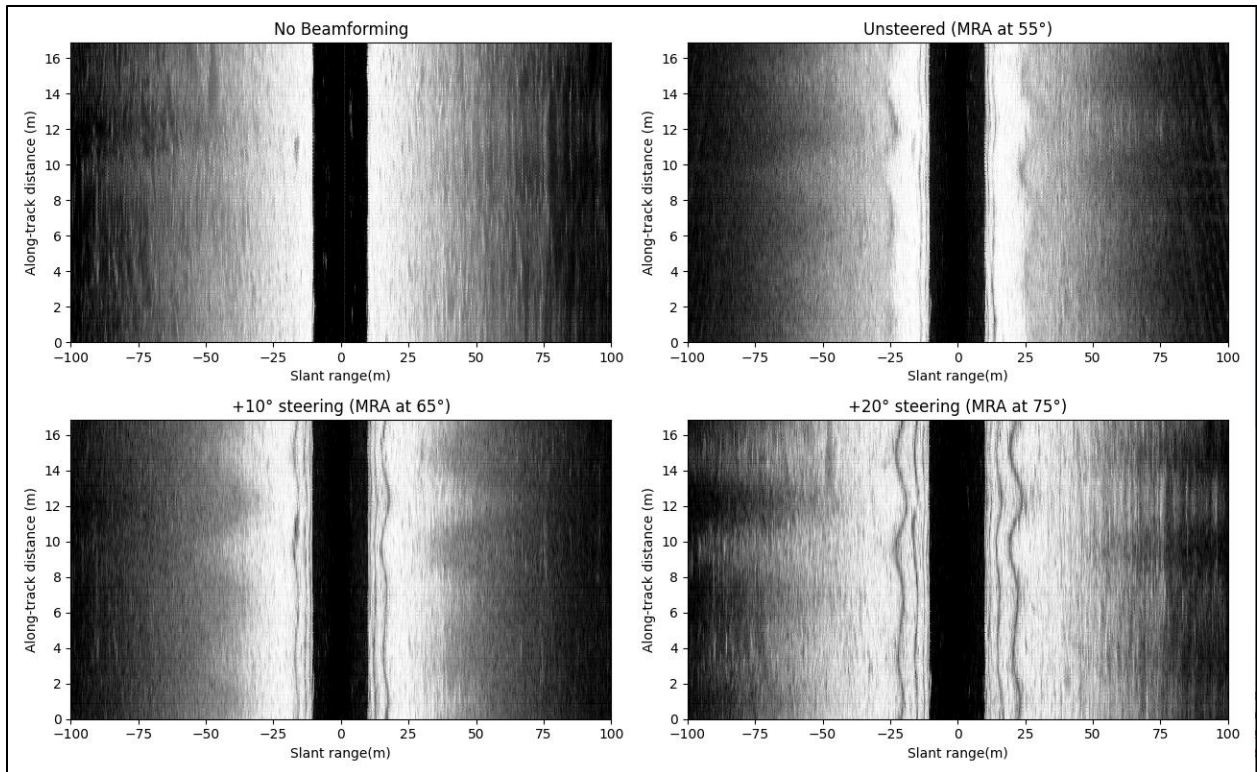
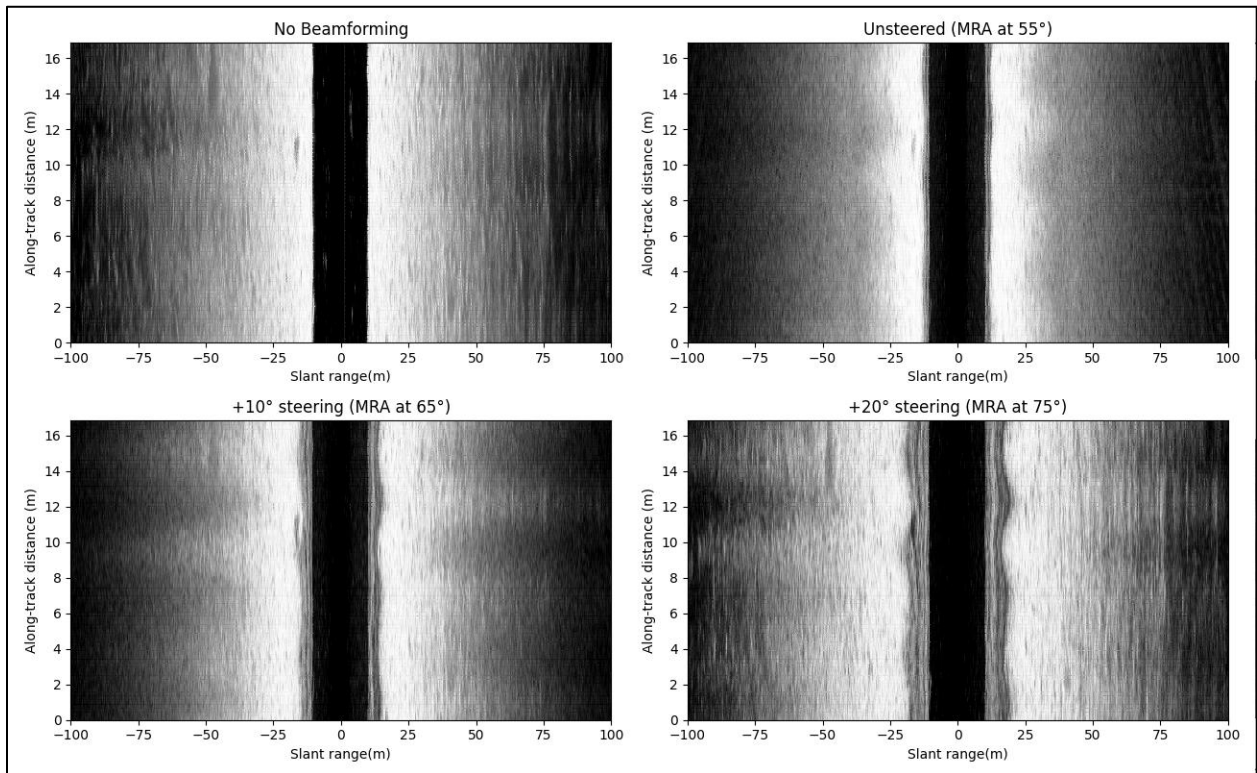


Figure 81 - Unshaded beam steered intensities (No TVG).

Using the non-beamformed image (top left) as a reference, it is possible to notice in the beamformed counterparts a lighter area caused by the main lobe constructive interference in the steering direction. As expected for a 9-meter altitude configuration, the main lobes for steering angles of 0°, 10°, and 20° are centered respectively at about 16 m, 21 m, and 35 m horizontal

range. The nulls can also be seen as dark stripes, where interstave destructive interference is prevalent, causing extremely low amplitudes. This grid was created without motion compensation, explaining the wavy behavior of the lobes and nulls.

In turn, Figure 82 was obtained by applying Chebyshev weights for a sidelobe level attenuation of 30 dB, maintaining the same conditions as Figure 81:



*Figure 82 - Beam steered intensities (No TVG), Chebyshev shading SLL -30dB applied.*

Once the Chebyshev shading is applied, it is possible to notice that the lighter area is now broader, reflecting the main lobe beamwidth increase. Consequently, the nulls were displaced inwards, and more importantly, the regions between nulls are much darker, proving that the shading attenuated the sidelobe levels. The shaded beam steering is justified to reduce the phase interference coming from sidelobes. In this context, the beamforming really worked as a spatial

filter, amplifying signals from the direction of interest while attenuating other sources. At the same time, the shading mitigates the beamforming weakness of developing sidelobes in unwanted directions.

### 3.6.2. Averaging phases

Each sample was steered to the center of the step it belongs, resulting in vectors of steered complexes for each virtual array. After that, the complex product array, corrected for TVG, was obtained using Equation 3.8:

$$Complex\_Products = VT_1 \times VT_2^* \times 10^{\frac{TVG(dB)}{10}} \quad (3.8)$$

Finally, the phase average is calculated by summing the beam steered samples inside the window estimated for each sample. In contrast to what was proposed in 2.7.1, these vectors were purposely not normalized to apply more weight to strong signals. With that, weak multipath interference has less contribution, and shadows within the window will cause fewer distortions to target detection. As intensities are used as weighting, the correctly chosen TVG factor is needed not to overweight the first window samples compared to the last ones. Besides, the Signal-to-Noise Ratio (SNR) estimate within each window, explained in Chapter 2, can also be biased if TVG is not applied.

A disadvantage of not normalizing the vectors is that, when trying to make detections in shadowed areas, the phase average will be biased toward proud targets that cause shadows. However, since returns from shadows are usually inaccurate, it is reasonable to reject the returns from shadows and prioritize having fewer distortions of proud objects. After summing the vectors, the phase average is obtained by taking the argument of the result. Then, it is multiplied by the

factor  $B/\sin(B)$  (Equation 2.20) and converted to DOA using Equation 2.7. Figure 83 and Figure 84 compare the effect of normalizing or maintaining the complex products' amplitudes during the phase averaging in a single ping. Amplitude-weighted complexes significantly helped in having a clearer target detection.

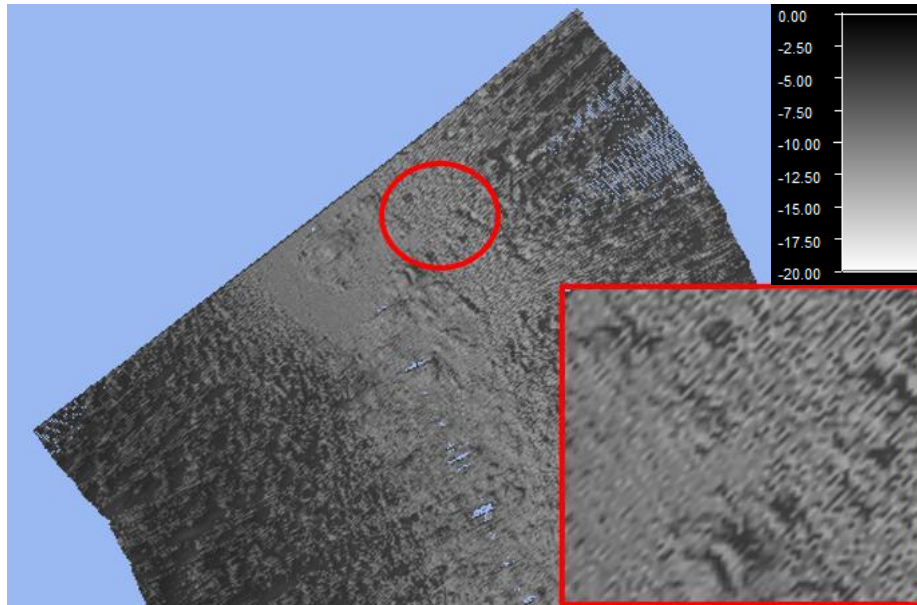


*Figure 83 - Bathymetric grid of normalized complex products.*

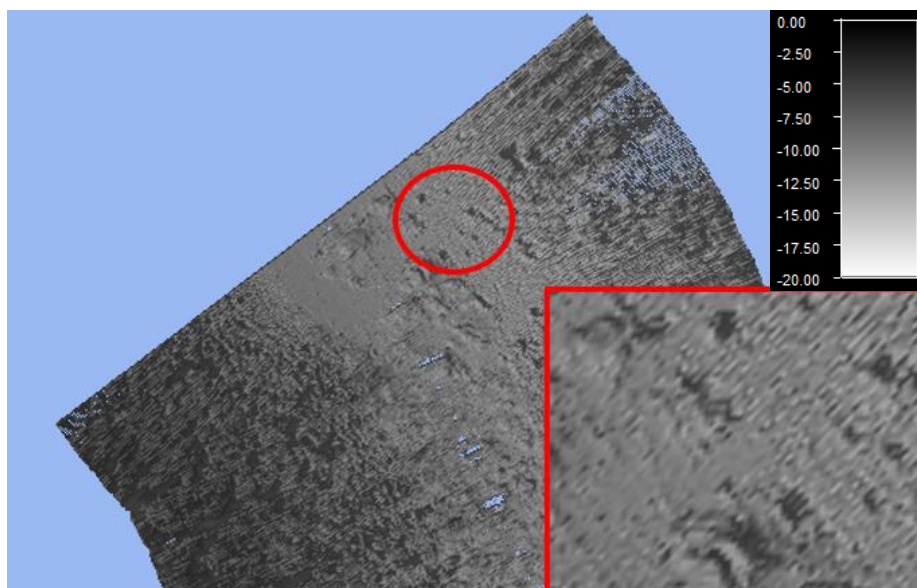


*Figure 84 - Bathymetric grid of amplitude-weighted complex products.*

### 3.6.3. Estimating the angular uncertainty

In deriving depths, it is equally important to evaluate how accurate the dataset is. Considering that, it is possible to estimate the angular variance from the model used to convert the phase average into DOAs, by differentiating the equation under the law of propagation of uncertainties. Applying it to Equation 3.4 yields:

$$\sigma_{\Delta\phi}^2 = \left(\frac{\partial\Delta\phi}{\partial\theta}\right)^2 \sigma_{\theta}^2$$

$$\sigma_{\theta}^2 = \frac{\sigma_{\Delta\phi}^2}{\left[2\pi b\cos(\theta_{st}) \frac{c_{design}}{c_{actual}} \sin(\theta + \psi - \theta_{st})\right]^2} \quad (I)$$

In (I), the denominator is known for each sample, but the numerator must be found by estimating the phase uncertainty. From Equation 2.20, the last can be calculated from the phase average uncertainty:

$$\sigma_{\Delta\phi}^2 = \sigma_{\overline{\Delta\phi}}^2 \times \frac{B}{\sin B} \quad (II)$$

Following this, the phase average uncertainty can be obtained from the window average for each sample. Given that the complexes' amplitudes are not supposed to affect the phase information, the derivation follows using the normalized complexes  $\underline{z}$ :

$$\overline{\Delta\phi} = \text{argument} \left( \sum_{\text{window}} \hat{z} \right) = \arctan \left( \frac{E\{Im(\hat{z})\}}{E\{Re(\hat{z})\}} \right) \pm k\pi, k \in \mathbb{Z}$$

Assuming circular symmetry between real and imaginary parts, the covariance matrix of the real and the imaginary sets is:

$$Cov(Re, Im) = \begin{bmatrix} \sigma_{Re}^2 & \sigma_{Re}\sigma_{Im} \\ \sigma_{Im}\sigma_{Re} & \sigma_{Im}^2 \end{bmatrix} = \begin{bmatrix} \frac{1}{2}\sigma_z^2 & 0 \\ 0 & \frac{1}{2}\sigma_z^2 \end{bmatrix}$$

Representing the expected values of imaginary and real parts as  $\overline{Im}$  and  $\overline{Re}$ , yields:

$$\begin{aligned} \sigma_{\Delta\phi}^2 &= \left(\frac{\partial\Delta\phi}{\partial\overline{Im}}\right)^2 \sigma_{Im}^2 + \left(\frac{\partial\Delta\phi}{\partial\overline{Re}}\right)^2 \sigma_{Re}^2 \\ \sigma_{\Delta\phi}^2 &= \frac{1}{2}\sigma_z^2 \times \left[ \left(\frac{\overline{Re}}{\overline{Re}^2 + \overline{Im}^2}\right)^2 + \left(\frac{\overline{Im}}{\overline{Im}^2 + \overline{Re}^2}\right)^2 \right] \\ \sigma_{\Delta\phi}^2 &= \frac{1}{2} \frac{\sigma_z^2}{\overline{Re}^2 + \overline{Im}^2} \end{aligned} \quad (III)$$

Substituting (II) and (III) into (I):

$$\sigma_{\theta}^2 = \frac{B\sigma_z^2}{2\sin B(\overline{Re}^2 + \overline{Im}^2) \left[ 2\pi b\cos(\theta_{st}) \frac{c_{design}}{c_{actual}} \sin(\theta + \psi - \theta_{st}) \right]^2} \quad (3.9)$$

Where  $\sigma_z^2$  is the variance of complexes within each window. Figure 85 presents the angular standard deviation obtained using Equation 3.9.



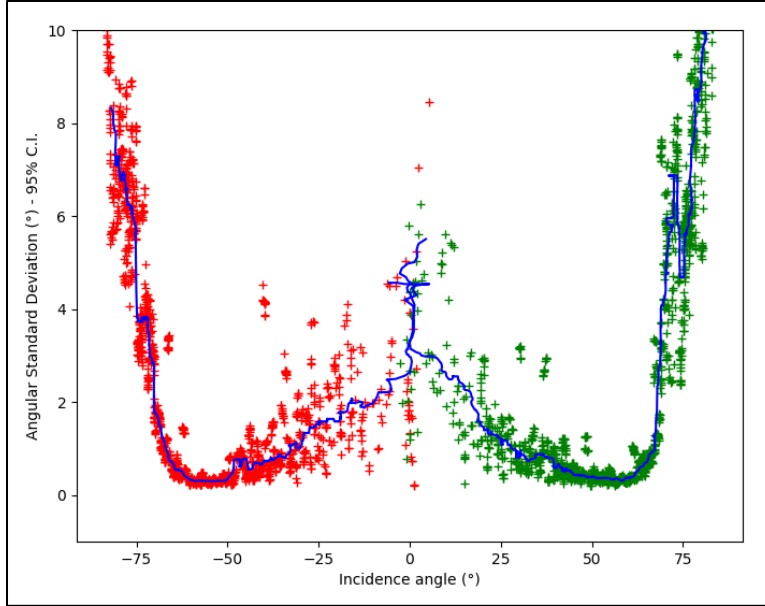


Figure 85 – Angular standard deviation vs. Incidence angle. Blue: 100 samples standard deviation running median.

The angular uncertainty is clearly higher near-nadir. The case shown in Figure 85 has a standard deviation median varying from 3° to 5° at nadir, due to the lower SNR at that region. It then decreases to a minimum of 0.4° at about 60° incidence angle, from where it abruptly diverges, due to the phase difference inherent uncertainty increase (see section 2.7.4) and to the SNR loss with range.

This angular uncertainty may be combined with the timing uncertainty (known by the manufacturer) and the other ancillary systems' uncertainties to estimate the total depth and positioning uncertainty after integration. Assessing the depth uncertainty, in an assumed homogeneous sound speed field, leads to the following expression:

$$d = \frac{ct}{2} \cos\theta$$

$$\sigma_d^2 = \left(\frac{t \cos\theta}{2}\right)^2 \sigma_c^2 + \left(\frac{c \cos\theta}{2}\right)^2 \sigma_t^2 + \left(\frac{ct \sin\theta}{2}\right)^2 \sigma_\theta^2 \quad (3.10)$$

By using the last term of Equation 3.10, the depth uncertainty contribution from the angular uncertainty can be evaluated, as in Figure 86.

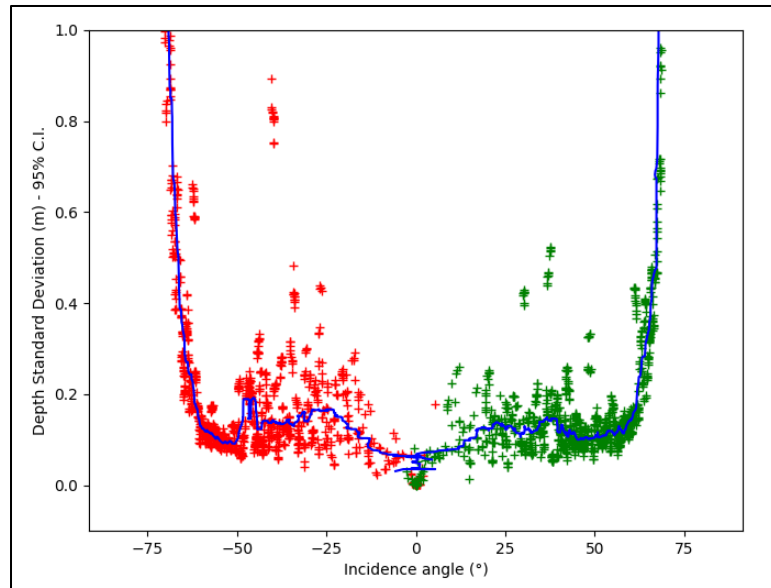


*Figure 86 - Depth standard deviation vs. Incidence angle. Blue: 100 samples standard deviation running median.*

After computing the depth standard deviation, it is noticeable that the uncertainty at nadir greatly reduced to less than 10 cm. That is explained because the depth sensitivity to angle variation in normal incidence is exceedingly small, so even higher values of angular uncertainty will not terribly affect the results in this region. In the far range, the uncertainty divergence is delayed from 60° to 65°, reaching one meter at about 70°.

#### 3.6.4. Improving efficiency

Making the algorithm computationally efficient was not one of the main objectives of this study. Nevertheless, some strategies were implemented to help with the processing speed. First, it is notable that adjacent sample windows may overlap considerably. In that case, instead of

summing all the complexes inside the window at each sample iteration, the phase sum was obtained incrementally from the previous sample.

Although it decreased the processing time, the main gain in efficiency was obtained by skipping samples as the processing goes further in the across-track range. This is justified because the further the range, the wider the horizontal range within the angular window established, so the independence between adjacent samples decreases with the radial distance. As a result, down-sampling progressively the solutions as the range increases may not negatively impact the seafloor model achieved, depending on how many samples are skipped. The sample skipping in this algorithm was implemented by specifying the desired percentage of overlap between adjacent sample windows. By setting a 94% overlap between windows, each ping could be processed five times faster, without losing significant density at far-range.

### 3.6.5. Filtering

The filters defined in section 2.10 were used to reject potentially unreliable data, by using thresholds set empirically by analyzing the dataset. The thresholds used for the beamforming algorithm were summarized in Table 12.

*Table 12 - Filter thresholds used for the beamforming algorithm.*

<b>Parameter</b>	<b>Threshold</b>
Window intensity	70 dB
Coherence	0.95
SNR	12 dB
Standard deviation (1 sigma)	5°

In addition to the filters, a horizontal binning was implemented to reduce the depth variance and to make geo-referencing and gridding scripts run faster, as fewer samples are being processed.

To perform this binning, which strictly should be done in true geographic coordinates, the refracted ray path was ignored, thus assuming a homogeneous sound speed profile, equal to the probe reading, to convert the TWTTs and DOAs into approximate depths and horizontal ranges (Equations 2.14 and 2.15). Then, horizontal cells are made using the chosen bin size, and each cell receives the median of depths and DOAs within the cell limits. The median was used instead of the mean value so as not to be affected by outliers. After that, the nominal cell depths and DOAs are converted back to TWTTs and DOAs, to have a comparable output to the EdgeTech solutions. Figure 87 below shows the result of the whole filtering process. The thresholds set were able to reject most questionable depths, notably the vast spikes from shadows that appeared below the grid.

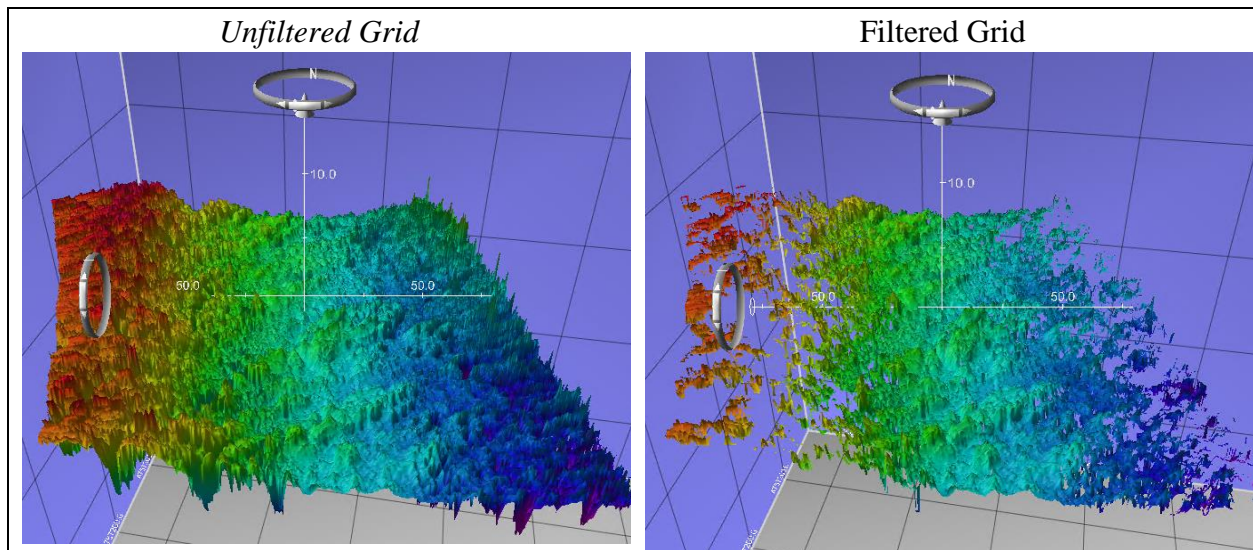


Figure 87 - Unfiltered vs. Filtered bathymetry grid.

### 3.6.6. Algorithm overview

The phase bottom detection algorithm devised during this study can be summarized as follows:

- 1) Calculate the TWTT array.
- 2) Estimate the time of first arrival from the amplitude time series and calculate the nadir depth.
- 3) Using the TWTTs, estimate DOAs for the nadir depth.
- 4) Set the array  $\underline{B}$  with the angular windows to be used for each sample.
- 5) Calculate the corrector  $B/\sin(B)$ .
- 6) Convert the angular windows to the sample domain (flat seafloor at the nadir depth).
- 7) Choose which samples to resolve based on the overlap percentage set.
- 8) Calculate the steering parameters for the first step.
- 9) Iterate until the last sample:
  - 9.1) Steer the samples needed for the present step.
  - 9.2) Calculate the window phase average and resolve DOAs for the present step.
  - 9.3) Calculate the quality metrics for the present step.
  - 9.4) When the final sample of the step is reached:
    - Update the elevation.
    - Estimate the next step interval.
    - Estimate the next step steering angle.
    - Advance one step.
- 10) Filter the time and angle arrays based on the quality metric thresholds set. A flag array may be used not to lose the rejected information.
- 11) Return TWTTs, DOAs, quality metrics, and flags (if used).

### 3.7. Data visualization and analysis

To establish a meaningful comparison between the algorithm solutions, the EdgeTech solutions, and the EM2040P reference grid, the time-angle pairs obtained by the in-house algorithm must be converted to rigorously geo-referenced depths. Three scripts were devised to achieve this: integration, vertical datum correction, and gridding.

#### 3.7.1. Integration

The sensor integration script used in this study was adapted from the UNH Seabed Mapping Course Lab 4, devised by Prof. Semme Dijkstra. The sensor lever arms, and the waterline height were introduced as manual inputs. At the same time, motion and position information were extracted from the JSF datagram and interpolated to the transmit time and each of the sequential wavefronts' times of arrival. The ship position considered for the integration was the mean point between the signal transmission and reception (Figure 88) so that the draft to be used for ray tracing could be estimated (Figure 89).

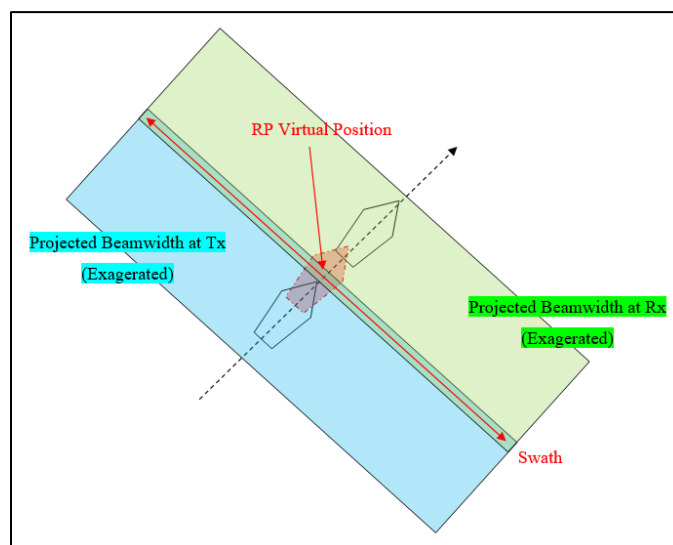


Figure 88 - Ship position considered for integration.

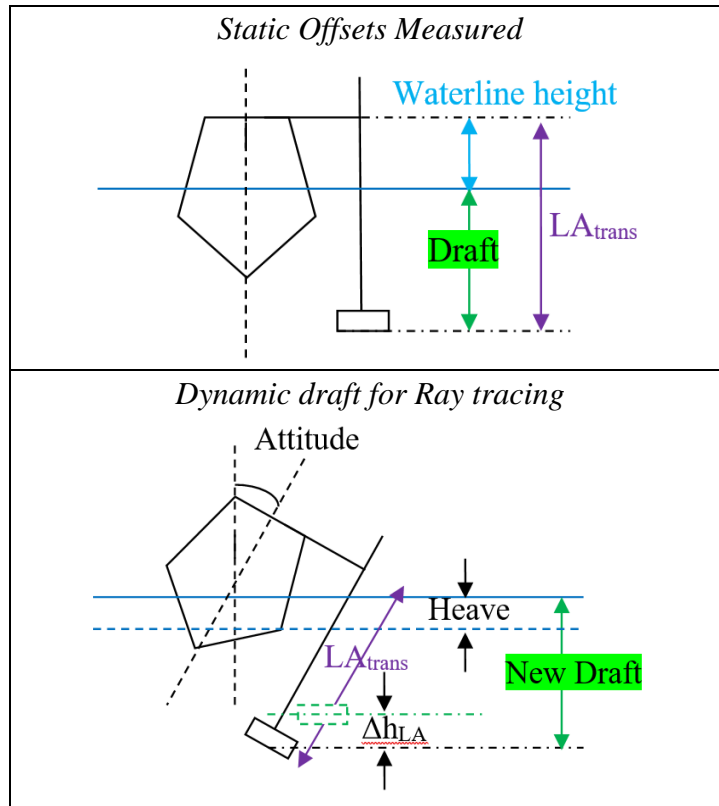


Figure 89 – Draft used for Ray tracing.

Another needed estimate for the ray tracing process is the depression angle at the transducer head. The beam vector was considered normal to the transducer head in the horizontal plane, being depressed by the complement of the DOA. This beam vector was rotated by the attitude at reception to calculate the depression angle and the swath azimuth.

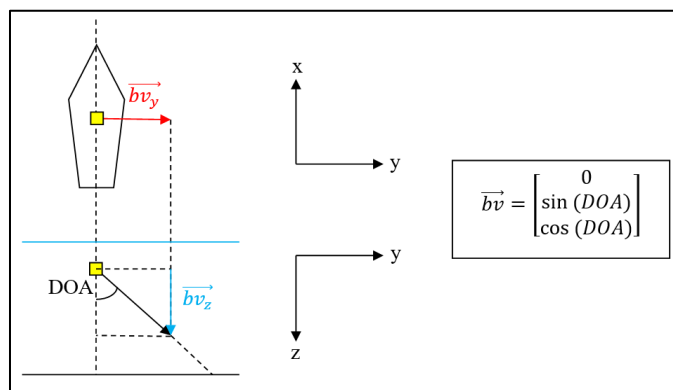


Figure 90 - EdgeTech 6205 beam vector.

In sequence, the estimated draft is used with a sound velocity profile to ray trace each time-angle pair as described in Hughes Clarke (2021), obtaining pairs of radial distances and depths.

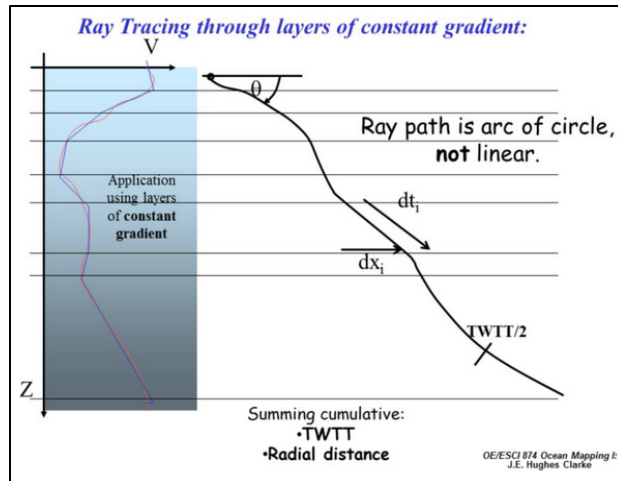


Figure 91 - The Ray Tracing process. Retrieved from Hughes Clarke (2021).

Finally, the radial distances, oriented to the swath azimuth, are projected into the UTM axes, and summed to the transducer geo-referenced lever arm and the ship geo-referenced position (at the origin). The result of the integration script is a 4-column database containing time, eastings, northings, and depths.

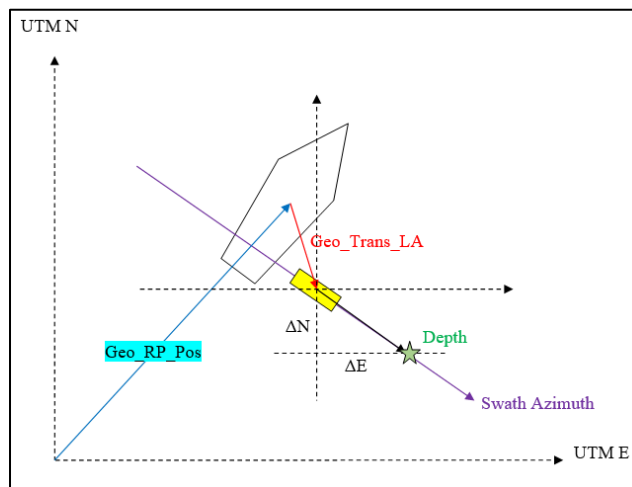


Figure 92 - Geo-referencing depths.



The integration logic used in this study was validated by comparing EdgeTech solutions of a given line, processed by the code, vs. Qimera. Negligible differences were noted, probably due to slight differences in the gridding process.

### 3.7.2. Vertical datum correction

The survey was conducted to the instantaneous water level, a dynamic datum affected by tides, winds, and other environmental parameters. To avoid vertical mismatching due to the datum change with time, the database depths were reduced from water level measurements to the MLLW datum from the Seavey Island NOAA station (#8419870), interpolated to each depth time. All measurements are available online at <https://tidesandcurrents.noaa.gov>.

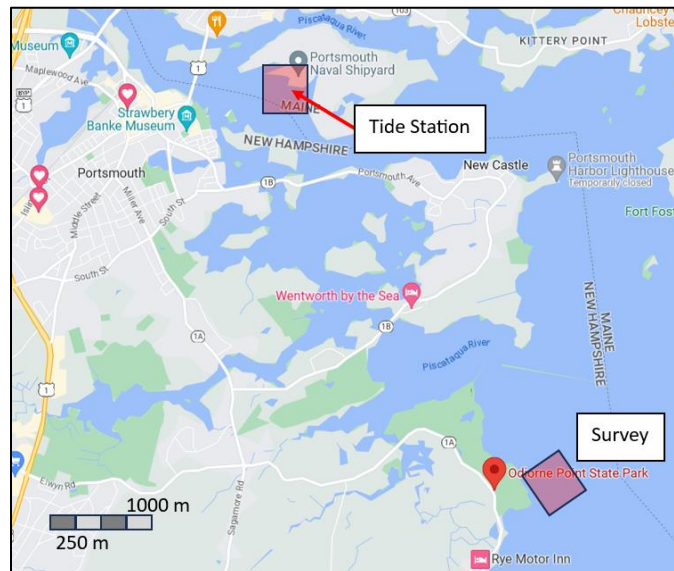


Figure 93 - Tide station and survey locations.

### 3.7.3. Gridding

Databases obtained from the previous step were gridded using the following logic:

- 1) The grid limits are defined by the maximum value of Eastings and Northings existing on the database.
- 2) A regularly-spaced Eastings and Northings matrix is created using a pre-set grid size in meters.
- 3) Each pair of E and N defines a node center. Then, for each node:
  - 3.1) The algorithm filters all depths within half-a-cell size from the node.
  - 3.2) The node depth is obtained using a weighted mean of the filtered depths, using the inverse distances from each depth to the node center as weights.
- 4) The script returns the Eastings array, the Northings array, and the E x N gridded depths matrix.

#### 3.7.4. Visualization tools

The depth grid computed by the gridding script can be plotted with the Python package matplotlib. A hill shade function adapted from Yan (2019) was included in the code to apply a 315° azimuth and 45° altitude sun illumination. Figure 94 illustrates the grid results, using a vertical exaggeration of 5 times:

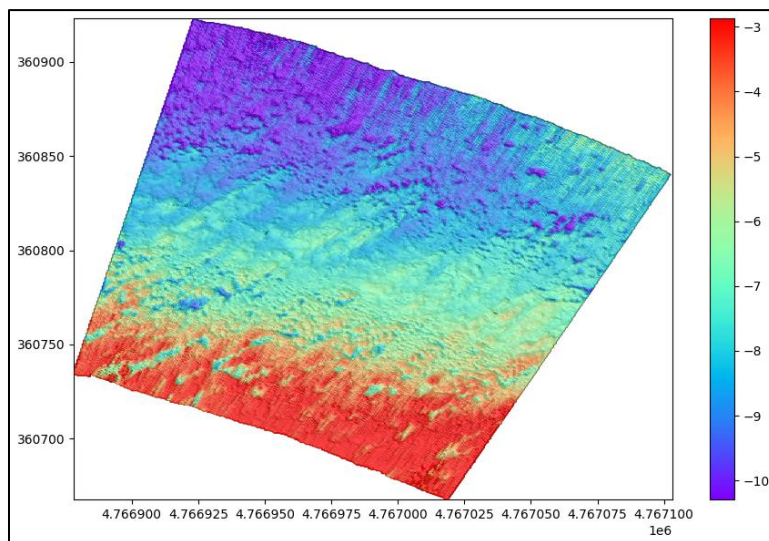


Figure 94 - Unfiltered grid from this study's beamforming bottom detection algorithm.

To achieve better visualization and use spatial tools, the grids were exported into ASCII files and imported into the commercial applications Qimera and Fledermaus. Due to the study time constraints, the software helped compare the algorithm results with the EM2040P reference dataset, for which no Python codes were implemented. Statistic tools, grid differences, and profile visualizations were also used when analyzing the datasets.

#### 3.7.5. The depth cross-check

To accomplish the third objective, comparing the 6205 proprietary bottom track dataset to the EM2040P counterpart, the depth cross-check tool from Qimera was applied to both grids and the results were analyzed and discussed in Chapter 4. The depth cross-check is a quality control tool often implemented in post-processing software. Although its implementation is not usually detailed in manuals, the test is generally done by spatially differentiating processed line depths to the nodes of a reference DTM. Each absolute difference is then compared to a maximum error budget, defined by the standard in use (e.g., S-44 Special Order), resulting in several rejected and accepted points. Finally, the percentage of accepted points relative to the total must be greater than the confidence interval defined in the standards, so the dataset is categorized. It is common to compute these statistics in swath angle intervals so that the user can observe the dataset quality in function of the beam angle. Figure 95 shows an example of QPS Qimera's cross-check tool.

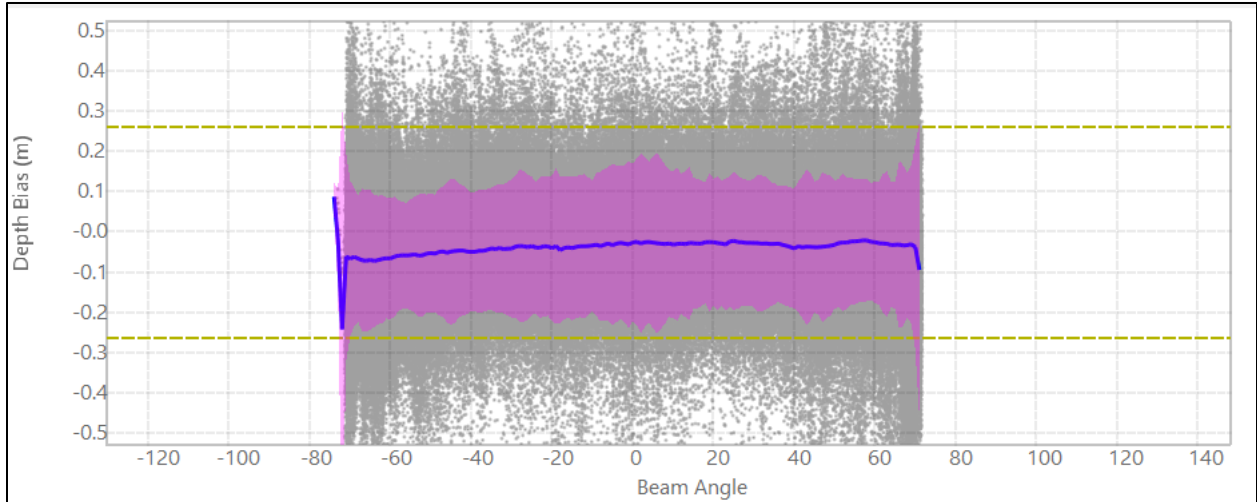


Figure 95 - Qimera's cross-check tool plot.

In yellow, Qimera plots the maximum error budget for the Special Order, calculated as defined in the S-44 6<sup>th</sup> Edition (IHO, 2022):

$$TVU = \sqrt{a^2 + (b \times d)^2} \quad (3.11)$$

Where  $\underline{a}$  and  $\underline{b}$  are constants defined in IHO (2022) for each survey order. Additionally, each gray point is the difference between a check line depth and the DTM node depth at the same location. The pink area and the blue line are statistics generated within incidence angle domain subsets. The blue line is the mean difference within each subset, while the pink envelope represents a  $1\sigma$  confidence interval around the mean (as described in QPS, 2023).

## CHAPTER 4: RESULTS

### 4.1. Beamforming performance

A series of comparisons between the following bottom detection algorithms were performed to assess the benefits of applying beamforming to the phase bottom detection: the half-wavelength average, Vernier solutions, and different stave combinations in beamforming.

#### 4.1.1. Split-arrays used

The first assessment of the developed code was how many combined elements would return the best model of the seafloor. This algorithm applied conventional phase beamforming to the set number of adjacent staves and included a window for each virtual stave in the phase averaging process. The ambiguous pairs were not used in this study to improve the depth variance, as this study didn't reach the phase unwrapping implementation for these subarrays. In the conditions described, Figure 96 below compares each beamforming configuration results:

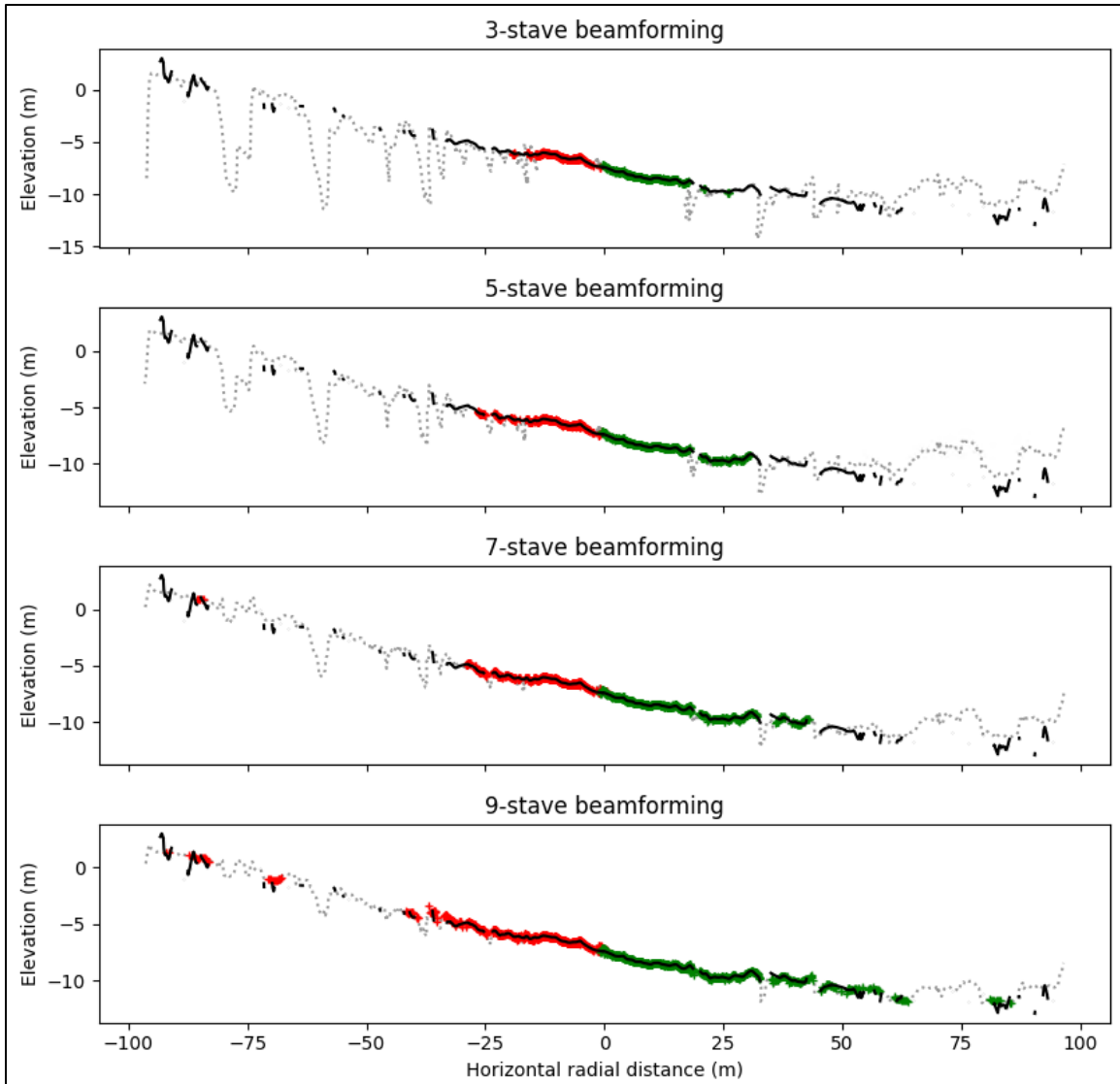


Figure 96 - 3, 5, 7, and 9-stave beamforming solutions. EdgeTech solutions in black. The algorithm rejected solutions in gray.

Using fewer staves to apply beamforming and make an average solution was not beneficial for the logic used in this algorithm. The fewer staves combined, the noisier the solution obtained, less agreement to the reference solution was achieved, and more data was rejected, meaning that the change significantly affects the quality factors. Besides, as no regression was used in this implementation, the benefit of less error in function fitting mentioned before is not applicable.

Proceeding the evaluation, the quality factors can also be used to assess the use of smaller subarrays:

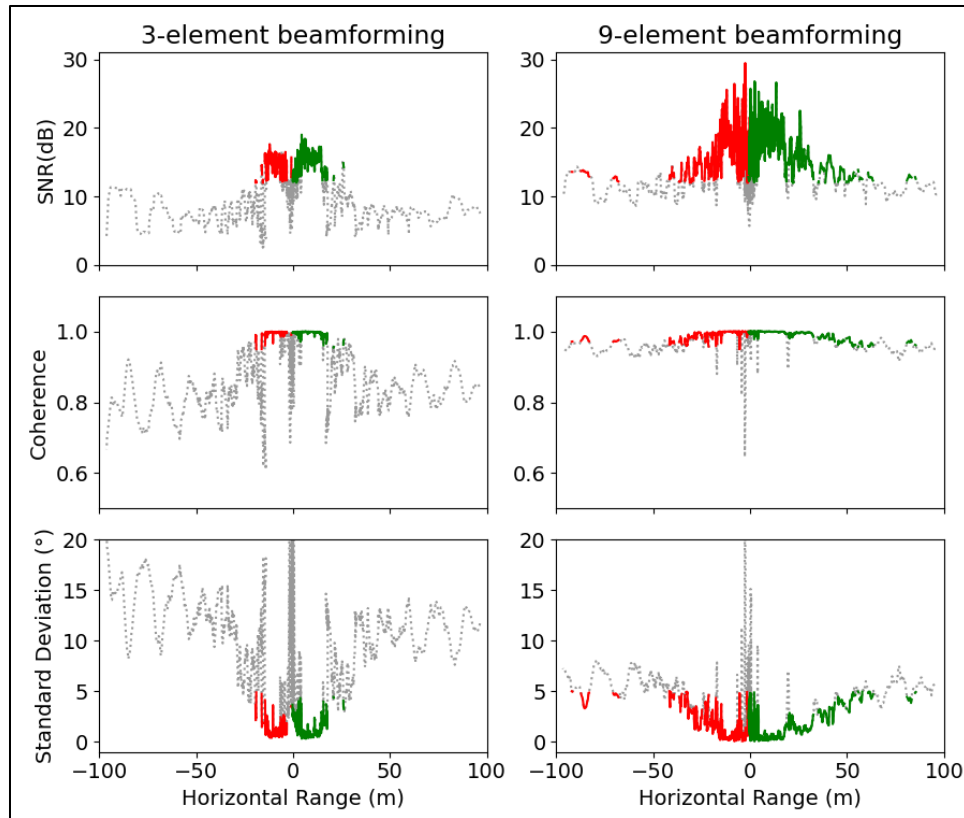
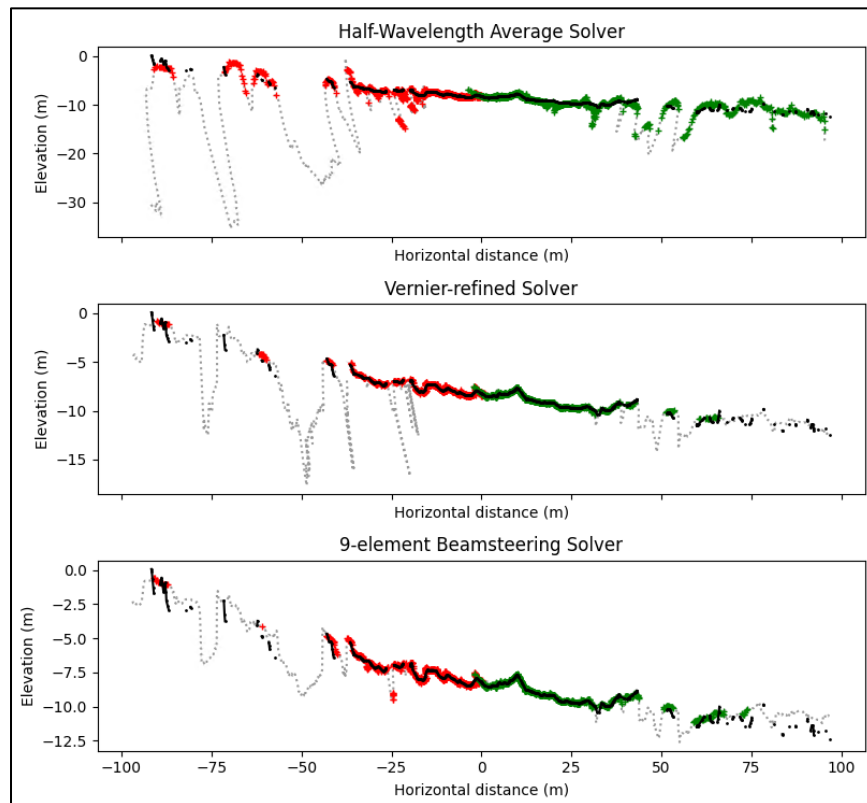


Figure 97 – 3 and 9-stave beamforming quality metrics. EdgeTech solutions in black. The algorithm rejected solutions in gray.

Comparing the parameters, the SNR in close range for the 9-element combination is about 10 dB greater than for the 3-element alternative. If maintained, the water column threshold may reject actual data in the nadir. Besides, there is a considerable loss of coherence from about  $60^\circ$  incidence angle on, which is the main factor rejecting far-range data, as the threshold in use for both is 0.95. The standard deviation behaves similarly to coherence, showing a noisier solution in the 3-element beamforming algorithm. Considering these aspects, the default configuration adopted in this study was the 9-element beamforming (two virtual staves).

#### 4.1.2. Beamforming vs. conventional depths

The way the theory is conceived, the expectations over the comparison between beamforming and conventional solutions are the difference between applying a spatial filter in the first method, while relying on a heavy averaging to dilute the unfiltered noise in the latter. Figure 98 shows a comparison between depth solutions from the same ping, achieved with the three algorithms being compared:



*Figure 98 - 2D depth solutions from different phase bottom detection algorithms. Gray: data rejected by the filter thresholds. Black: EdgeTech solutions.*

The three solutions are consistent with the EdgeTech solutions to a certain degree. Still, in terms of noise, the beam steering solver appears to have achieved a cleaner solution, followed by the Vernier solution, which had poorer results in shadowed areas, and last by the half-wavelength



average, that showed artifacts in the close range already, at about 20 m. Interestingly, the Vernier method agreed more in the edges of the swath, as it is not affected by the beam steering error, indicating that the EdgeTech solutions are averaging less uncorrelated noise in the far range. In any case, shadows and the far end of the swath do not usually bring trustable data, tending to be rejected, so Vernier and beam steering can achieve comparable filtered results. Besides, beam steering amplifies power in the far range, as fewer data was rejected compared to the other solutions. As for the close range, Figure 99 shows the detection of a 1-meter-high boulder by each algorithm at normal incidence for a group of pings. The PMBS' solutions were all integrated by this study's logic (including the manufacturer's), while the EM2040P dataset was integrated by Qimera and imported in Python.

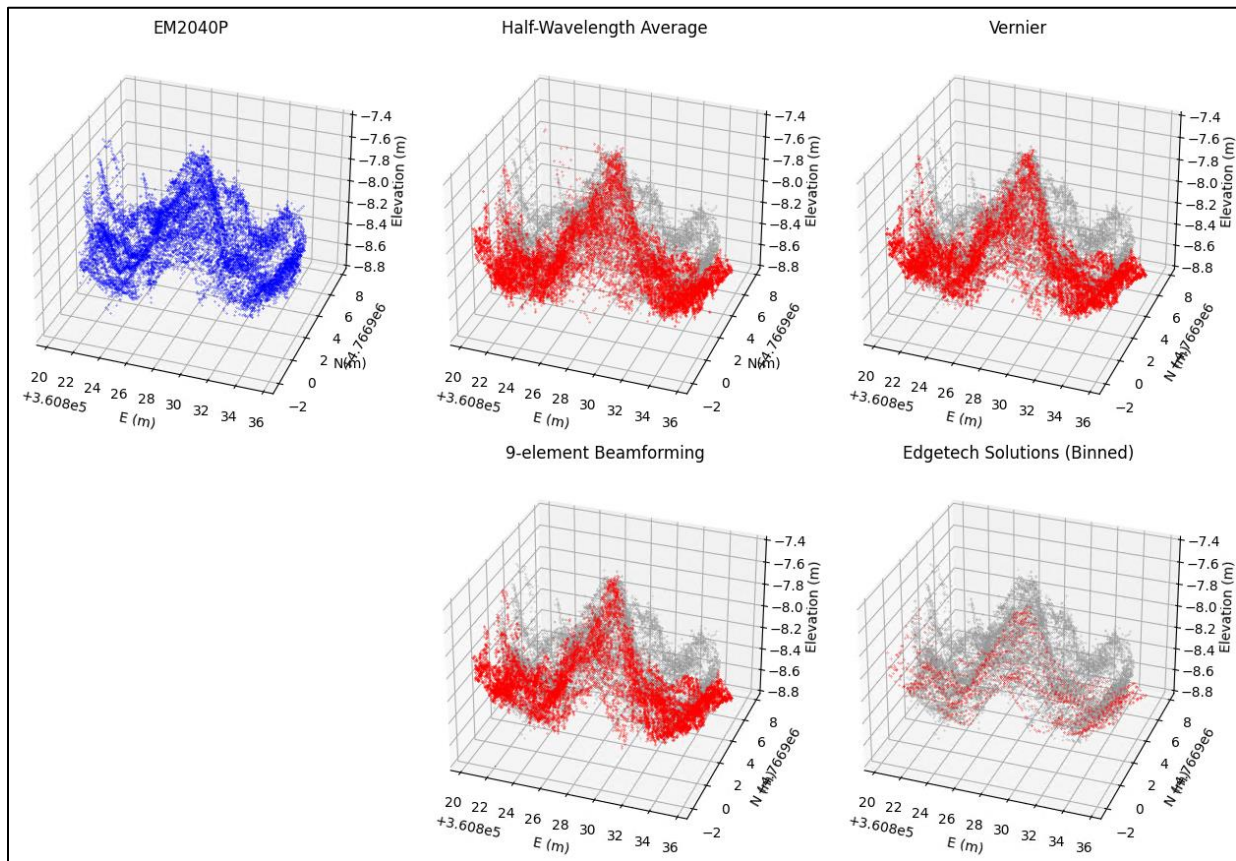
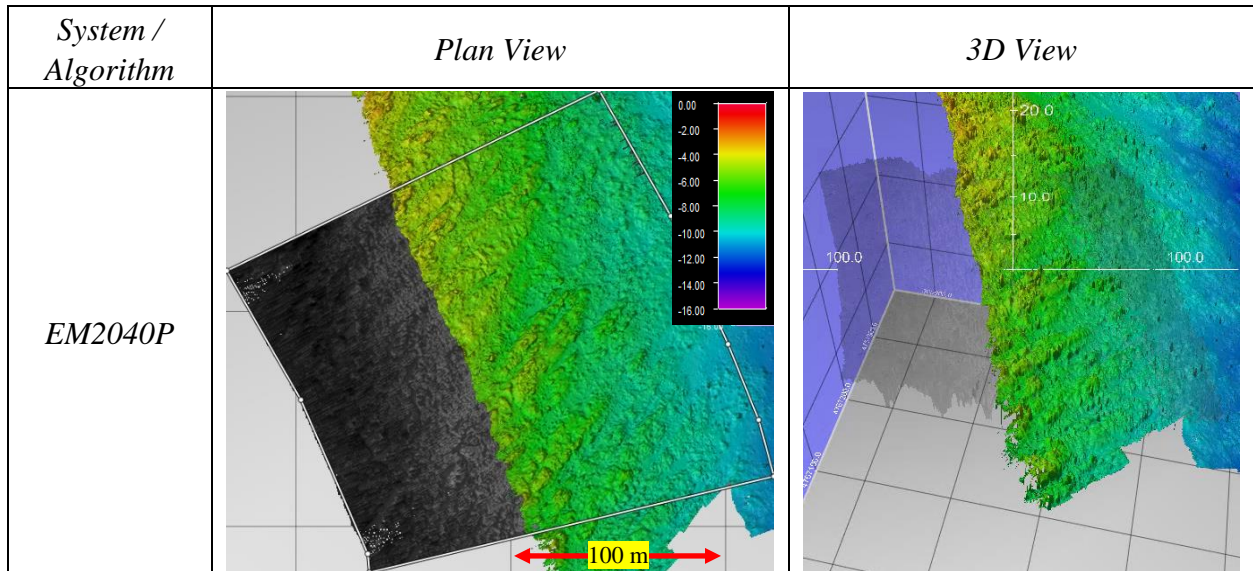
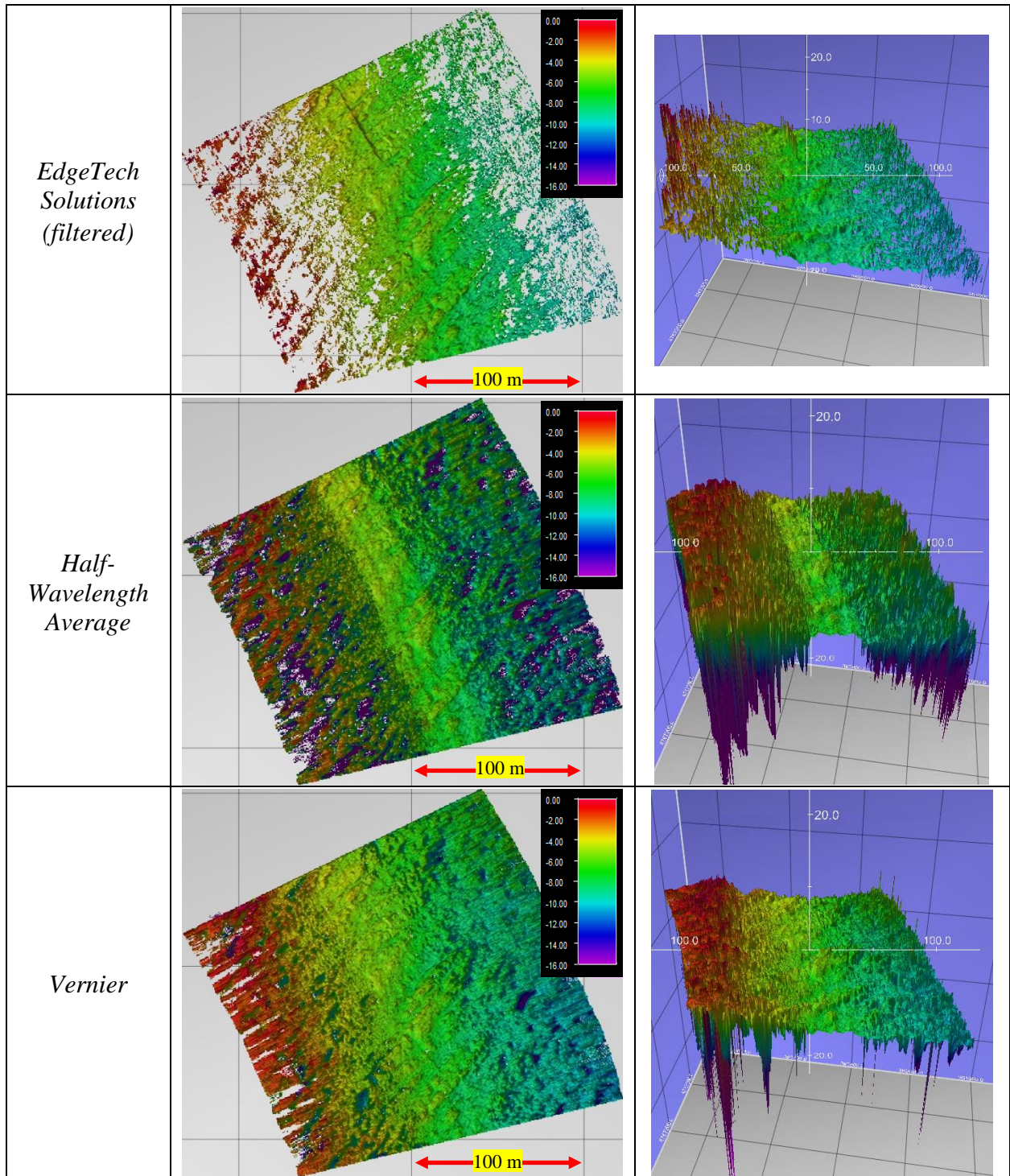


Figure 99 – 1-meter-high boulder at the nadir. Gray: EM2040P co-located soundings.

Analyzing Figure 99, it is possible to notice that the four algorithms depicted the boulder accordingly, though the EdgeTech solution underestimated the feature height by 18 cm, which may be caused by using a longer across-track window for the ensemble average. Regarding noise, more outliers are seen in the half-wavelength solution, followed by the Vernier and then, the beam steering depths, which seem to be the cleaner solutions between the in-house developed algorithms. The manufacturer detections are the ones that are less corrupted by noise, though the reason for that is not only the detection process, but also because it is already binned. EdgeTech does not provide raw (non-binned) solutions. Looking further into this comparison, 0.5-meter cell resolution DTMs from each algorithm are shown below. Depths were slightly filtered, just enough to reject water column and reverberation:







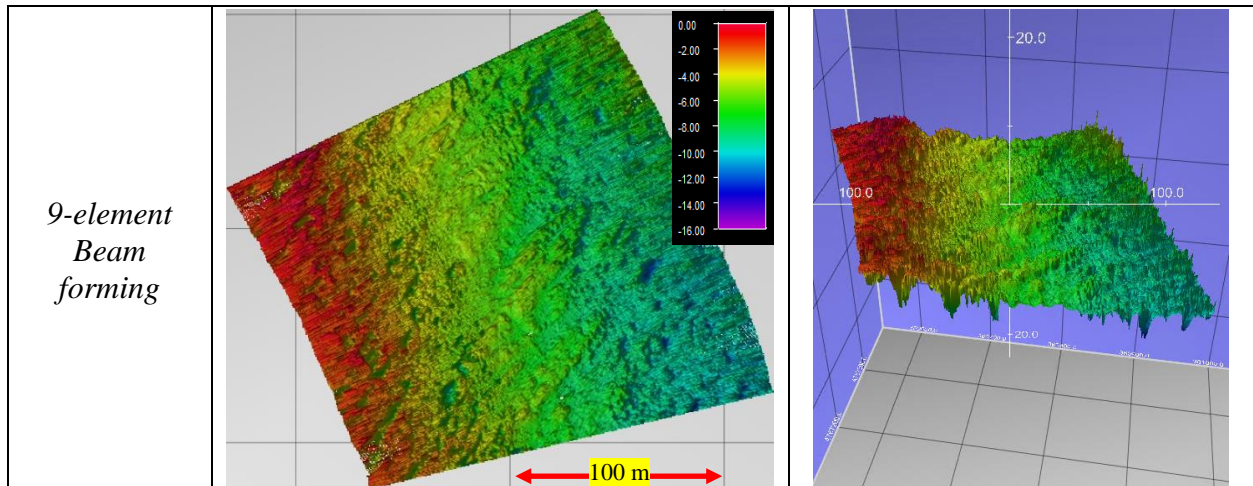
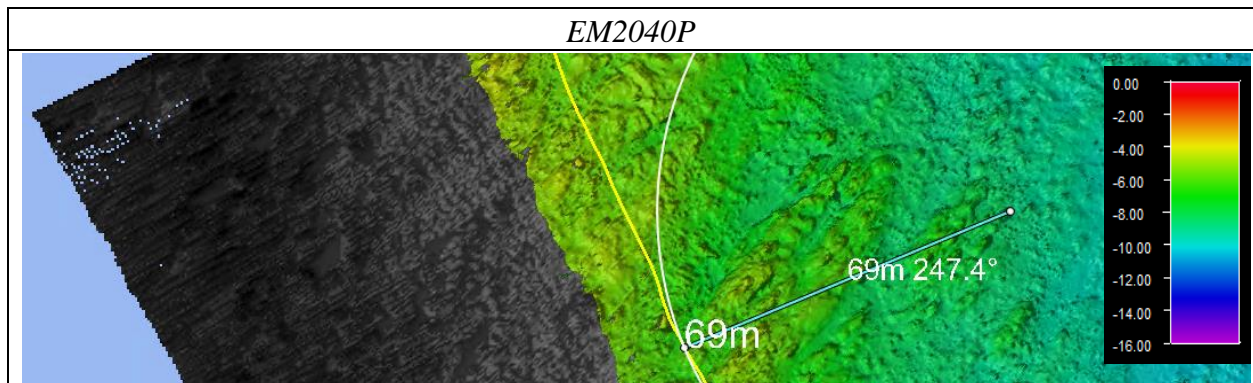


Figure 100 - Comparison between Half-wavelength, Vernier, and Beamforming DTMs.

The overview of the DTMs indicates that the Vernier and Beamforming algorithms had solutions in far-range where EdgeTech either rejected or could not compute a solution. However, the half-wavelength solver could only resolve the central subset of the DTM. Another point is that more outliers are seen in the Vernier solution than in beamforming, and even the slight filtering affected Vernier results in far-range, in the shallow side (red). To see how far the algorithms could detect morphology, a feature was chosen in the EM2040P grid 69 m offset from the 6205 line at about an  $83^\circ$  incidence angle. The EdgeTech solutions did not depict the feature, which was filtered automatically during their bottom detection process. Two of the in-house unfiltered results, however, could show the feature, as shown in Figure 101:



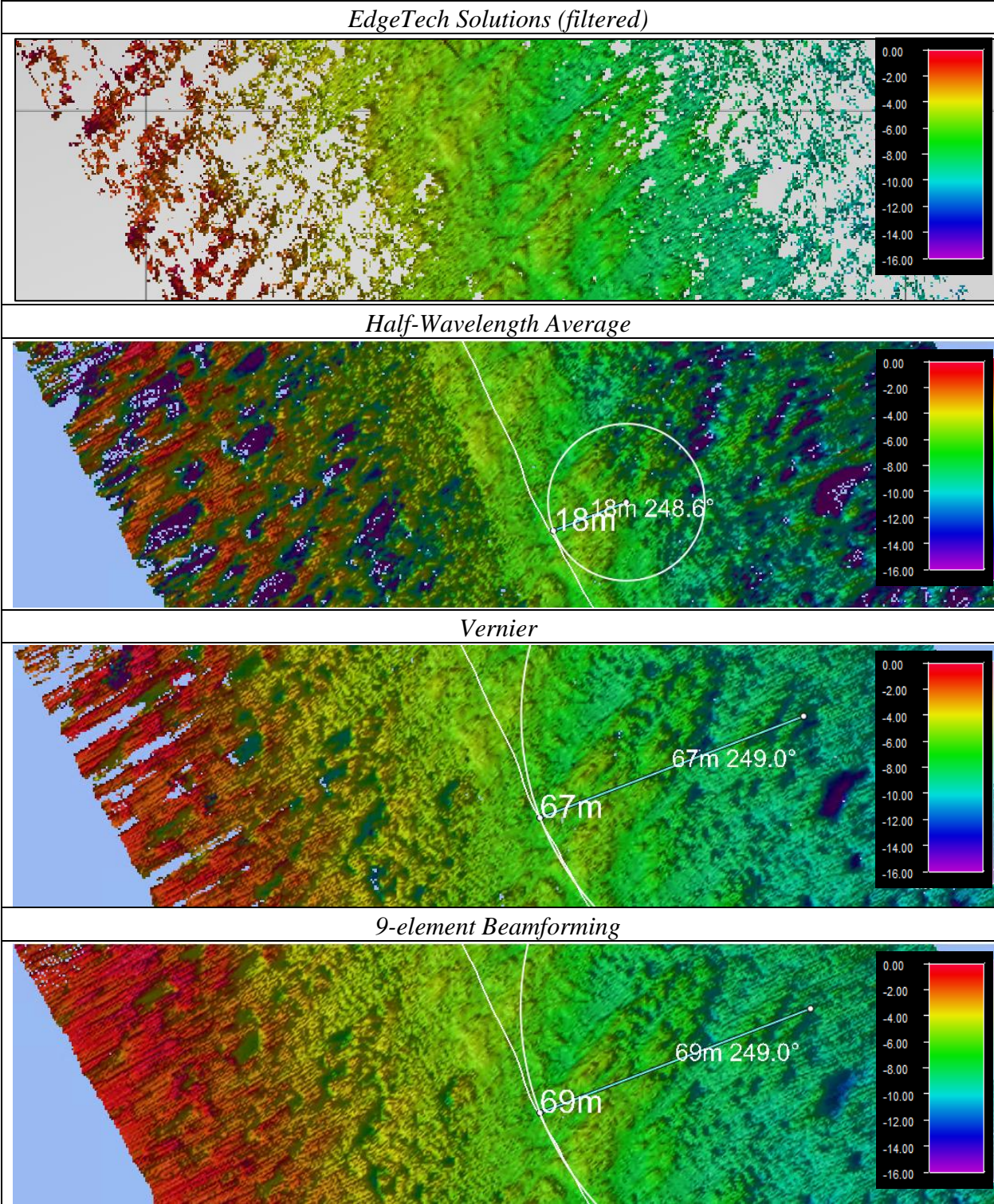


Figure 101 - Visual recognition of morphology.



Analyzing the half-wavelength average solution, there is a clear limit from where noise starts to corrupt the depth solutions heavily, in agreement with previous analyses. In this case, further than the 18-meter range ( $65.0^\circ$  at 8-meter depth), it is hard to distinguish morphology from the severely noisy solutions. This example corroborates the theory that described high variance for solutions derived directly from unambiguous differential phases.

Theoretically, more precise DOA estimation can be achieved by including ambiguous pairs in the averaging process. The Vernier solution shows the result of disambiguating and averaging all the nine possible element spacings for the 6205. A visual inspection of the Vernier-refined grid makes it possible to attest to a significant improvement in bottom detection. Morphology can now be distinguished up to about 67 meters or  $83^\circ$ , and much of the noisy terrain model in the mid and far-range was collapsed to a lesser-variance solution. However, even the slightest filter already rejected data from the edges of the swath on the port side, which were shallower and rougher in this case.

Looking now at the beamforming solutions, less noise is seen in the mid and far-range, depths at shadowed areas are more collapsed, and even applying a heavier coherence filter; no data was rejected in the far-range. This result leads us to believe that the spatial filter effect of beam steering is acting on the differential phase coherence, effectively attenuating multipath. Further analysis of that will be performed next. Morphology could be recognized at the same practical distance as Vernier at  $83^\circ$  incidence. As for the close range, a zoom-in was applied to an area of 40m x 20m centered at Lat.  $43^\circ 02' 32.14''$  N / Long.  $070^\circ 42' 31.36''$  W, to verify how the DTMs depict features at the nadir (Figure 102):

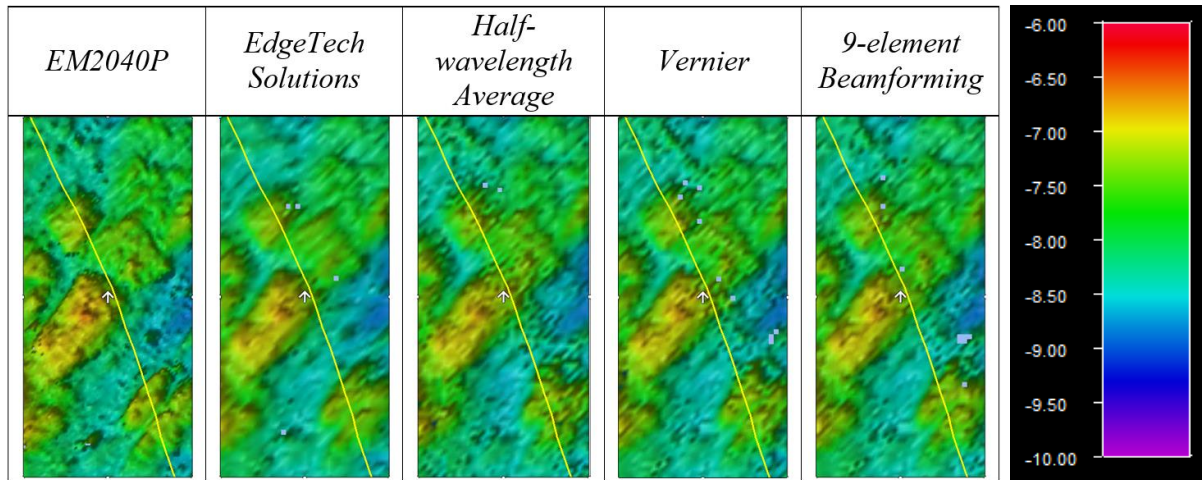


*Figure 102 - Nadir solutions for different phase bottom detection algorithms.*

Half-wavelength and Vernier aggregated more noise in normal incidence detection than beamforming, seen as black dots around the navigation line (in yellow). Some are still seen when compared to the EdgeTech solutions, which are cleaner, but more smeared than the others. This smearing may probably be an effect of using a larger averaging window than the one used in this study or a consequence of EdgeTech’s DOA estimation method, for instance, by averaging more subarrays and/or ambiguous pairs.

The presence of higher noise corruption in the conventional methods may result from treating all directions equally, where nadir interference exists. 9-element beamforming achieved better target detection at the nadir by successfully attenuating some of the mentioned interference, using thinner beams. Regarding holidays, all algorithms had some gap cells at the nadir, but the EdgeTech solution had fewer, potentially a secondary effect of using a larger window.

#### 4.1.3. SNR and phase coherence

Another way to analyze the algorithm’s performances is to examine how SNR and phase coherence respond to each method. The estimators used were the ones defined in section 2.9.

Figure 103 shows the effects of filters in elevation, and the SNR and coherence series for the Vernier and the 9-element beamforming algorithm.

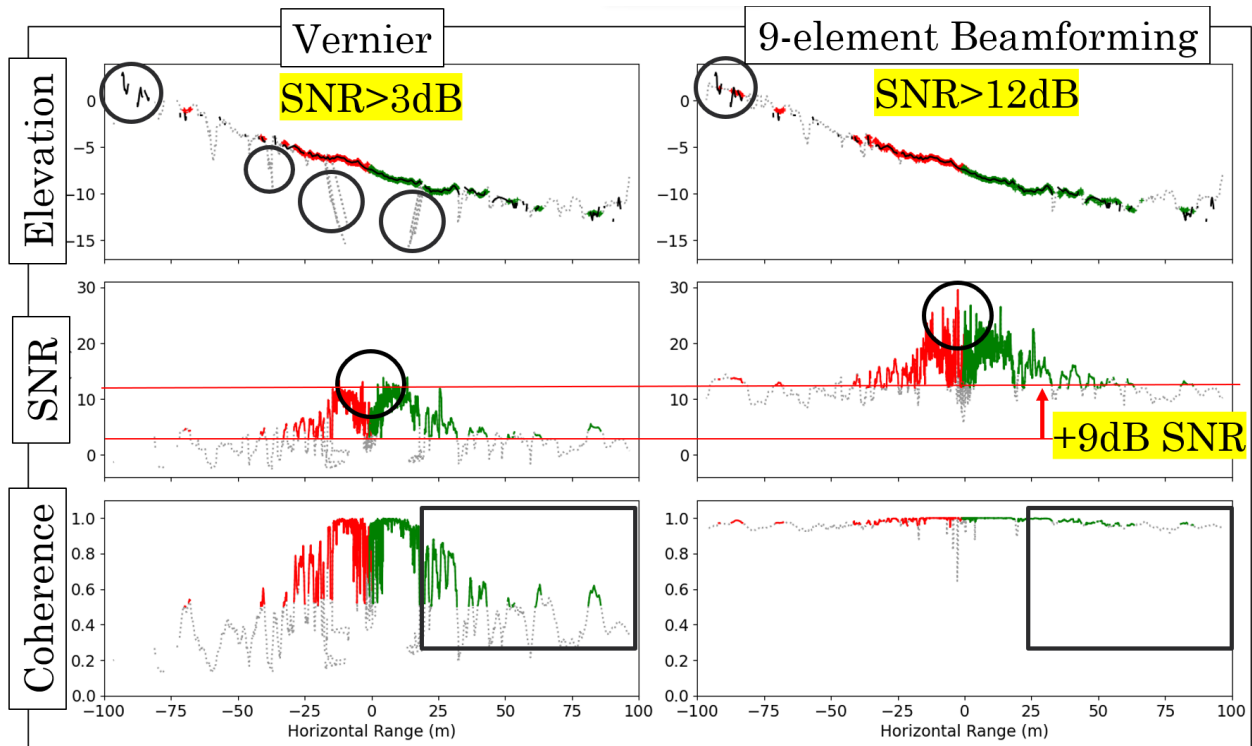


Figure 103 - SNR and coherence - Vernier vs. Beamforming.

In the elevation plots, the Vernier bottom detection had more outliers than the beamforming, and more of the far-range data was rejected using comparable SNR thresholds. Analyzing the SNR series, a mean level gain of 9 dB was observed when applying beamforming, compatible with the theoretical gain calculated in section 2.10.2. Not only that, but an additional increase of SNR in close-range indicates that some level of interference is being mitigated, as intended. A problem observed in the Vernier algorithm was defining a reasonable SNR threshold because the nadir levels were too close to far-range data, reducing the maximum range achieved by the filtered Vernier compared to the beamforming DTM.



Another significant consequence of beamforming can be seen in the coherence. Figure 103 shows that, for the beamforming solution, the differential phase coherence is always close to one, ranging from 0.90 to 1.00, meaning that the window phase vectors were always close to being perfectly aligned. Notwithstanding, the Vernier solver only maintains high coherence up to 60~70° incidence angle, from where it decays fast and heavily, because of treating all directions equally. From the point of view of differential phase coherence, beamforming can be considered a more stable solution than Vernier, as it successfully filters signals from unwanted directions instead of attempting to dilute them in averaging, as Vernier does.

#### 4.1.4. Comparison to the reference dataset

Considering the EM2040P solution as the truth, each algorithm can be evaluated on how much they agree with the reference. The previous analyses show that different trends could occur depending on the incidence angle, so, for this study, the DTMs were filtered by angle intervals of 10° and then compared to the reference by running a grid difference and computing statistics. A maximum range of [0, 15] meters was defined to avoid gross outliers in the computation, that would be manually rejected in the usual processing flux. Further, the mean, the standard deviation (95% confidence) and the resulting confidence interval were used to evaluate similarity. Figure 104 presents the statistics obtained for Line 4, P.L. 3.7 ms, 100-meter maximum range.

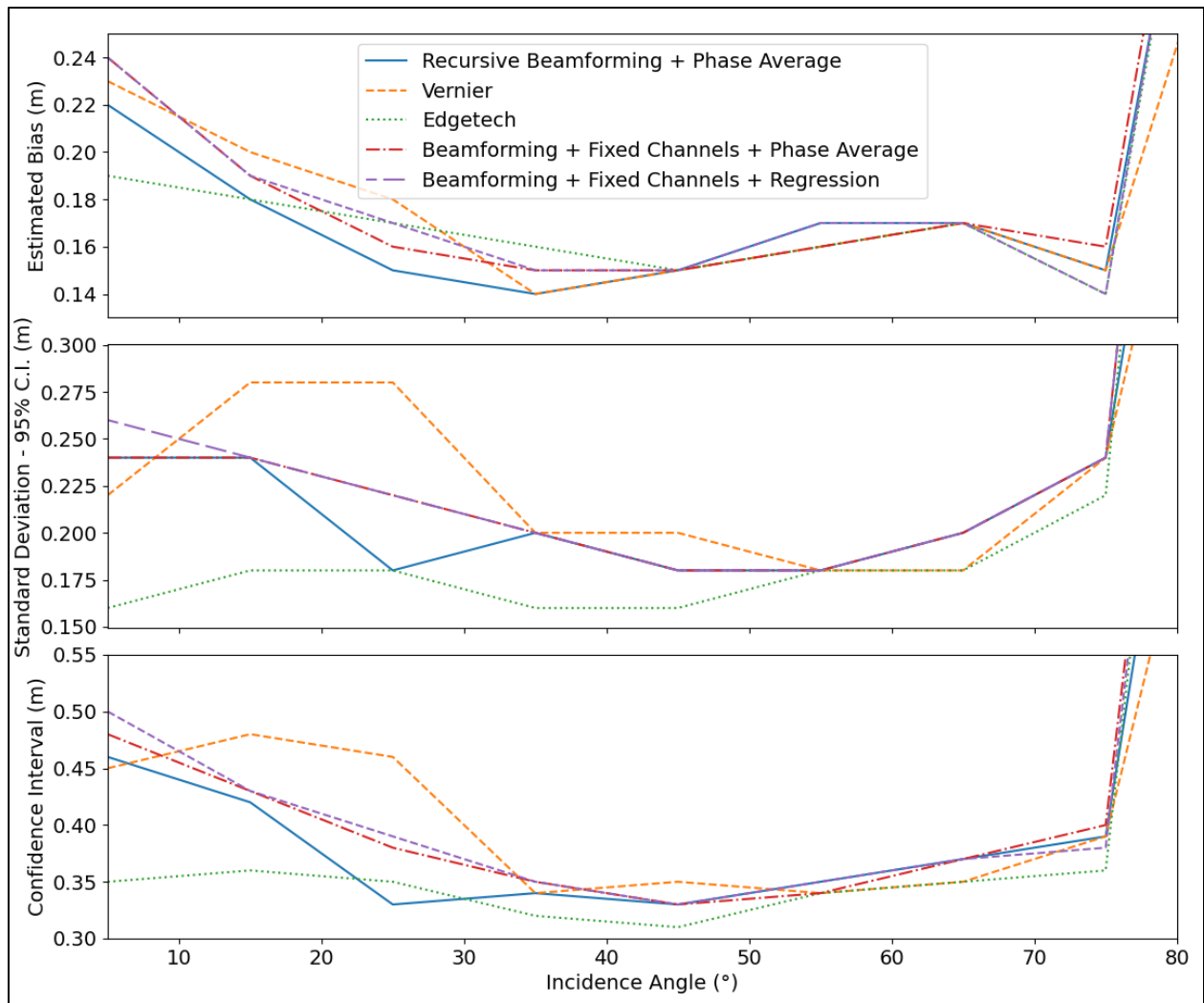


Figure 104 - Algorithms' grid difference statistics.

In this analysis, it is important to mention that the estimated bias between the algorithms and the reference dataset is not only due to the bathymetry processing, but also to inaccuracy in the water level corrections (which were not collected at the exact place where the survey occurred), and the draft measurement. Nonetheless, it is still possible to affirm that the manufacturer's results had a larger mean difference to the reference grid than the in-house algorithms from 10° incidence to 50° incidence, which ultimately resulted in a grid about 16 cm deeper than the EM2040P, which is another clue that EdgeTech is using a larger window than the in-house algorithms. Beam steering

solutions were less biased than Vernier's up to the interval  $30^\circ$  to  $40^\circ$ , and then had about the same level of bias.

In terms of uncertainty, EdgeTech solutions consistently had the lowest value of standard deviation up to the  $70^\circ$ - $80^\circ$  interval, from where it diverged more than the other algorithms. That may be explained by a larger sample window being averaged, or a superior array processing technique. In turn, beam steering solutions had lower uncertainty up to  $50^\circ$ - $60^\circ$ , and then Vernier resulted in lower values (probably because it is not affected by the steering error in far range).

To analyze the combined effect of bias and uncertainty, a third plot for the resultant confidence interval was conceived. As seen, the manufacturer's solution is the one that agrees best to the reference dataset, except for the last interval ( $80^\circ$  to  $90^\circ$ ), where all algorithms diverge anyway. Additionally, beam steering solutions have better agreement to the reference than Vernier up to  $60^\circ$  incidence, from where the latter seems to drift less.

Finally, among the different beamforming algorithms, the use of phase averaging or regression (red vs. purple) didn't imply a reasonable difference in detection (at least, by using the same average window). As for recursive vs. fixed channels (blue vs. red/purple), the former showed lower values of bias and standard deviation up to mid-range ( $40^\circ$ ), from where it had similar results to the latter.

#### 4.1.5. Processing time

Although the Vernier and beamforming grids look similar, the latter is much more efficient than the first. While the conventional phase beam steering computations are mainly two weighted sums of a complex time series window (for the 9-element version), the Vernier solver processes an average phase for each of the nine possible combinations of stave spacing, averaging thirty

repetitions of the complex time series window, before proceeding the phase disambiguation, for which a search script is then used eight times to reach a final solution. As a result, the Vernier solver developed in this study was about seven times slower than the beamforming algorithm.

## **4.2. EdgeTech solutions vs. EM2040P**

The previous section showed that beamforming improved SNR, especially for nadir and far-range, and filtered phase vectors coming from multipath. In the current section, the manufacturer's solutions will be compared to a multibeam reference dataset that provides accurate and high-resolution DTMs, to assess the quality of 6205 datasets in shallow waters. Four standard survey criteria were used to evaluate this: mean depth cross-check, target detection, density, and system efficiency.

### **4.2.1. Mean depth cross-check**

The survey area had a mean depth of about ten meters, so the transducers were at an approximate altitude of eight meters. Thus, this test considered a 6205 coverage of about  $85.4^\circ$  for each side. The four EM2040P eastern lines were characterized by a rougher seafloor, while the others had a smooth, gently sloped seafloor. Aware that slight positioning or integration differences may cause false vertical mismatches in rough areas, this study purposely crossed the whole datasets, considering that most hydrographic offices would not restrict TVU evaluation to flat parts. At the same time, this choice is expected to provide more conservative results in terms of the safety of navigation.

Conventionally, the end product (the 6205 grid) would be assessed against check lines to perform the survey quality control, verifying how much the DTM would represent an independent

set of raw lines. However, the intention of this test was to check the quality of the 6205 raw soundings, not its averaged grid, so the 6205 lines, P.L. 0.25 ms, maximum range 100 m, were tested against the EM2040P DTM using Qimera’s cross-check tool, achieving the S-44 Order 1.

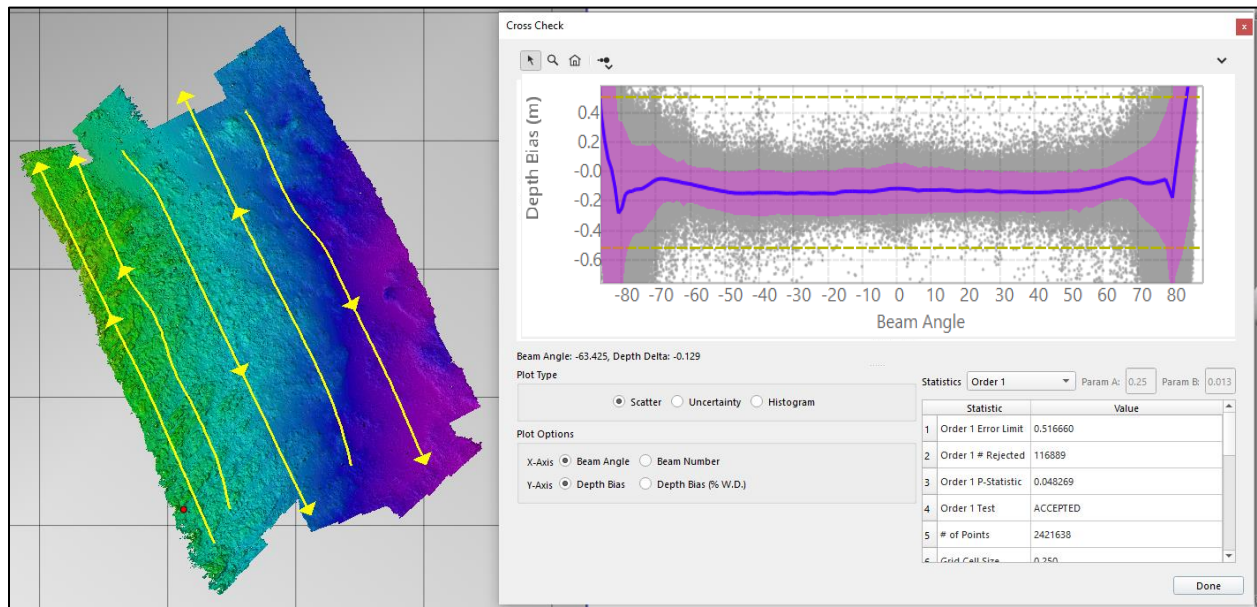


Figure 105 - 6205 raw lines (yellow) cross-checked with the EM2040P reference dataset.

Although relevant for nautical charting, the S-44 limits may be considered lax in shallow water for modern systems, as most of the vertical errors do not come from time-and-angle estimation, but rather from draft, water level corrections, and sometimes refraction. That said, a better qualification may be achieved by looking at the cross-check standard deviation, which is less influenced by those long-term variations. Besides, the variance of PMBSs’ depths is highly dependent on the incidence angle, so the overall qualification as Order 1 may not be applicable to the edges of the swath. Therefore, a more precise analysis may be performed in the uncertainty vs. incidence angle plot (Figure 106):

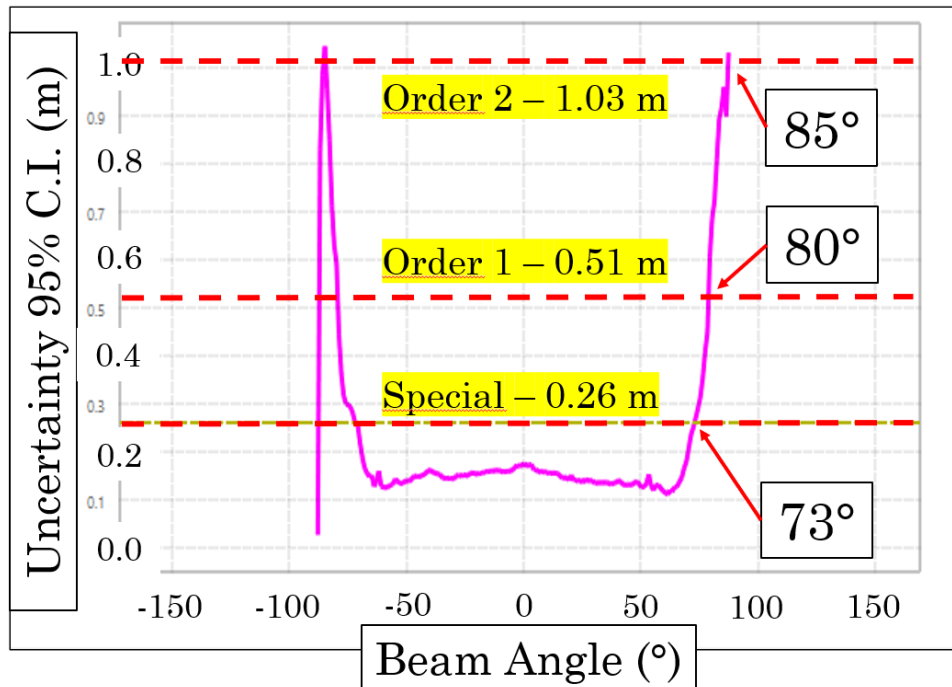


Figure 106 - 6205 raw line uncertainty (95% confidence) vs. beam angle.

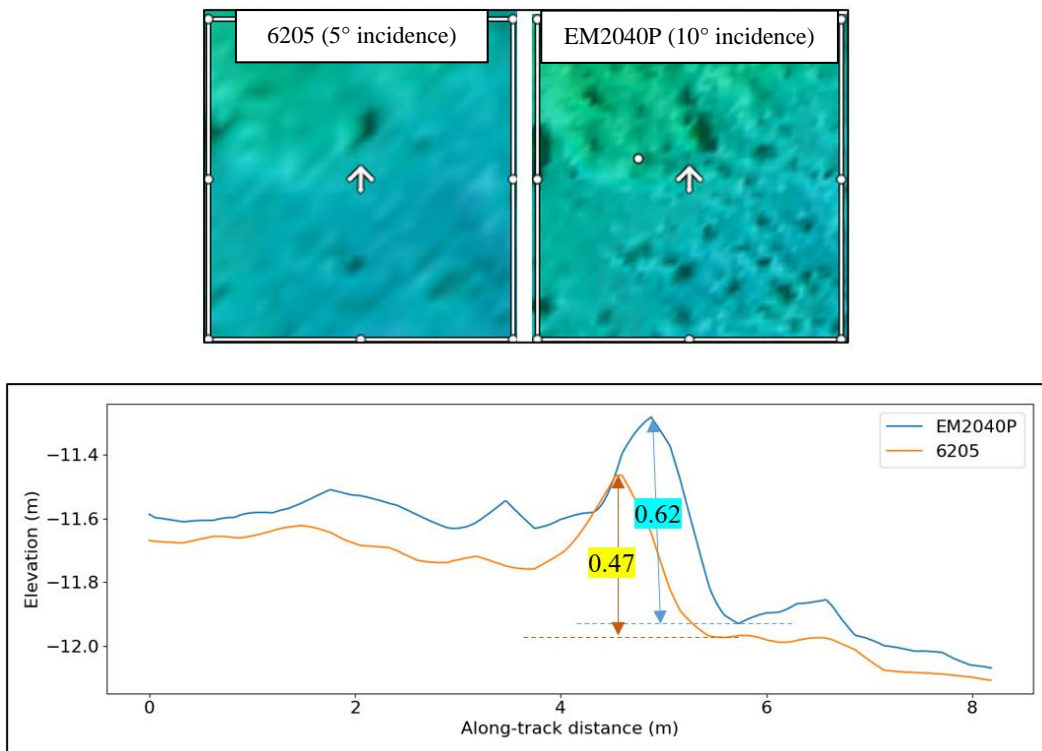
Figure 106 shows that the vertical uncertainty of 6205 raw data (95% confidence), when compared to the EM2040P dataset, was slightly higher on the nadir (around 0.17 m), gently fell to 0.13 m at 65° and abruptly rose to one meter until the end of the swath at 85°. This uncertainty curve, obtained exclusively with data, is highly correspondent to the uncertainty model developed in section 3.6.3, starting its divergence at the same incidence angle (65°). However, the EdgeTech processing method obtained considerably lower uncertainty values after 65°, which may be consequence of either a more advanced processing technique or a heavier averaging filter being applied.

Considering the clear dependence between the depth uncertainty and the incidence angle, better quality DTMs may be obtained filtering the maximum coverage. In this case, the standard deviation limit for Special Order was crossed at 73°, for Order 1 at 80°, and Order 2 at 85°. Therefore, filtering the 6205 lines by angle, and rejecting data over 73°, made a new cross-check achieve Special Order.

#### 4.2.2. Target detection

A 0.5-meter grid was made with Line 2, an 8-meter altitude line, with a maximum range of 50 meters and compared to the closest EM2040P single line grid (Line 7, at about a 5-meter lateral offset). The mean difference between both grids were compensated in the EdgeTech grid, yielding a +0.15m vertical offset, so that the target detection analysis would be less affected by the 6205 estimated bias. Then, common small objects (of about 1-meter horizontal size) were examined in the 6205 grid at close, mid, and far-range, and compared to the EM2040P detection through an along-track profile to compare its detection by a sequence of pings. The 6205 lines were run at 3.5 knots, while the EM2040P lines were run at 5.1 knots. Meaningful examples were listed as follows.

#### Case 1 – Close-range, small target at Lat 43-02-34.60N / Long 70-42-26.79W



Small objects close to the nadir were successfully detected by the 6205, but some target heights were underestimated, the difference ranging from 0 to 30 cm. Figure 107 is an example of object one meter far from the nadir, having a height detection of 15 cm lower than its EM2040P counterpart.

**Case 2 – Mid-range, small target at Lat 43-02-33.94N / Long 70-42-25.52W**

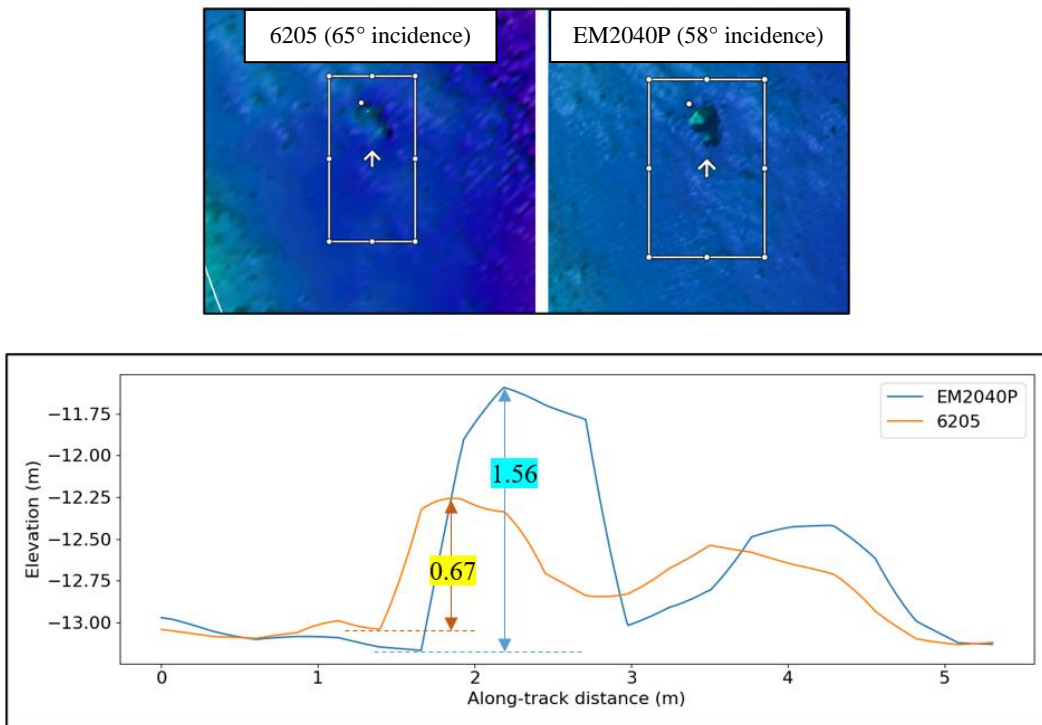


*Figure 108 - Case 2 - Target detection at mid-range.*

Comparing both grids at mid-range, all significant objects detected by the EM2040P were also detected by the 6205, but a more significant height underestimation was observed in some targets. In the case shown by Figure 108, the 6205 detection of a well-defined object twenty meters from the nadir had a height difference of 89 cm compared to the EM2040P detection.



**Case 3 – Far-range, small target at Lat 43-02-33.34N / Long 70-42-24.57W**

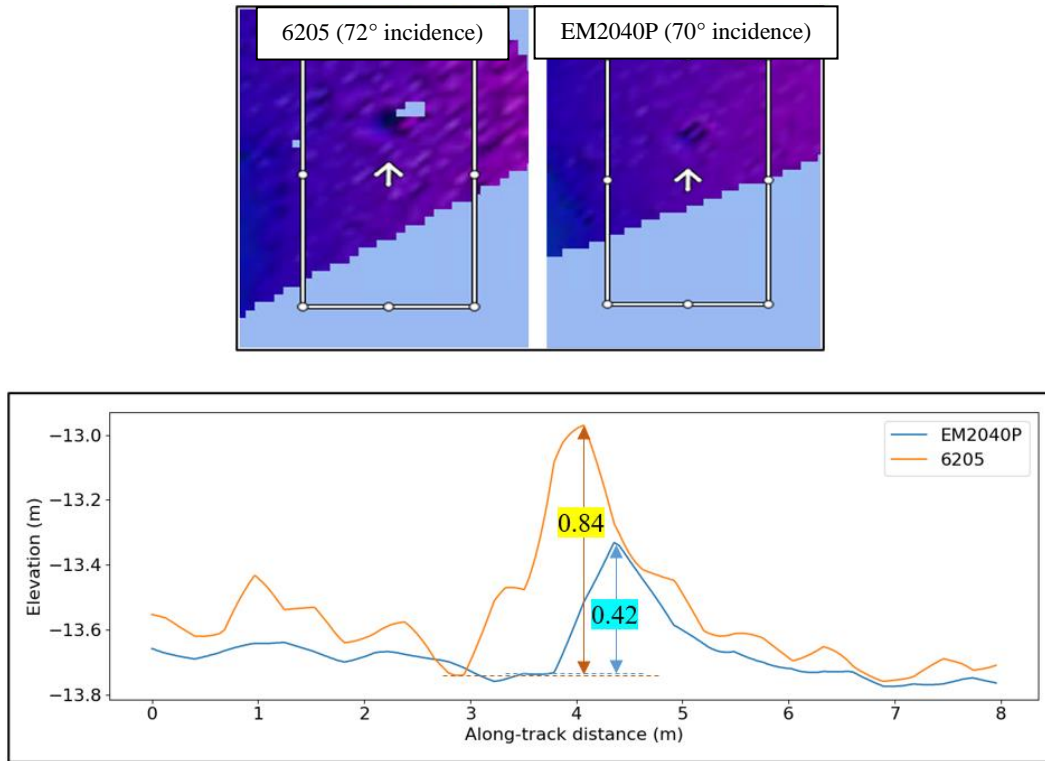


*Figure 109 - Case 3 - Target detection at far range.*

Small objects could be distinguished in far-range up to about thirty-three meters ( $76^\circ$  incidence angle). At further ranges, the 6205 depth variance made it exceedingly difficult to differentiate targets from the noise. Regarding the height estimation, the 6205 either presented comparable results to the EM2040P or now overestimated target heights, as shown by Figure 109, where the height difference was 0.42 m. Given that MBES are known to underestimate heights in very low grazing angles, it is possible that the 6205 may have been capable of providing a height estimation with the same accuracy or better than the EM2040P.

Analyzing the cases above, the EdgeTech 6205 was comparable to the EM2040P in detecting 1-meter targets at a 10-meter depth, even at far range, up to about  $76^\circ$  incidence angle. However, the 6205 systematically underestimated small targets' heights in close and mid-range (about one meter long and 0.5 to 1.5 meter high, at 8 meters altitude). Causes for the smearing may

include the averaging processes used to reduce the depth variance, such as the size of the time window and the binning, which affects the targets' boundaries and penalize more small targets in the across-track dimension. Pimentel (2018) also mentioned difference in feature boundaries in tests comparing an EM2040 to a Kongsberg Geoswath PMBS. The grid difference between the EM2040P and the 6205 datasets, with 100% overlap, shows that most differences do happen on targets' boundaries. Slight differences in positioning or integration are also reflected in grid differences, but such a mismatching would create symmetrical differences in the features' opposite boundaries, while what is observed in the grid differences is basically a positive difference covering small rocks completely.

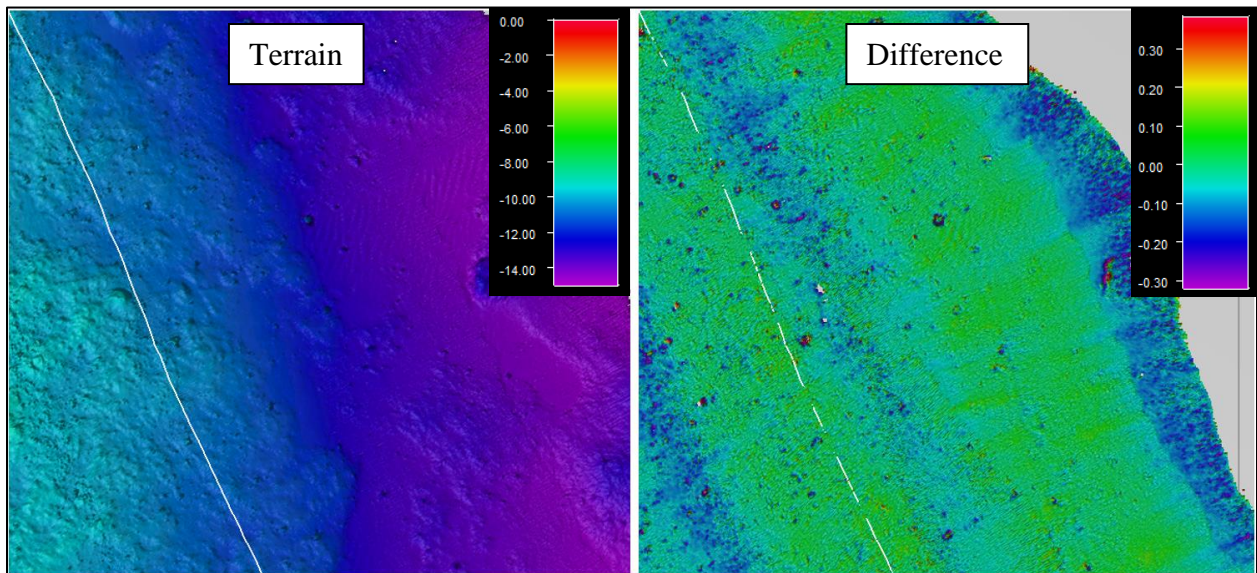


*Figure 110 - Feature boundaries in the EM2040P-6205 grid difference.*

Although the 6205 grid statistics met the S-44 TVU limits for Special Order, from a safety-of-navigation point of view, targets are what navigators are concerned about, and the differences in minimum depth observed in the cases above are significant when compared to the TVU limits.

### 4.2.3. Density

To evaluate density, DTMs for each system were created using lines at a 10-meter altitude, non-overlapped, with 0.25-meter cell resolution, shown in Figure 111 and Figure 112. The EM2040P line used to this assessment had about a 10-meter lateral offset from the 6205 line. The 6205 grid used the dataset run with a 50-meter maximum range to assess the system in a condition where the ping rate would only be limited to collect usable data.

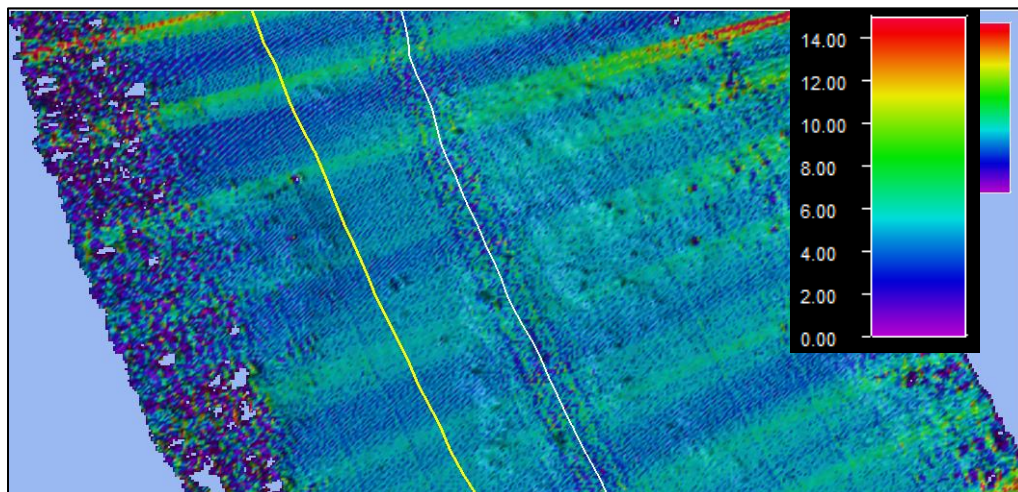


*Figure 111 - 6205 density layer (soundings/node) at 10-meter altitude. Yellow: EM2040P navigation. White: 6205 navigation.*

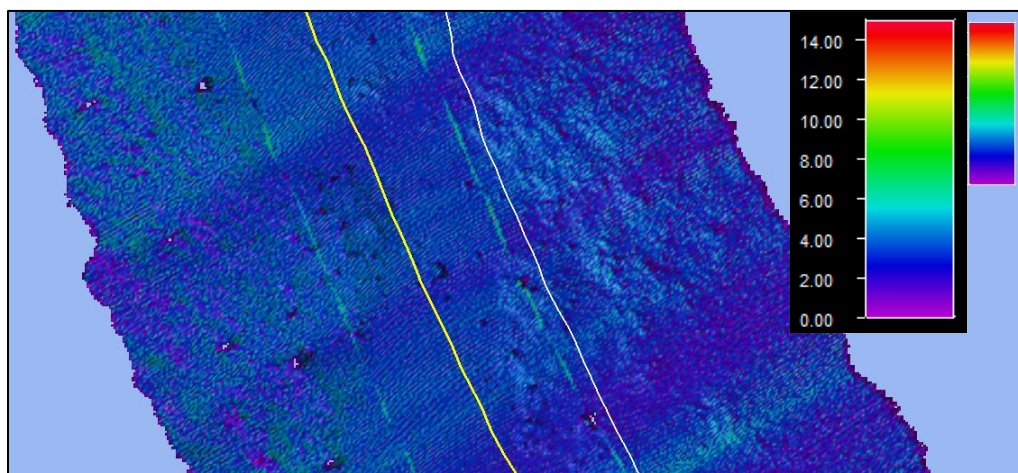


*Figure 112 – EM2040P density layer (soundings/node) at 10-meter altitude. Yellow: EM2040P navigation. White: 6205 navigation.*

The EM2040P grid shows a more equally distributed density, thanks to the system's attitude compensation in real-time; the 6205 only enjoys inherent roll stabilization (as the range is controlled by the receiver listening time only). The latter's sounding density is affected by yaw and pitch: when the heading changes, soundings get denser inwards and sparser outwards, while pitch makes the whole swath oscillate in density from one ping to the next.

To properly compare the systems' densities, it is vital to consider that PMBSs can deliver a much higher sounding density across-track than MBES systems, which may mislead a density comparison realized directly from square cells, so a more precise evaluation is obtained by comparing each dimension separately. It is also important to recall that the density in each dimension is controlled by different factors. First, the across-track distance is defined by the system mode (equidistant or equiangular) and number of beams (or bins, in PMBSs). The EM2040P was set to have 400 soundings per ping across-track, while the 6205 has 800 bins. Regarding the along-track density, it is mainly controlled by the survey speed, the number of simultaneous swaths (two for the EM2040P and one for the 6205) and the system ping rate, the latter being reduced as the maximum slant range is wider. Figure 113 was obtained by plotting the line integrated soundings in Fledermaus:

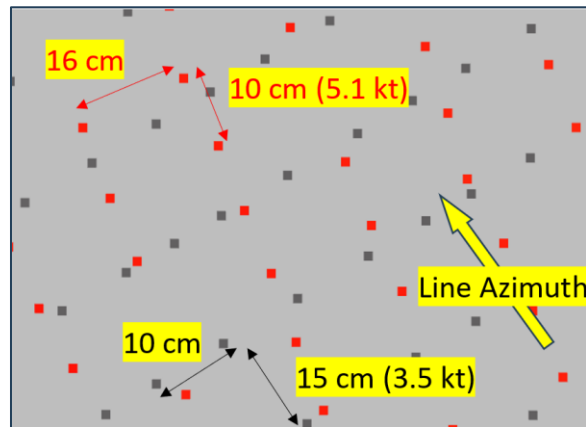


Figure 113 - Sounding Density - 6205 (gray) vs. EM2040P (red).

As both systems were set to equidistant mode, and each maintained a fixed ping rate, the across and along-track distances between soundings were approximately constant. The survey speeds were different though, thus needing an along-track normalization prior to the comparison (a 4-knot speed was used as reference, which is a usual survey speed for the 6205). The distances shown in Figure 113 were obtained by the mean of 10 samples, and are summarized per unit distance in Table 13:

*Table 13 - Density - EM2040P vs. 6205.*

<b>Soundings/meter</b>	<b>6205</b>	<b>EM2040P</b>
Across-track	10.00	6.25
Along-track*	5.90	12.7

*\* Normalized for a 4-knot speed.*

Table 13 shows that while the 6205 achieved less than half the EM2040P along-track sounding density, as expected due to having only one swath and a wider angular sector, it still was able to obtain more than the 3 hits per meter minimum (as written into most Special Order target detection interpretations). Therefore, the mean density is not the 6205 limiting factor to reproduce targets compared to the EM2040P. The loss of target definition, then, may be due to target smearing through averaging. Although in low noise environment, phase angular resolution is theoretically as fine as the sampling interval permits, the need for averaging (windowing and binning) ends up reducing that achievable resolution in the across-track direction.

The 6205 density at normal incidence:

An important discussion in this section is the density at the normal incidence, which was claimed to be constant throughout the swath by the manufacturer, notably a positive departure from other PMBS systems that suffer from gaps at the nadir. In the 6205 grid, up to 15° incidence,



while the data density never suffers complete dropout, it is possible to see significant fluctuations in density. The profile below is an across-track sounding density profile for a 0.5-m grid. The oscillation in the normal incidence is noticeably evident. However, the mean density across the swath was indeed kept stable.

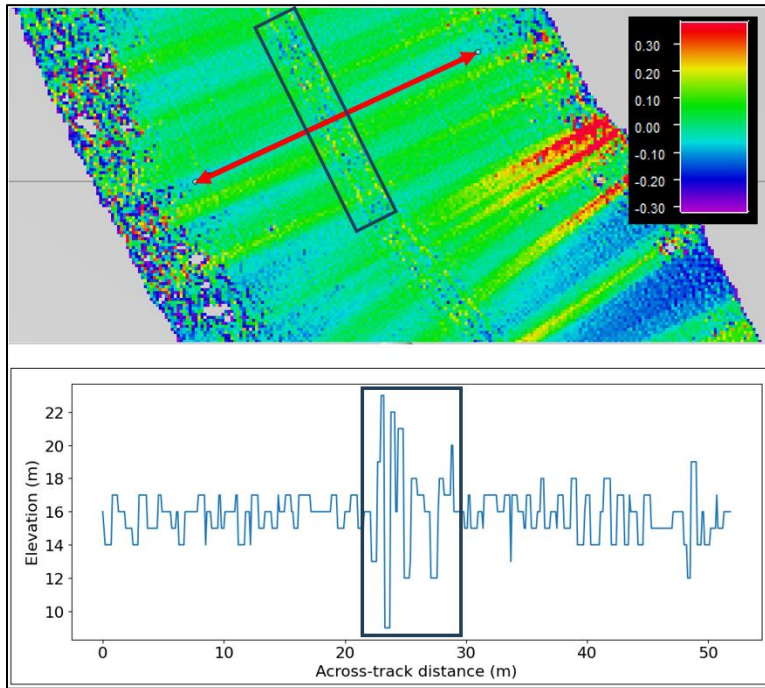


*Figure 114 - 6205 across-track density profile.*

To assess the impact of the density oscillation at the nadir, a weighted-average grid with 0.25-meter cell resolution was made for Line 2, range 50-m, P.L. 0.25 ms. (Figure 115). In this grid, it's possible to see that the normal incidence region (up to 15°) is notably noisier and more smeared than mid-range, reflecting either these oscillations in density or a more penalizing influence of window across-track averaging at that location. Despite this increase in noise, this smearing didn't hinder the visual recognition of 1-meter features at the nadir, and the noise can be drastically reduced by applying a CUBE gridder.

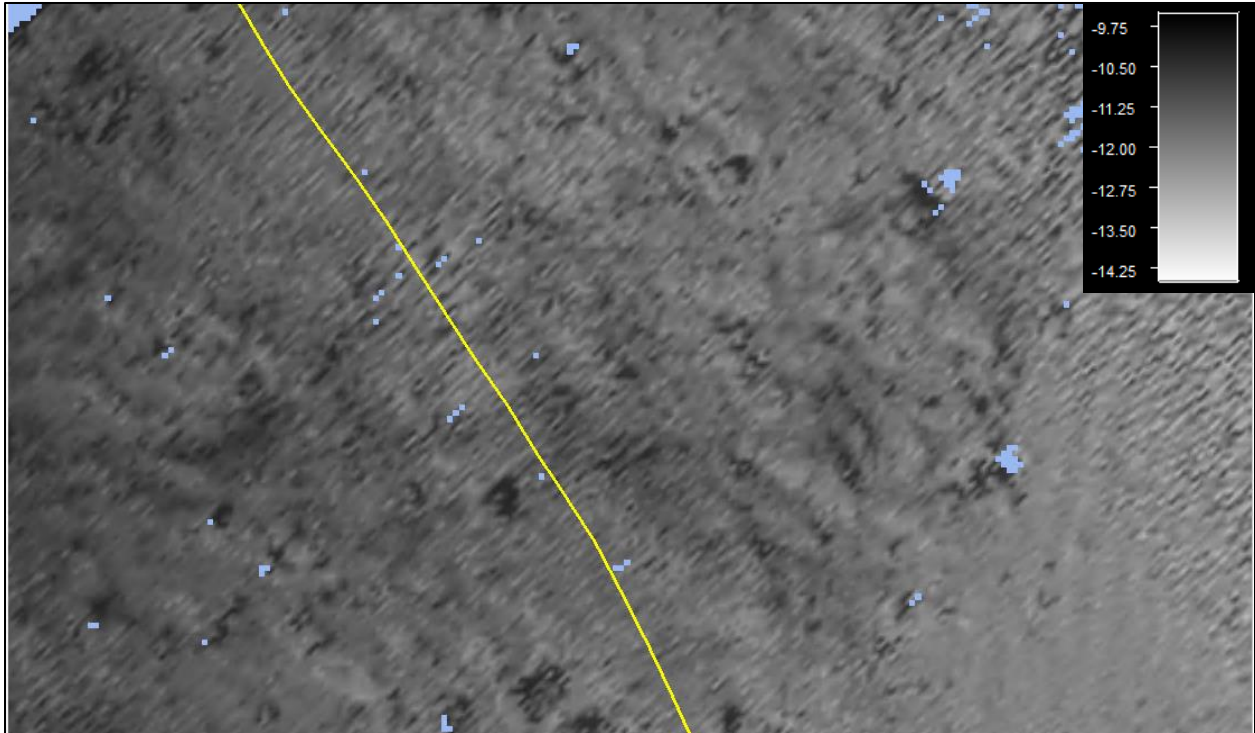


*Figure 115 – Smearing and noise at normal incidence.*

From a quantitative point of view, the nadir oscillation in rare cases reached the minimum of six soundings per 0.5-meter node in this line nadir, equivalent to 24 soundings per meter squared. Given that the number of soundings per meter along-track was 6.7 at 3.5 knots (see Figure 113), the across-track density at normal incidence, in the worst case, was 3.6 soundings/meter, which is still within the NOAA specs for target detection.

The impact of not being yaw-stabilized:

At a 3.5 knots speed and 14 Hz ping rate, a 1-meter target would be ensonified at least seven times (assuming a constant heading), which would be considered a valid target detection capability, according to the NOAA (2022) 3-hit criterion. It is known, though, that the 6205 is not stabilized for yaw, so changes in heading may hinder the target detection capability at the outer swath. For example, the survey lines for this study were navigated by a trained crew; however, the

helmsman oscillation in heading reached a maximum of 52° within 19 seconds, representing a rate of turn (ROT) of 2.7°/s.

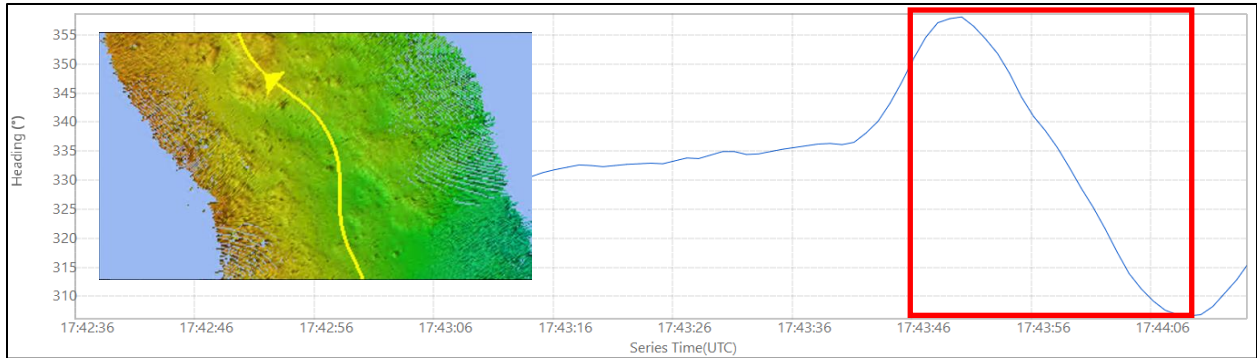


*Figure 116 - Maximum heading change rate observed at this study's survey.*

Typically, the number of pings that would hit a target of length  $L$  is estimated by:

$$N = \frac{Lp}{v} \quad (4.1)$$

Where:

- $L$  is the one-dimensional size of the required feature (for special order,  $L=1$  meter).
- $N$  is the desired number of pings to hit the target (for the NOAA criterion,  $N=3$ ).
- $v$  is the boat speed.
- $p$  is the ping rate.

However, when a ship turns, the heading change is usually faster than the course on ground change, so in an infinitesimal time, it happens as if the ship kept its original course but slightly changed its heading.



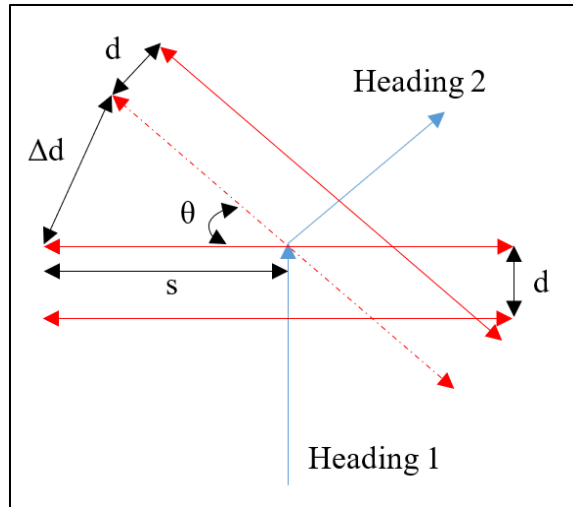


Figure 117 - Ping distribution along a heading change.

Considering the misalignment between the drift speed and the tangential speed low, the number of pings hitting the target is now reduced, approximated by Equation 4.2 below:

$$N = \frac{Lp}{v_{drift} + s \times ROT} \quad (4.2)$$

Where:

- $s$  is half the swath length (port or starboard side).
- $ROT$  is the rate of turn in radians per time unit.

Taking that into consideration, while the ship was performing that turn, the number of pings a 1-meter target would receive at 3.5 knots at a 50-meter maximum range would be reduced from 7 to 3 times only, at the limit of not following the NOAA specifications at the far range. Regarding that matter, when using a non-stabilized system such as the 6205, it is essential to consider how the ship usually oscillates around the line azimuth to plan the survey speed, preferably not using data from turns.

#### 4.2.4. Efficiency

A metric that may be used to compare the 6205 and the EM2040P efficiency is the amount of time they take to produce equivalent results; in other words, a DTM with similar quality, 100% bathymetric coverage survey, and ability to detect required targets all over the swath. Thus, the criteria used for this comparison were:

I. Quality - achieving uncertainties compatible with the desired S-44 survey order. This simulation considered the swath coverages achieved in section 4.2.1.

II. Target detection – target independent ensonification at least three times along track per pass (NOAA, 2022) within the swath range to be used, according to Equation 4.2. This criterion will evaluate along-track density only, as both systems are already known to more than satisfy 3 hits across-track for a 1-meter-wide target.

III. Bathymetric coverage - complete seafloor coverage, meaning that the survey speed does not allow along-track gaps from one ping to the next. This is achieved by surveying at speeds up to the limit given by Equation 4.3, as function of the along-track beamwidth  $\underline{\alpha}$  and the maximum ping rate  $\underline{p}$ . This ping rate is given by Equation 4.4, depending on the angular coverage  $\underline{\beta}$  (one side) and the number of simultaneous swaths in the water  $\underline{s}$ .

$$v_{coverage} = 2dp \tan\left(\frac{\alpha}{2}\right) = cs \tan\left(\frac{\alpha}{2}\right) \cos(\beta) \quad (4.3)$$

$$p = \frac{cs \cos(\beta)}{2d} \quad (4.4)$$

This simulation considered a 10-meter depth to represent a typical shallow water environment. The efficiency of each system was calculated depending on the time needed to survey an area of 1 NM<sup>2</sup>, calculated with Equation 4.5, where  $\underline{o}$  is the desired overlap percentage.

$$\Delta t = \frac{1}{(2 - o)v d \tan(\beta)} \quad (4.5)$$

The limiting speed considered was the minimum to satisfy both the second and the third criteria, respecting the hardware limitations documented. The more relevant limitation accounted for was the 6205 maximum speed of 5 knots, according to EdgeTech (2019). The simulation results are summarized in Table 14.

*Table 14 - Efficiency comparison: EM2040P vs. 6205.*

<b>System / Criterion</b>	<b>EM2040P Dual Swath</b>	<b>6205 (Special Order)</b>	<b>6205 (Order 1)</b>
Maximum coverage	Up to 70°	Up to 73°	Up to 80°
Maximum survey speed	22.6 kt	5.0 kt	4.4 kt
Time to survey 1 NM <sup>2</sup> at max. speed	3h	11.3h	7.4h
Efficiency (max. speed)	1.00	0.26	0.40
Time to survey 1 NM <sup>2</sup> at 4 kt	16.8h	14.1h	8.2h
Efficiency (same speed)	1.00	1.19	2.05

The time needed to perform the survey with the maximum speed possible is 11.3h for the 6205, while it is only 3.0h for the EM2040P, because the latter was designed with dual swath, doubling the usable speeds. Thus, in this case, the high speed the EM2040P can achieve is counterbalancing the 6205 wider swath, greatly surpassing the 6205 efficiency. Thus, there is a clear advantage in using the MBESs when high speeds are allowed. It is important to mention that high speeds usually lead to more propeller noise, reducing the SNR, so a coverage of 70° may not be realistic.

Notwithstanding, this study's primary concern is the shallow water environment, where safety or resources may limit the maximum speed, the survey can be performed at. In that situation, the 6205's efficiency is higher than the EM2040P's, especially if the survey quality is expected at the S-44 Order 1 level, having practically double the MBES efficiency.

## CHAPTER 5: CONCLUSION

### 5.1. Discussion

This research explored the potential of receive cycle beamforming to improve multi-stave PMBS bottom detection. Focusing on that, the three research objectives were accomplished:

- A differential phase bottom detection algorithm was devised by evaluating complex phasors of two (or more) virtual staves created by combining a set number of array elements through conventional phase-shift beamforming. Other techniques common to PMBS processing were also developed and implemented, such as array shading, windowing, binning, filtering, and error modeling.

- The beamforming algorithm could successfully estimate DOAs, fairly consistent with the manufacturer's solution. Besides, two other DOA estimators were developed based on conventional techniques: a more straightforward half-wavelength average estimator and a refinement using Vernier concepts. The resultant depths, their SNR and phase coherence were compared. Complimentary integration and gridding scripts made possible the use of more sophisticated analysis tools from those commercially available (in this study, Qimera and Fledermaus, from QPS).

- Datasets using the PMBS EdgeTech 6205 and the MBES EM2040P were acquired with a minimal inter survey delay (one day), thus minimizing the possibility of environmentally influenced changes between the two datasets. The survey area near Odiorne Point was a challenging, but realistic environment for system evaluation. Although small, it included a significant slope in shallow water (from 2 to 14 meters), a very rocky region with scattered targets of many sizes, and a smooth area near the southwest corner of the survey area. The data analyses

were made using background theory, theoretical modeling in Python, and the commercial applications Qimera and Fledermaus. This study assessed the IHO S-44 Survey Order achieved in the depth cross-check, target detection capability, and density. An efficiency evaluation was also developed at the end of the analysis.

Based on the results reported in Chapter 4, the research questions were answered:

a) How can applying beamforming in a multi-stave PMBS improve the signal processing results?

The use of beamforming and steering in steps increased the amplitude gain where the signals were expected to arrive while attenuating simultaneous echoes from extraneous directions (multipath, nadir interference). This hypothesis could be demonstrated during the comparison between the conventional and the beamforming quality factors:

I. While half-wavelength average solutions were indistinguishable from noise from  $65^\circ$  incidence angle and beyond, Vernier and Beamforming estimators could follow morphology up to about  $83^\circ$  incidence angle. Although beamforming achieved comparable results to Vernier in detecting morphology, the first was seven times more computationally efficient than the latter.

II. Beamformed signals enjoyed an SNR increase in the far range and close to normal incidence, where decorrelation is known to happen, improving the accuracy of DOA estimation. This effect also helped during the filtering process: SNR levels from shadowed areas were better segregated from good data, avoiding unwanted rejection of nadir data or mid/far-range good data while attempting to reject shadows.

III. A huge gain in coherence was observed in swath edges, as a consequence of the multipath attenuation and the directivity gain, resulting in solutions less corrupted by noise. The beamforming spatial filter ability was more efficient in reaching reasonable depth solutions than

diluting noise through numerous series of heavy averages in Vernier. That could be seen in 2D profiles, where less noise was seen in beamforming swaths, especially from mid to far range.

IV. Less noise was observed in the beamforming DTMs at normal incidence compared to the Vernier algorithm, reinforcing the idea that the first method is beneficial to mitigate the common slant range interference at that region.

V. The EdgeTech solutions, compared to the in-house developed algorithms, provided smoother target detection in the system nadir while not being affected by beam steering errors at the swath edges. This leads to the belief that the manufacturer used longer across-track averaging windows, and their ensembles had less embedded noise. However, the point cloud and DTM analyses showed that the manufacturer's method may be causing some degree of bias and target height underestimation.

VI. Window intensities derived through beam forming could be used as a potential means of improving the associated side scan image, given the beamforming multipath suppression effect and the noise dilution during the window average.

b) What is the manufacturer solution performance compared with a well-assessed echo sounder?

I. The 6205 raw lines collected in this study, when cross-checked with a Special Order EM2040P reference grid, were able to achieve Special Order up to a  $73^\circ$  coverage, in a conservative estimate where rough and sloped areas were not ignored when estimating the TVU. A coverage of  $80^\circ$  was considered usable if there is tolerance to a TVU at Order 1 level.

II. Regarding target detection, using a wider swath reduces the maximum ping rate the system can achieve. Nevertheless, at speeds of 5 knots or less, the system had a fast enough ping rate to maintain the minimum of three hits per target, as specified by the NOAA (2022) standards,

even during the more sinuous heading deviation ( $52^\circ$  within 19 seconds), where the lack of yaw stabilization made the outer edge of the swath less dense. In river corridors, where heavy turns are fated to happen, it is important to establish a maximum ROT and speed that would maintain the target detection capability. In the event that this is not possible, migrating to a yaw-stabilized system (such as the EM2040P) may be necessary. Regarding the dataset's ability to depict targets, DTMs with single 6205 lines could successfully represent 1-meter targets up to  $76^\circ$ . However, on many occasions, it underestimated small target heights by a few decimeters. From the safety-of-navigation point of view, one may consider the correct reproduction of the target minimum depth as the main factor to consider a detection as valid. Considering that, the result obtained is detrimental to building trust in the 6205 DTM as a Special Order product, making it more appropriate for Order 1 in this criterion.

III. The nadir gap, a problem that hindered the efficiency promise of PMBSs, seems to be consistently resolved in shallow waters. Rare-to-no nadir gaps were found in the survey lines run in this study, and the required mean sounding density was maintained throughout the swath. Density oscillations were systematically seen in the nadir, though, but not enough to hinder target detection, as far as this study could assess. However, the normal incidence region (from  $0^\circ$  to  $15^\circ$  incidence) is systematically more smeared and noisier than mid-range.

IV. Regarding efficiency, if an Order 1a product is expected, the 6205 could be used up to  $80^\circ$  coverage, representing a swath 105% wider than a  $70^\circ$  MBES. If the Special Order is required, the usable swath may be reduced to  $73^\circ$ , which would represent a gain of only 19%. If time is the factor that will define which system is to be used, the choice needs to consider the maximum speed the survey can be performed, which may be limited by the systems' specifications (5.0 knots in the case of the 6205), the required quality, or the environment (as in shallow waters or uncharted



regions). In situations that allow the use of high speeds, MBES systems tend to be more efficient, especially if they have multiple along-track swaths. In contrast, when both systems are restricted to speeds lower than 5 knots, the 6205 will have the upper hand in efficiency by the ratio that its swath is wider.

All aspects considered, beamforming in multi-stave PMBS is seen to significantly aid detection at both normal incidence and far range, and the EdgeTech 6205, specifically, satisfied the S-44 guidelines for hydrographic surveys. When compared to the MBES Kongsberg EM2040P, the quality demonstrated by the 6205 seemed to be more consistent with S-44 Order 1a surveys because of the underestimation of small target heights, which is a main concern in S-44 Special Order areas where “underkeel clearance is critical” (IHO, 2022). That said, considering that single-beam echo sounders are still widespread in Brazilian riverine surveys, S-44 Order 1 should be acceptable in most cases. In conclusion, the EdgeTech 6205 may be a reasonable alternative to Order 1 riverine surveys, capable of providing up to two times the swath an MBES with a 70° coverage would achieve in a 10-meter depth.

## **5.2. Suggestions for future works**

Due to this study’s time constraints, it was not possible to explore all possibilities to improve the PMBS detection with beamforming, so some aspects may be worth studying in the future.

First, exploring the phase time series regression and more variants of subarray processing methods, including phase unwrapping of ambiguous virtual stave pairs, may be a way to reduce the bottom detection uncertainty.

Second, the use of more advanced array processing techniques in multi-stave PMBSs may achieve better feature detection at normal incidence than conventional beamforming, while keeping enough efficiency to be used in real-time. Combinations of techniques may be used since the crucial issues found in this study were restricted to the nadir region.

And, finally, exploring the benefits of beamforming as a means of improving the side scan imagery, which may include interference and layover mitigation.

## LIST OF REFERENCES

- Abraham, D. A. (2019). *Underwater Acoustic Signal Processing. Modeling, Detection, and Estimation*. Ellicott City: Springer.
- Alexopoulos, A. (2005). *Phased Array Analysis Using a Modified Chebyshev Approach*. Edinburgh: Defence Science and Technology Organisation. Retrieved from <https://apps.dtic.mil/sti/pdfs/ADA446241.pdf>
- Applanix Corporation. (2017). *POS MV V5 Installation and Operation Guide*. Retrieved from [https://buyandsell.gc.ca/cds/public/2018/04/11/45eb05446e5501e70f07d1a4ac0088e4/A.BES.PROD.PW\\_OLZ.B002.E7035.ATTA015.PDF](https://buyandsell.gc.ca/cds/public/2018/04/11/45eb05446e5501e70f07d1a4ac0088e4/A.BES.PROD.PW_OLZ.B002.E7035.ATTA015.PDF)
- Brisson, L. N., Wolfe, D. A., & Staley, M. (2014). Interferometric Swath Bathymetry for Large Scale Shallow Water Hydrographic Surveys. *Canadian Hydrographic Conference*. St. John's: Canadian Hydrographic Association. Retrieved from <https://www.edgetech.com/wp-content/uploads/2019/07/EdgeTech-Paper-on-6205-presented-at-CHC2014.pdf>
- Burdic, W. S. (1984). *Underwater Acoustic System Analysis*. Los Altos Hills: Peninsula.
- Butowski, M. (2014). Improving the Capabilities of Swath Bathymetry Sidescan Using Transmit Beamforming and Pulse Coding [Master's Thesis, University of Victoria]. Victoria, British Columbia, Canada. Retrieved from [http://dspace.library.uvic.ca/bitstream/handle/1828/5343/Butowski\\_Marek\\_MASc\\_2014.pdf?sequence=1&isAllowed=y](http://dspace.library.uvic.ca/bitstream/handle/1828/5343/Butowski_Marek_MASc_2014.pdf?sequence=1&isAllowed=y)
- Chesterman, W. D., Quinton, J. P., Chan, Y., & Matthews, H. R. (1966). Acoustic Surveys of the Sea Floor near Hong Kong. *International Hydrographic Review*. Retrieved from [https://www.google.com/url?sa=t&rct=j&q=&esrc=s&source=web&cd=&ved=2ahUKEwiz89eayPH\\_AhV4K1kFHS\\_LA2AQFnoECBQQAQ&url=https%3A%2F%2Fjournals.lib.unb.ca%2Findex.php%2Fihv%2Farticle%2Fdownload%2F24022%2F27807%2F&usq=AOvVaw2Z-ddInEDp8u-c87MtXjOZ&opi=89978449](https://www.google.com/url?sa=t&rct=j&q=&esrc=s&source=web&cd=&ved=2ahUKEwiz89eayPH_AhV4K1kFHS_LA2AQFnoECBQQAQ&url=https%3A%2F%2Fjournals.lib.unb.ca%2Findex.php%2Fihv%2Farticle%2Fdownload%2F24022%2F27807%2F&usq=AOvVaw2Z-ddInEDp8u-c87MtXjOZ&opi=89978449)
- Chonghua, Y. (2019). *Hillshade from a Digital Elevation Model*. Retrieved from Github: [https://github.com/royalosityin/Work-with-DEM-data-using-Python-from-Simple-to-Complicated/blob/master/ex07-Hillshade%20from%20a%20Digital%20Elevation%20Model%20\(DEM\).ipynb](https://github.com/royalosityin/Work-with-DEM-data-using-Python-from-Simple-to-Complicated/blob/master/ex07-Hillshade%20from%20a%20Digital%20Elevation%20Model%20(DEM).ipynb)

- Cloet, R. L., & Edwards, C. R. (1986, September). The Bathyscan Precision Swathe Sounder. *Oceans* (pp. 153-162). Washington D.C.: IEEE. doi:10.1109/OCEANS.1986.1160560
- Cloet, R. L., Hurst, S. L., Edwards, C. R., Phillips, A. J., & Duncan, A. J. (1982, September). A Sideways-looking Towed Depth-measuring System. *The Journal of Navigation*, 35(3), 411-420. doi:10.1017/S0373463300021780
- de Moustier, C. (1988). State of the Art in Swath Bathymetry Survey Systems. *International Hydrographic Review*, 25-54. Retrieved from <https://scholars.unh.edu/ccom/901/>
- Denbigh, P. N. (1989). Swath Bathymetry: Principles of Operation and an Analysis of Errors. *Journal of Oceanic Engineering*, 289-298. doi:10.1109/48.35979
- DHN. (2017). *Normas da Autoridade Marítima para Levantamentos Hidrográficos*. Retrieved from <https://www.marinha.mil.br/dhn/sites/www.marinha.mil.br.dhn/files/normam/NORMAN-25-REV2-MOD1.pdf>
- Dijkstra, S. (2021). UNH Seabed Mapping Course Laboratories C and D algorithms.
- DNIT. (n.d.). *Infraestrutura Aquaviária*. Retrieved 12 20, 2022, from gov.br: <https://www.gov.br/dnit/pt-br/assuntos/aquaviario>
- Doucet Survey Inc. (2016). *Surveying and Laser Scanning Services for the "Gulf Surveyor" Research Vessel*.
- Edgetech. (2015). *Edgetech Multi Phase Echo Sounder Technology*. Retrieved from Edgetech.com: <https://www.edgetech.com/wp-content/uploads/2019/07/Multi-Phase-Echo-Sounder.pdf>
- Edgetech. (2019, April). 6205 Bathymetry & Side Scan System User Hardware Manual. West Wareham, Massachusetts, United States of America. Retrieved from [https://www.edgetech.com/wp-content/uploads/2019/07/0014877\\_REV\\_F.pdf](https://www.edgetech.com/wp-content/uploads/2019/07/0014877_REV_F.pdf)
- EdgeTech. (2020). Technical Note. Feature Detection with an EdgeTech Side Scan Sonar. Retrieved from <https://www.edgetech.com/wp-content/uploads/2020/10/Feature-detection-Rev3.pdf>

- Edgetech. (2022, June 17). *JSF File and message descriptions*. Retrieved from Edgetech.com: [https://www.edgetech.com/wp-content/uploads/2019/07/0023492\\_Rev\\_G.pdf](https://www.edgetech.com/wp-content/uploads/2019/07/0023492_Rev_G.pdf)
- EdgeTech. (2022a). *Discover Bathymetric User Software Manual*. West Wareham. Retrieved from [https://www.edgetech.com/wp-content/uploads/2019/07/0014878\\_Rev\\_H.pdf](https://www.edgetech.com/wp-content/uploads/2019/07/0014878_Rev_H.pdf)
- Friedman, A., Pizarro, O., Williams, S. B., & Johnson-Roberson, M. (2012, December). Multi-Scale Measures of Rugosity, Slope and Aspect from Benthic Stereo Image Reconstructions. *Plos One*, 7(12), pp. 1-14. Retrieved from <https://journals.plos.org/plosone/article/file?id=10.1371/journal.pone.0050440&type=printable>
- Grall, P., Kochanska, I., & Marszal, J. (2020). Direction-of-Arrival Estimation Methods in Interferometric Echo Sounding. *Sensors*. doi:<https://doi.org/10.3390/s20123556>
- Harris, F. J. (1978, January). On the Use of Windows for Harmonic Analysis with the Discrete Fourier Transform. *Proceedings of the IEEE*, 66. Retrieved from <http://web.mit.edu/xiphmont/Public/windows.pdf>
- Hughes Clarke, J. E. (2021). UNH Seabed Mapping Course Class Notes.
- IHO. (2022, October). Standards for Hydrographic Surveys. (6.1.0). Monaco. Retrieved from [https://iho.int/uploads/user/pubs/standards/s-44/S-44\\_Edition\\_6.1.0.pdf](https://iho.int/uploads/user/pubs/standards/s-44/S-44_Edition_6.1.0.pdf)
- Jenness, J. (2003). *Grid Surface Areas: Surface Area and Ratios from Elevation Grids [Electronic manual]*. Retrieved from Jenness Enterprises: ArcView® Extensions: [http://www.jennessent.com/arcview/arcview\\_extensions.htm](http://www.jennessent.com/arcview/arcview_extensions.htm)
- Jin, G., & Tang, D. (1996). Uncertainties of Differential Phase Estimation Associated with Interferometric Sonars. *IEEE*, 53-63. doi:10.1109/48.485201
- Kinsler, L. E., Frey, A. R., Coppens, A. B., & Sanders, J. V. (2000). *Fundamentals of Acoustics* (4th ed.). Wiley.
- Kongsberg Maritime AS. (2020). *EM 2040P Multibeam echo sounder Installation manual*. Retrieved from [https://www.kongsberg.com/contentassets/24be01e20bf94e02a1f29d5928755a87/417418ac\\_em2040p\\_installation\\_manual\\_en.pdf](https://www.kongsberg.com/contentassets/24be01e20bf94e02a1f29d5928755a87/417418ac_em2040p_installation_manual_en.pdf)

- Kraeutner, P. H. (1998). *Small Aperture Acoustic Imaging Using Model Based Array Signal Processing [Doctoral thesis, Simon Fraser University]*. Burnaby, BC, Canada.
- Kraeutner, P. H., & Bird, J. S. (1997). Principal components array processing for swath acoustic mapping. *Oceans*. Halifax: IEEE. doi:10.1109/OCEANS.1997.624174
- Kraeutner, P. H., Bird, J. S., Charbonneau, B., Bishop, D., & Hegg, F. (2002). Multi-Angle Swath Bathymetry Sidescan Quantitative Performance Analysis. *Oceans* (pp. 2253-2263). Biloxi: IEEE. doi:10.1109/OCEANS.2002.1191981
- Llort-Pujol, G., Sintes, C., & Gueriot, D. (2008). Analysis of Vernier interferometers for sonar bathymetry. *OCEANS*. Quebec: IEEE. doi:10.1109/OCEANS.2008.5151958
- Llort-Pujol, G., Sintes, C., Chonavel, T., Morrisson III, A. T., & Daniel, S. (2012, March/April). Advanced Interferometric Techniques for High-Resolution Bathymetry. *Marine Technology Society, 46*(2), 10-31. doi:10.4031/MTSJ.46.2.4
- Lurton, X. (2000). Swath Bathymetry Using Phase Difference: Theoretical Analysis of Acoustical Measurement Precision. *IEEE*, 351-363.
- Lurton, X. (2008). *An Introduction to Underwater Acoustics*. Berlin: Springer.
- NOAA. (2022, March). Hydrographic Survey Specifications and Deliverables. Retrieved from [https://nauticalcharts.noaa.gov/publications/docs/standards-and-requirements/specs/HSSD\\_2022.pdf](https://nauticalcharts.noaa.gov/publications/docs/standards-and-requirements/specs/HSSD_2022.pdf)
- Pimentel, V. B. (2018). Comparação entre dados batimétricos adquiridos com ecobatímetro multifeixe e dados batimétricos adquiridos com sonar de varredura lateral interferométrico. [Master's thesis, Universidade Federal Fluminense]. Niterói, Rio de Janeiro, Brazil. Retrieved from <https://app.uff.br/riuff/bitstream/handle/1/23894/306%20-%20DISSERT%20-%20Vitor%20Bravo%20Pimentel%202018.pdf?sequence=1&isAllowed=y>
- Potucek, M. (2013). Acoustic geohabitat mapping: A case study [Master's Thesis, Stockholm University]. Stockholm. Retrieved from [https://www.su.se/polopoly\\_fs/1.553908.1620203899!/menu/standard/file/2013\\_martina-potucek\\_msc-marine-geology\\_60hp.pdf](https://www.su.se/polopoly_fs/1.553908.1620203899!/menu/standard/file/2013_martina-potucek_msc-marine-geology_60hp.pdf)

- QPS. (2022, March). Fledermaus 7.8 Documentation FMGT 7.10/FMMidwater 7.9. Retrieved from [https://publicdownload.qps.nl/Fledermaus/Fledermaus-7.8-Documentation\\_v3.pdf](https://publicdownload.qps.nl/Fledermaus/Fledermaus-7.8-Documentation_v3.pdf)
- QPS. (2023). *Qimera Cross Check*. Retrieved from QPS: [https://qpssoftware.scrollhelp.site/qimera/2.5/qimera-cross-check#id-\(2.5\)QimeraCrossCheck-WhatitDoes](https://qpssoftware.scrollhelp.site/qimera/2.5/qimera-cross-check#id-(2.5)QimeraCrossCheck-WhatitDoes)
- Rinehart, R. W., Wright, D. J., Lundblad, E. R., Larkin, E. M., Murphy, J., & Cary-Kothera, L. (2004). ArcGIS 8.x Benthic Terrain Modeler: Analysis in American Samoa. *Proceedings of the 24th Annual ESRI User Conference*. San Diego. Retrieved from <https://proceedings.esri.com/library/userconf/proc04/docs/pap1433.pdf>
- Sintes, C. (2002, March 13-16). Interferometric Side Scan Sonar: A Tool for High Resolution Sea Floor Exploration. In Cedre (Ed.), *Technical lessons learnt from the Erika incident and other oil spills*. Brest.
- Stegen, R. J. (1953, November). Excitation Coefficients and Beamwidths of Tschebyscheff Arrays. *Proceedings of the IRE*, 41, pp. 1671-1674. doi:10.1109/JRPROC.1953.274197
- Tucker, D. G. (1960). Directional Echo Sounding. *International Hydrographic Review*, 37, pp. 43-53. Retrieved from [https://www.google.com/url?sa=t&rct=j&q=&esrc=s&source=web&cd=&ved=2ahUKEwjBzPnex\\_H\\_AhUeF1kFHZN5B2cQFnoECA4QAQ&url=https%3A%2F%2Fjournals.lib.unb.ca%2Findex.php%2Fihr%2Farticle%2Fdownload%2F26540%2F1882519300%2F1882519535&usq=AOvVaw0q910w2Sd9AUcobkEB1IDl&](https://www.google.com/url?sa=t&rct=j&q=&esrc=s&source=web&cd=&ved=2ahUKEwjBzPnex_H_AhUeF1kFHZN5B2cQFnoECA4QAQ&url=https%3A%2F%2Fjournals.lib.unb.ca%2Findex.php%2Fihr%2Farticle%2Fdownload%2F26540%2F1882519300%2F1882519535&usq=AOvVaw0q910w2Sd9AUcobkEB1IDl&)
- Van Trees, H. L. (2002). *Optimum Array Processing: Part IV of Detection, Estimation and Modulation Theory*. John Wiley & Sons. doi:10.1002/0471221104
- Vincent, P. (2013). Modulated signal impact on multibeam echosounder bathymetry. [Doctoral Thesis, Université de Rennes].
- Wang, M. (2018). *Doa-tools*. Retrieved from Github: <https://github.com/morriswmz/doatools.py>